Bettina Schweda, BSc
01430228

Phenylene-Linked Perylene-Monoimide based Acceptors for the Application in Organic Solar Cells

MASTER THESIS
In partial fulfillment of the requirements for the academic degree
Diplom-Ingenieur
in the field of study of Technical Chemistry

submitted at
Graz University of Technology

Under the supervision of
Univ.-Prof. Dipl.-Ing. Dr.techn. Gregor Trimmel
Institute for Chemistry and Technology of Materials

Graz, November 2019

Affidavit / Eidesstattliche Erklärung

I declare that I have authored this thesis independently, that I have not used other than the declared sources/resources, and that I have explicitly indicated all material which has been quoted either literally or by content from the sources used. The text document uploaded to TUGRAZonline is identical to the present master's thesis.

Ich erkläre an Eides statt, dass ich die vorliegende Arbeit selbstständig verfasst, andere als die angegebenen Quellen/Hilfsmittel nicht benutzt, und die in den benutzten Quellen wörtlich und inhaltlich entnommenen Stellen als solche kenntlich gemacht habe. Das in TUGRAZonline hochgeladene Textdokument ist mit der vorliegenden Masterarbeit identisch.

_____	_____
Date/Datum	Signature/Unterschrift

I have not failed; I have only discovered 10 000 ways that did not work.

-- Thomas A. Edison

Abstract

The rising human population leads to increasing energy demand. Renewable resources take an important part in the generation of electrical energy. Thereby, photovoltaic systems are a key to replace conventional energy sources.

Commercially available systems are mostly based on crystalline silicon as the active layer. However, these materials are expensive due to demanding manufacturing processes and high energy input. Thus, ongoing research is done on cheaper, easily producible, environmentally friendly materials. Those, and other kinds of materials, can be used in the emerging class of organic solar cells. Perylenes are promising structural motifs for organic solar cell materials. In this work, properties of variously linked perylene-monoimide-phenylene-perylene-monoimide systems have been studied. The synthesis of these molecules were accomplished via Suzuki-coupling of the 8-bromo-perylene-monoimide and different phenylene diboronic and triboronic acids or their pinacol esters. The synthesis yielded between 8 – 30%. The compounds were characterized using NMR spectroscopy, mass spectrometry, absorption- and fluorescence spectroscopy, as well as thermal analysis; thermogravimetric analysis and differential scanning calorimetry. The experimental results of the optical studies were compared with density functional theory (DFT) simulations. During the assembly of the organic solar cells, challenges were faced concerning the solubility of the synthesized compounds. Nevertheless, promising results were obtained using blends of a suitable polymer and the phenylene-linked perylene monoimides. A power conversion efficiency of almost 2% was achieved without optimization of the solar cell parameters.

Herein, we present novel acceptor materials based on perylene monoimide derivatives. This research gives insight into the main characteristics of those compounds including the challenges and potential.

Kurzfassung

Die ständig wachsende Bevölkerung führt zu einem höheren Energiebedarf, weshalb man bei der Energiegewinnung vermehrt auf erneuerbare Energien ausweicht. Ein Beispiel hierfür sind verschiedene Photovoltaiksysteme.
Handelsübliche Solarmodule basieren meist auf kristallinem Silizium, das als Aktivschicht verwendet wird. Diese Zellen haben den Nachteil, dass ihre Herstellung mit hohen Kosten, sowie einem hohen Energieaufwand verbunden ist. Daher wird nach günstigeren, leichter produzierbaren und ökologisch verträglichen Materialien gesucht. Eine Alternative könnte die aufkommende Klasse der organischen Solarzellen sein. Eine vielversprechende Materialklasse dieser Art von Solarzellen stellen Perylene und Perylenderivate dar. In dieser Arbeit werden die Eigenschaften von Molekülen, in denen zwei oder drei Peryleneinheiten über eine Phenyleneinheit verbunden sind, untersucht. Hierfür wurde das 8-Bromperylenmonoimid mit den entsprechenden Phenyldi- bzw. triboronsäurederivaten mittels einer Suzuki-Kupplung umgesetzt, wobei die Ausbeuten zwischen 8 und 30% betrugen. Anschließend wurden die Verbindungen mittels NMR-Spektroskopie, Massenspektrometrie, Absorptions- und Fluoreszenzspektroskopie, sowie mit der Thermogravimetrischen Analyse und Dynamischen Differenzkalorimetrie untersucht. Die experimentellen optischen Daten wurden mit Dichtefunktionaltheoriesimulationen (DFT) verglichen. Bei der Assemblierung der organischen Solarzellen stellte sich heraus, dass die Löslichkeit der verschiedenen Verbindungen eine große Herausforderung ist. Dennoch konnten in Mischungen mit einem geeigneten Polymer Solarzellen mit guten Wirkungsgraden von bis zu 2% erreicht werden, ohne die Solarzellenparameter zu optimieren.
In dieser Arbeit werden neue Materialien aufgezeigt, die auf einer Perylenmonoimid-Phenylene-Perylenmonoimid Struktur basieren. Diese Arbeit gibt einen Einblick in die Eigenschaften dieser Verbindungen, wobei neben Herausforderungen auch deren Potenziale demonstriert werden.

Acknowledgements

At this point, I would like to thank all those who have contributed to the success of this work through their professional and personal support. I am particularly grateful for the expert advice and encouragement of Prof. Gregor Trimmel throughout the whole thesis, and the opportunity to work on that very interesting and diverse topic. In addition, I would like to acknowledge the contribution of Petra Kaschnitz, Josefine Hobisch, Karin Bartl and David Pfeifer, for the numerous measurements they have done for me.

Furthermore, my thanks go to my whole working group for the friendliest and most motivational working environment. All the talks during coffee or lunch breaks and also the gaming evenings were valuable and above all a lot of fun. Hereby I would like to mention Matiss Reinfelds and Stefan Weber, who had always an open ear for all kind of problems and provided useful tips for each of them.

Moreover, I would like to thank my parents for their support through my whole study and beyond, as well as my sister and brother-in-law, who were always there when needed. I thank all my friends and colleagues who studied with me, making exams less terrible. Especially I want to mention Sarah Rendl and Lukas Heupl, who provided lots of help during my master study. At last, I want to thank Werner Schlemmer for never ending support, patience and inspiration.

Table of Contents

1. Introduction

In the last decade the demand for renewable energy sources increased drastically due to environmental reasons including climate change. Beside wind or water energy, solar power is used and developed worldwide to gain as much energy as possible from the sunlight. By 2017, still 68.4% of the electricity was generated from fossil resources and nuclear fission reactors globally, followed by hybrid power (19.5%), wind power (6.5%), photovoltaics (2.5%) and others (3.0%). Nevertheless, the number of installed photovoltaic (PV) systems is increasing worldwide[1]. In Austria, there is an increasing number of installed PV systems, giving already about 1 400 000 kW installed PV power in 2018[2].

Most of the installed systems are based on crystalline silicon technologies. It can be distinguished between monocrystalline and polycrystalline silicon solar cells, and thin film technologies based on amorphous silicon, CdTe and copper indium gallium selenide (CIGS). Single crystal silicon heterostructures have a certified efficiency of 26.7%[3], whereas the polycrystalline cells reach only 22.3% so far[4]. The guaranteed lifespan is exceeding 30 years[5]. Beside silicon based systems, new technologies were developed based on GaAs, reaching an efficiency of 30.5% in concentrated systems[6]. In addition, the thin film technologies based on CdTe and CIGS can reach efficiencies up to 22.1% and 23.4%, respectively[7,8]. Although these PV systems are widely used, they have high production costs[9].

In 1991 the dye-sensitized solar cells (Grätzelzellen) were developed[10]. In contrast to the silicon based photovoltaics, the light is absorbed by a sensitizer which is attached to the surface of a semiconductor. Upon irradiation, the charge separation takes place at the interface between the sensitizer and the conduction band of the solid[11]. However, those colorful cells can so far only reach efficiencies up to 11.9%, which is less than other commercially available systems.

Nevertheless, the most commonly used solar cells on the market have one disadvantage: The silicon wafers which are an essential part of the set-up, are expensive and a lot of energy is needed for the production process of these cells. However, the advantage is that silicon is one of the most frequent elements in the earth's crust[12]. The dye-sensitized solar cells are potentially cheaper but they can reach only half of the efficiency of silicon-based cells. CdTe based solar cells currently approach the efficiency of silicon based solar cells. In addition, the modules give a better Life Cycle Assessment compared to silicon solar cells[13] and achieve better conversion efficiencies under diffused light[14]. However, Cd and Te are toxic materials and the

availability is limited. CIGS modules contain toxic and limited elements as well, but only small amounts are used for the production due to the thin film technology[15]. Moreover, the consumption of semiconductor material is less and the variability concerning the support material is higher compared to silicon modules[14].

In 2013 the investigation of a novel type of material started which have a perovskite crystal structure. The general formula of the structure is ABX_3, with different metals A and B in the center and on the edges of the unit cell and oxygen X on the face-centered holes. The early, very efficient cells contain lead as central atom in the structure. Starting at an efficiency of about 13%[16], these cells improved rapidly, now reaching up to 25.2%[17], after only 6 years of refinement. Soon, people started to assemble tandem cells with silicon and a lead perovskite, which increased the efficiency to 28%[17], exceeding even the other silicon-based photovoltaics on the market. However, the biggest problems are the stability of the active layer, as it is air and moisture sensitive[18]; as well as them containing lead, which is toxic for any living organism[19]. Many researchers are now looking for an alternative to the lead, resulting in the investigation of perovskites containing tin or germanium[20–22].

Even before the perovskite cells were developed, another novel class of photovoltaic cells has been developed; the organic solar cells. Because of the high exciton binding energies in organic materials, organic solar cells usually combine two organic semiconductors – a donor material (electron donating, high hole mobility) and an acceptor material (electron accepting, high electron mobility). They both can be environmental compatible[19] and more stable than perovskite based cells[23]. They started with only 2.5%[24] efficiency, but they are now exceeding the dye-sensitized solar cells giving now values up to 16.5%[25].

Recently, a lot of development was done in terms of acceptor materials, changing from fullerenes to non-fullerene acceptors, as they possess mostly a better stability, lifetime and more suitable absorption properties. Furthermore, the functionalization is much easier than with fullerenes[26]. A large group of acceptors are the perylene mono- and diimides, which are currently used as dyes in paint and varnish[27]. In this work, novel non-fullerene acceptors were investigated based on a perylene-monoimide-phenylene-perylene-monoimide structure.

2. Theoretical Background

2.1 Density Functional Theory

Density Functional Theory (DFT) is one of the most successful tools in computational chemistry nowadays, due to lower costs and shorter calculation times compared to other methods like Hartee-Fock (HF) theory. Since the 1990s, it increasingly gained importance and is now a key modeling method for calculations in quantum chemistry. The applications are ranging from the calculations of binding energies in molecules to the band structure of solids. Most successfully, DFT is used for predicting and understanding ground-state electronic structure properties of atoms, molecules and solid state materials[28,29].

2.1.1 The Schrödinger Equation

Like all wave function based quantum chemical methods, DFT is based on solving the time-independent, non-relativistic Schrödinger equation:

$$\hat{H}\Psi = E\Psi \tag{1}$$

$\hat{H}$ represents the Hamilton Operator and Ψ the wave function which contains all possible information about a given system[28] and comprises the solutions or so-called eigenstates of the Hamilton operator. These eigenstates have a corresponding eigenvalue E which is the total energy of the system. The Born-Oppenheimer approximation states that – due to the relatively large mass of protons and neutrons – the positions of the nuclei can be seen as fixed while the electrons move in the electrostatic field induced by the nuclei[30]. With this simplification, the Hamilton operator can be written as:

$$\hat{H} = -\frac{1}{2}\sum_{i}^{N}\nabla_i^2 + \hat{V}_{ext.} + \sum_{i<j}^{N}\frac{1}{|r_i - r_j|} \tag{2}$$

The Hamiltonian consists of three terms; the kinetic energy of the electrons ($\hat{T}$), the interaction with the external potential generated by the static nuclei ($\hat{V}_{ext.}$) and the electron-electron interaction (V_{ee}). The terms i and j denote the N electrons of the system and r stand for the respective radii[31].

To solve the Schrödinger equation and therefore calculate the total energy of a system, the wave function has to be known. Unfortunately, as the number of electrons (N) grows, the functions get more complicated due to higher dimensions. The exact wave functions are only known for one-electron systems like the hydrogen atom or H_2^+ molecule.

As it is too complex to search through all possible *N*-electron wave functions in larger, more-electron systems, the Hartree Fock approximation was developed to simplify the equation[32]. Nevertheless, the calculations using these methods are demanding for the computational resources; it is not yet possible to apply them on large and complex systems[28].

2.1.2 The Hohenberg-Kohn Theorem

The Hartree Fock method has its limitation in terms of complexity as well. In order to find the desired solution for the wave function, for each of the *N* electrons, *4N* variables, three spatial and one spin variable have to be taken into account. In case of the DFT method, only three spatial variables have to be solved[32].

This practical method was developed by Hohenberg and Kohn, who published the proof of this theory 1964 in the *Physical Review*. The Hohenberg-Kohn theorem states that the external potential is a unique functional of the ground-state density, making the density the key parameter in DFT on which all other variables can be based on[33]. Due to the use of the electron density, the many-body problem is reduced to only three spatial variables which are irrespective of the number of electrons. The independence of the system size allows the computation of more complex molecules[32].

2.1.3 Density Functional Theory – Functionals and Basis Sets

In the DFT plenty of different functionals were developed throughout the years. The most often used in quantum chemistry is B3LYP. It comprises the generalized-gradient approximation LYP for correlation with Becke's three-parameter hybrid functional B3 for exchange. The B3 functional mix a fraction of Hartree Fock exchange into the DFT exchange functional. Besides B3, other hybrid functionals exist with different combinations[28].

Basis sets can be classified by their number of basic functions used. The simplest sets, called *minimal sets*, utilize only one basis function. The more often used basis sets, *double-zeta* basis sets, double the set of functions using two instead of one function for each atomic orbital. It is assumed that only the valence orbitals need to be taken in account with two basic functions and core atomic orbitals with one, as they play the most important role. This limits the basis

set to the so called *split-valence* type sets (e.g. 3-21G, 6-31G). For most applications, those basis sets are augmented with polarization functions, called *polarized double-zeta* or *split-valence* basis sets (e.g. 6-31G(d,p))[32].

2.2 Suzuki-Coupling

The Suzuki-coupling is a Pd-catalyzed cross-coupling reaction between a bororganyl and an alkenyl/aryltriflate, -bromide or –iodide. Applicable bororganyls are alkenyl boronic acids and esters, aryl boronic acids and esters, as well as 9-borabicyclo[3.3.1]nonane dimer (9-BBN) derivatives. The commonly used catalyst for this reaction is tetrakis(triphenylphosphane)palladium $Pd(PPh_3)_4$. The general reaction is shown in **Scheme 1**[34].

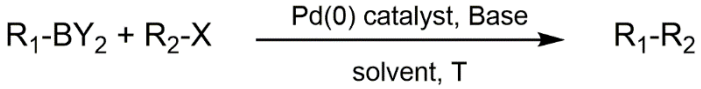

Scheme 1: General reaction scheme of the Suzuki-coupling; **R_1:** alkenyl, aryl, alkene; **R_2:** alkenyl, aryl, alkene

2.2.1 Cross-Coupling Reactions

The Suzuki-Miyaura coupling was first published by Miyaura et. al. in 1981. Beside this coupling reaction, other C-C-coupling methods are known, like the Negishi-coupling or Stille-coupling. The Negishi-coupling uses organozinc-compounds instead of organoborane compounds, leading to lower yields than the Suzuki-coupling[35].

In case of the Stille-coupling, tin complexes are used as substrates instead of boron containing compounds, which have a similar electronegativity. In both cases a similar mechanism as well as reaction scope is given[36]. However, an important drawback is the toxicity of organotin compounds[34]. In contrast, boronic acids and their esters are not only nontoxic, but can also be easily synthesized, are stable and cost effective. In addition, Suzuki-couplings can be run in aqueous media, as bororganyls are water soluble; high turnover rates are reached for the Pd-catalyst due to the reactivity of the bororganyls. There are not necessarily interfering byproducts, which allow one pot synthesis approaches and thus, reduce the time and chemical demand[35,37,38].

Apart from those advantages, the reaction has some limitations; for example: some alkyl borates do not show the desired reactivity, chloride substrates react slowly, decreasing the yield, and many side products can be formed in the absence of a base[37]. Another side reaction is the

beta-hydride elimination, which can occur in presence of a beta-hydride and competes with the reductive elimination which can reduce the yield drastically[39].

2.2.2 Mechanism of the Suzuki-Coupling

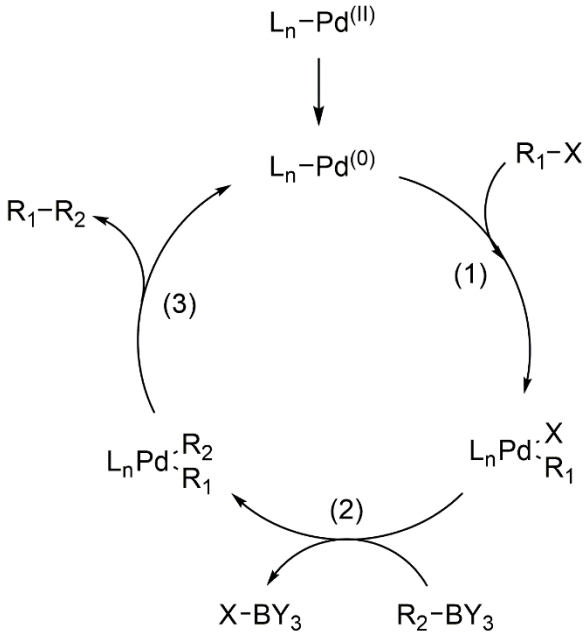

Scheme 2: General mechanism of the Suzuki-coupling with the substeps, (1) oxidative addition, (2) transmetallation and (3) reductive elimination[40].

The mechanism of the reaction consists of three fundamental steps (see **Scheme 2**): The oxidative addition of the substrate to the catalyst (1), the transmetallation, where the bororganyl is added to the catalyst (2) and the reductive elimination, giving the desired product and the catalyst (3)[40,41].

The oxidative addition is the rate determining step in the cycle. The reactivity depends on the atom/group 'X' on the organic compound, decreasing in the following order: I > Br > OTf > Cl > F[42].

2.2.3 Catalysts and its Ligands

Since the Suzuki-coupling was first introduced in the 1980's, a lot of research was going on in this topic; one field of it was the Pd catalyst design. The first catalyst used was $Pd(PPh_3)_4$; this one and [1,1′-Bis(diphenylphosphino)ferrocene]dichloropalladium(II) ($PdCl_2$(dppf)) proved to be very viable. In general, catalysts with an electron-rich Pd(0) center, or precursors thereof, and bulky ligands are widely used. The electron-rich center helps the oxidative addition reaction and the bulkiness increases the orbital overlapping on the metal which enables reductive

elimination[41]. Therefore, these features lead to higher turnover numbers and a lower required catalyst loading.

The ligands are categorized by the atom which is coordinated to the metal. There are three major classes: phosphine ligands, carbon ligands and nitrogen ligands. From those, the most prominent ones are the phosphine ligands. In first reports of the Suzuki reaction PPh_3 was used as a ligand. Since then many new modifications of it has been prepared in order to improve its properties. For example, the aromatic ring was replaced by a cyclohexane (PCy_3) or other, more electron-rich and bulkier alkyl groups[39,43,44]. In addition, palladacycles were developed with a good thermal stability, which are air stable, low cost and are environmentally friendly[45].

2.2.4 Reaction conditions

As mentioned before, the oxidative addition is the rate determining step in the Suzuki-coupling and the reactivity of the electrophilic partners for this step decrease in the following order: I > Br > OTf > Cl > F[42]. According to this, chlorine is one of the least reactive partner and a worse leaving group. To counteract on this behavior, bulky, electron rich phosphine ligands are used on the Pd catalyst and stronger bases are implemented[35].

In *B*-alkyl Suzuki reactions, the base plays an important role in many more steps throughout the Suzuki-coupling: It hydrolyses the $Pd^{II}X$ intermediate to the more reactive $Pd^{II}OH$ species; it is responsible for the complexation of BR_2OH side products and at last, it is used for the regeneration of the catalyst. Studies revealed that the reactivity of the base varies with the solvent used. For example, strong bases such as NaOH, TlOH and NaOMe perform best in THF or H_2O, whereas weak bases like K_2CO_3 and K_3PO_4 work best in DMF[37].

Palladium catalysts are the most widely used for Suzuki coupling, but also other metals have been shown to be catalytically active. For example, Ni, Ru, Fe and Cu. In addition, the performance of the coupling reaction depends on the reactivity of the bororganyl to conduct the transmetallation, too. It was shown that the reactivity is related to the Lewis acidity of the bororganyl, following that electron withdrawing groups increase the reactivity: $ArBF_3 > BR(OH)_2 > BR(OR)_2 > BR_3$[35].

2.3 Organic Solar Cells

Organic solar cells are photovoltaic devices used for the generation of electrical energy through solar irradiation. The devices consist of an active layer comprising two semiconductors, a donor and an acceptor material, embedded between two electrodes. Interfacial layers are frequently used between the photoactive layer and the respective electrodes.

2.3.1 Working Principle

The conversion of solar energy into electric energy in an organic solar cell is based on 6 different steps, as depicted in **Figure 1**. When light is absorbed, an electron-hole pair, called exciton, is generated (1). In some cases, mostly in the bilayer heterojunction, the exciton can recombine, leading to losses (2). The exciton diffuses to the interface between the donor and acceptor (3). At the interface, the exciton dissociates into electrons and holes (4), subsequently the separated charge carriers are transferred to the respective electrodes (5), where the charge carriers are finally collected (6)[46].

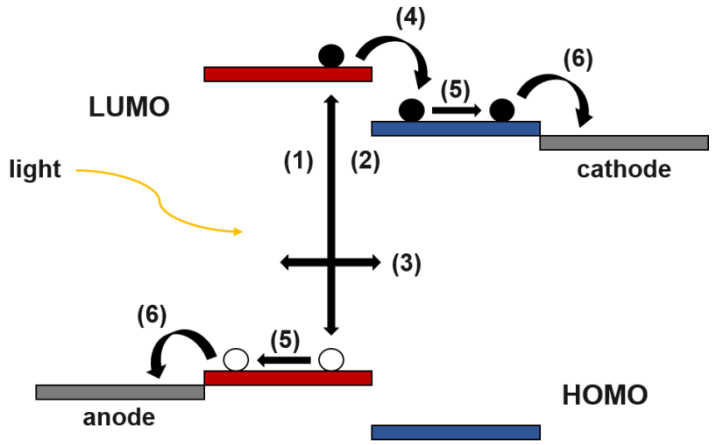

Figure 1: Schematic illustration of the photocurrent generation in an organic solar cell; (1) photon absorption and exciton generation, (2) exciton recombination, (3) exciton diffusion, (4) exciton dissociation, (5) charge transfer and (6) charge extraction[46,47].

2.3.2 IV Characteristics

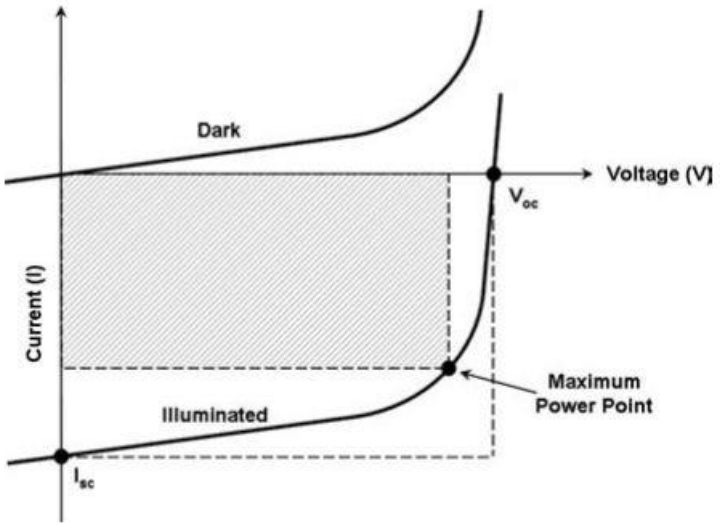

Figure 2: Schematic illustration of the IV characteristics of a solar cell[47].

In **Figure 2**, a schematic illustration of the IV characteristics is shown. Two parameters correlating to the IV characteristics are the open-circuit voltage (V_{OC}) and the short-circuit current (I_{SC}). The V_{OC} is the maximum voltage of a photovoltaic cell when no current is flowing. In contrast, the I_{SC} describes the maximum current the device can reach. In addition to these parameters, the maximum power point (mpp) can be observed, where the maximum power is produced. It is the product of voltage and current and can be referred to as the voltage on the maximum power point (V_{mpp}) and the current at the maximum power point (I_{mpp}). From these values, the fill factor (FF) can be determined:

$$FF\ [\%] = \frac{I_{mpp} * V_{mpp}}{I_{SC} * V_{OC}} \tag{3}$$

The probably most important parameter is the power conversion efficiency. It is the ratio between the electrical power output of the cell ($P_{el,out}$) and the incident solar irradiation (P_{in}), which are given in W/cm^2. The $P_{el,out}$ is described by the product of I_{mpp} and V_{mpp} (see **Equation 4**)[47].

$$PCE\ [\%] = \frac{P_{el,out}}{P_{in}} = \frac{I_{mpp} * V_{mpp}}{P_{in}} = \frac{I_{SC} * V_{OC} * FF}{P_{in}} \tag{4}$$

When it comes to solar cell parameters, usually the short-circuit current density (J_{SC}) [mA/cm^2] is given instead of the short-circuit current (I_{SC}) [mA]. This is due to the fact, that the parameter correlated with the electrode area is better comparable.

2.3.3 Device Design

In general, there are two prominent device designs for organic solar cells: the bulk and bilayer heterojunction. As depicted in **Figure 3**, the bilayer heterojunction possesses clearly defined layers of the donor and the acceptor, whereas in the bulk heterojunction a blend is made between those materials[47]. The charge separation takes place at the interface between the donor and acceptor phase[46]. In case of the bulk heterojunction, a larger interface is achieved. In addition, percolation pathways are built, which transports the electrons through the acceptor, and the holes through the donor phase. Due to this, a better charge separation is achieved[48,49].

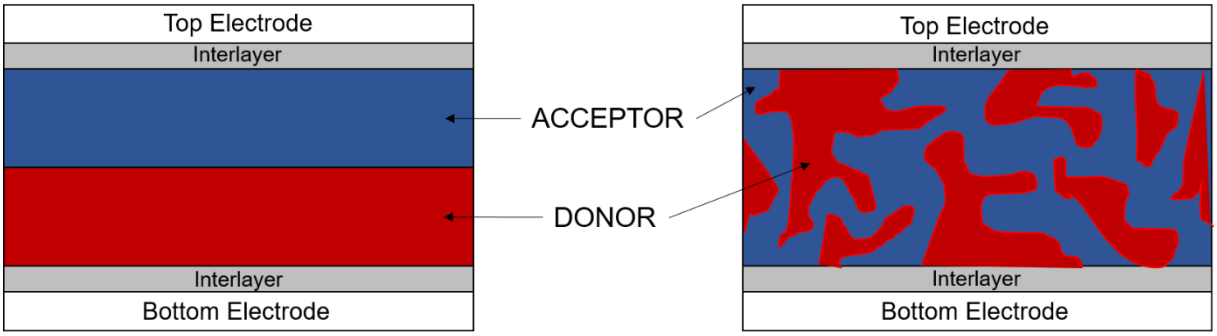

Figure 3: Schematic illustration of the bilayer (left) and bulk heterojunction (right).

In addition, the device can be assembled in an inverted or a normal structure. In the normal device structure, the bottom electrode is the anode and the top electrode the cathode (e.g. Al as top electrode). The inverted design possesses an anodic top electrode and a cathodic bottom electrode (e.g. Ag as top electrode). In this work, all substrates were assembled in the inverted design structure[48].

2.3.4 Interfacial Layer Materials

When it comes to interfacial layers, it is distinguished between p- and n-type interlayers. Prominent materials for n-type interfacial layers are metal oxides, like ZnO_x and TiO_x, which can absorb UV-light. Often used materials for p-type interlayers are transition metal oxides like MoO_3 and V_2O_5. The main reason for introducing interfacial layers, is the function as an

optical spacer, protection of the active layer from diffusion of the electrode material and prevention of leakage currents[49].

2.3.5 Electrode Materials

The most often used transparent electrode is indium tin oxide In_2O_3:Sn[50] (ITO). It is usually deposited on glass or transparent, flexible polymer substrates such as polyethylene terephthalate (PET). It has a lot of advantages, like a high transparency and conductivity, but it is less suitable for flexible devices due to its brittleness[48]. Alternatives would be for example poly(3,4-ethylenedioxythiophene)-poly(styrenesulfonate) (PEDOT:PSS) or carbon nanotubes (CNT)[49]. As top electrode, Ca and Mg would be suitable candidates, but they can easily be oxidized. Therefore, an alternative would be Al, Ag or Pd, respectively, which exhibit the most suitable V_{OC} and I_{SC} values. However, these parameters depend on the combination of the interfacial layer and the electrode as well[48].

2.3.6 Active Layer Materials

The active layer in an organic solar cell consists of a donor and an acceptor material. The donor material has to be a conjugated material to enable charge transport. In the choice of acceptor materials, it can be distinguished between fullerene and non-fullerene compounds with suitable absorption behavior.

2.3.6.1 Donor Materials

At first, simple polymers were used as donor materials, like poly(*para*-phenylene) (PPP), poly(*para*-phenylene vinylene) (PPV)[51,52], polythiophene[53,54] or polycarbazole[55,56] and certain derivatives. Throughout the research, the structures of the polymers used got more complex. Examples for frequently used donors are, PTB7, PTB7-Th[57,58] or PCE-12[59,60] (see **Figure 4**). The purpose behind the structural changes was the improvement of the IV characteristics and therefore the efficiency of the solar cell devices. This was achieved with band gap engineering and the adjustment of electron- and hole mobilities, as well as lowering the energetic orbitals. The suitable polymer donor molecule should exhibit a medium or low bandgap, high carrier mobility, matched energy levels and a good solubility[61].

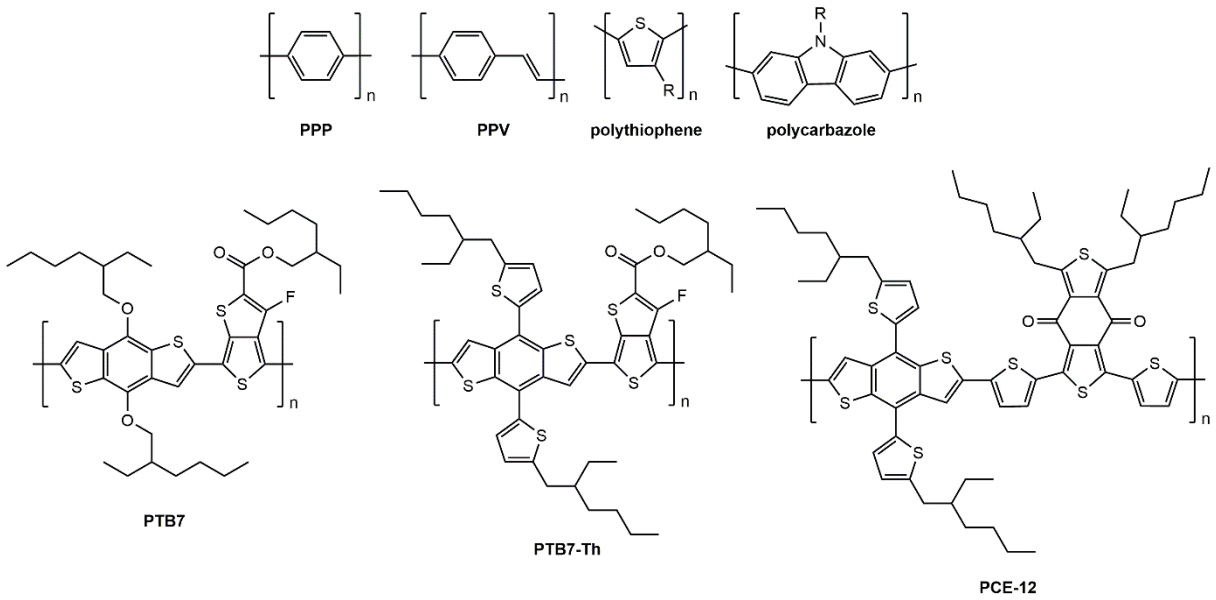

Figure 4: Structures of polymers used as donors in organic solar cells.

2.3.6.2 Acceptor Materials

Acceptor materials in organic solar cells function not only as absorber, but are responsible for the electron transportation to the respective electrode. Two major classes of acceptors can be distinguished: fullerene and non-fullerene/post-fullerene acceptors.

The first important acceptor materials were fullerene derivatives (see **Figure 5**), like phenyl-butyric-acid-methyl esters ($PC_{60}BM$, $PC_{70}BM$) and 1',1'',4',4''-tetrahydro-di[1,4]methano-naphthaleno[5,6]fullerene-C60 (ICBA). These materials possess lots of suitable characteristics for the application in solar cells. For example, they possess high electron mobilities, have 3D structures with delocalized π-electrons and are excellent electron acceptors. In contrast, they have high production costs, weak absorption properties and thermal, as well as photochemical instability[62,63].

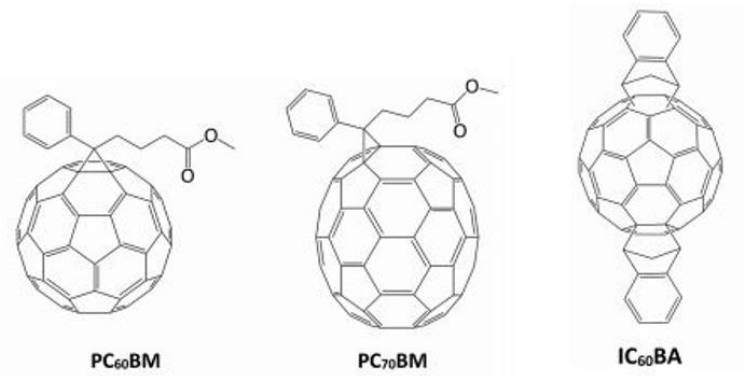

Figure 5: Examples for fullerene acceptors used in organic solar cells; image taken from reference 64 by F. Domínguez, et. al.[64].

Therefore, research is going now in the direction of non-fullerene acceptors, as they, unlike fullerenes, can be more easily adjusted and synthesized[62]. In addition, some of them possess a higher thermal stability and strong absorption in the visible range, which can be complementary to the absorption of donor molecules[63]. The most promising types of non-fullerene materials may be the 3,9-bis(2-methylene-(3-(1,1-dicyanomethylene)-indanone))-5,5,11,11-tetrakis(4-hexylphenyl)-dithieno[2,3-d:2',3'-d']-s-indaceno[1,2-b:5,6-b']dithiophene (ITIC) derivatives (see **Figure 6**), as well as halogenated compounds in general. By now, a power conversion efficiency of over 15%[25] was achieved using these compounds. Nevertheless, many other materials are investigated and are emerging the research area.

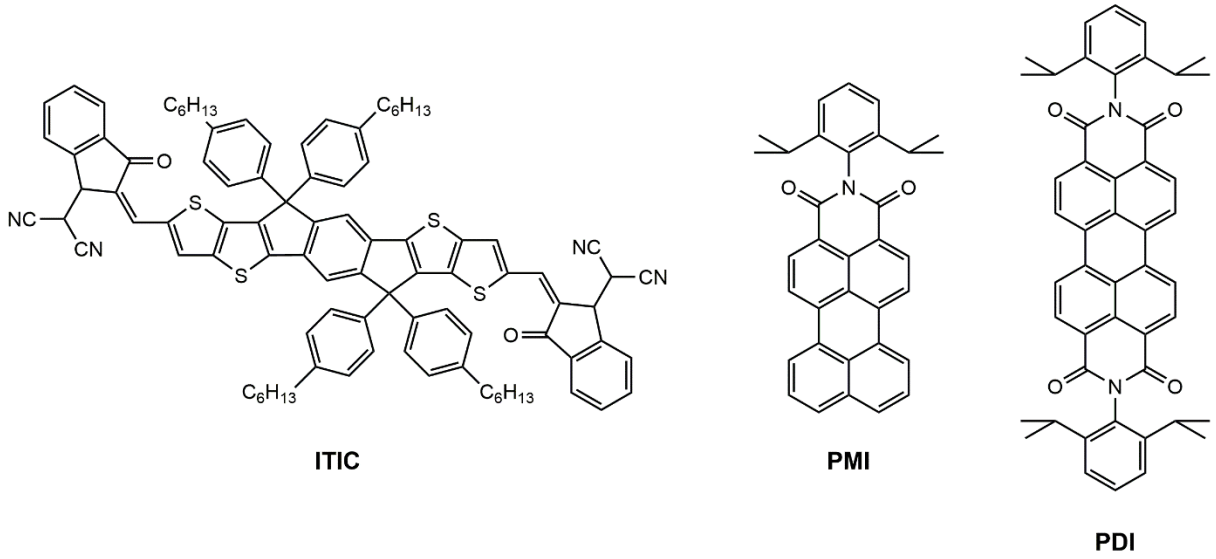

Figure 6: Examples for non-fullerene acceptors used in organic solar cells.

One example would be perylenes. Here, two major compounds are known and studied: the perylene diimides and perylene monoimides (see **Figure 6**). Both materials exhibit suitable absorption properties and have high temperature stability[62]. In addition, a lot of new functional groups can be introduced, and couplings between the PMI or PDI units are very prominent[65,66].

Recent studies of PMI units connected with different linkers gave promising results for the use as acceptor materials in organic solar cells. One example would be a fluorene linker, achieving a PCE of already 6% using different additives[67]. However, even without additives over 2% are reached. Beside the fluorene unit, aryl compounds were studied, like phenylene- and thiophene-based linkers (see **Figure 7**). Optical studies were done on these compounds, showing similar LUMO levels and absorption ranges. By now, the highest PCE of these molecules was obtained with a thiophene-linker (1.3%)[65].

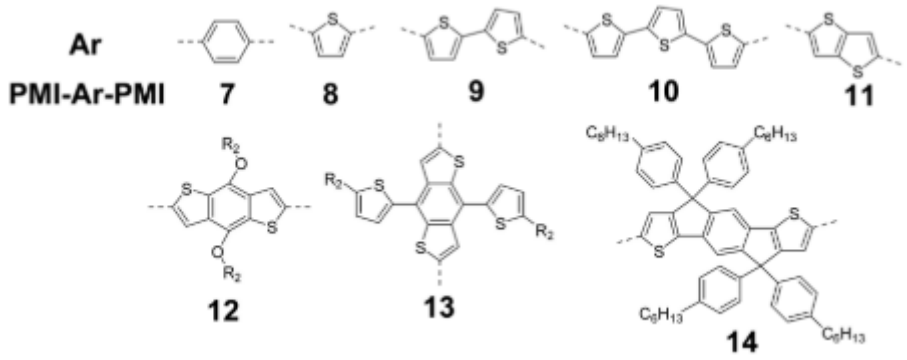

Figure 7: Examples for aryl linkers based on thiophene and phenylene units; image taken from reference 65 by Y. Hu, et. al[65].

3. Objective

Similar to the idea of Y. Zhang, et al.[67,68] and Y. Hu, et. al.[65], the use of perylene monoimide based acceptors in organic solar cells should be investigated. Therefore, four phenylene-linked perylene monoimide compounds should be synthesized and characterized (see **Figure 8**). Several measurements should be carried out including 2-dimensional NMR experiments for the identification of the molecular structure, as well as absorption and fluorescence spectroscopy for the determination of the optical properties. In addition, thermogravimetric analysis and differential scanning calorimetry should be applied to get an insight in the thermal properties. The optical experimental data should be correlated with computational methods for further investigation. At last, the synthesized acceptors should be assembled in photovoltaic devices, followed by the characterization of the cells and the investigation of influences of thermal annealing on the solar cell parameters.

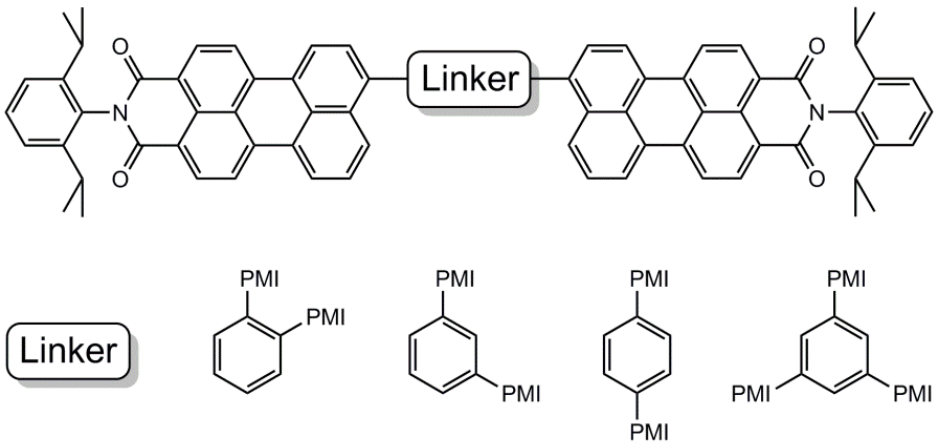

Figure 8: Graphical representation of all synthesized acceptors.

4. Results and Discussion

The goal of this work was to synthesize four different acceptors, characterize them and investigate their behavior in organic solar cells. These acceptors are based on a perylene-monoimide-phenylene-perylene-monoimide structure (see **Figure 8**). At start, those structures were geometrically optimized and optically characterized using DFT based computations. Consequently, the actual synthesis of these acceptors and the application in organic solar cells were carried out.

4.1 Computations based on Density Functional Theory

The main goal of the DFT-based computations was to get an insight in the geometrical configuration and the optical properties of the desired compounds. First, the molecules were geometrically optimized using Gaussian 09 with the B3LYP functional and the 6-31G* basis set. **Figure 9** depicts the optimized structures of all four targeted compounds.

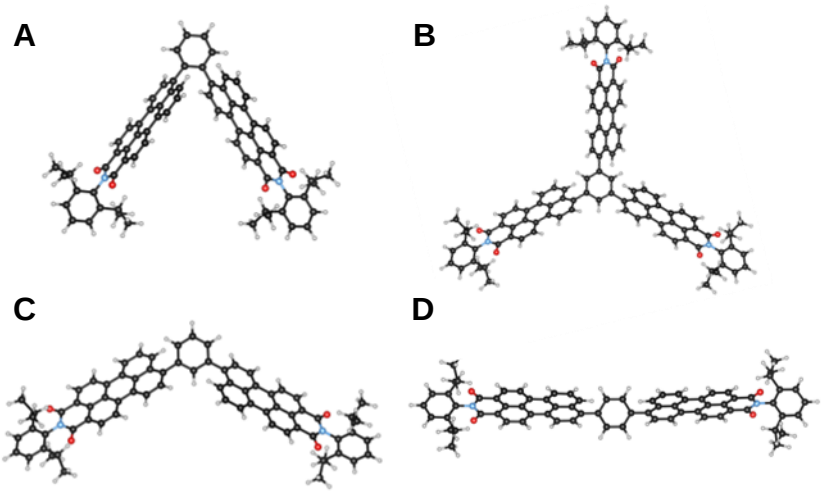

Figure 9: Optimized structures of all acceptors in the gas phase; **A**: PMI-oPh-PMI, **B**: $Ph(PMI)_3$, **C**: PMI-mPh-PMI, **D**: PMI-pPh-PMI.

The computed dihedral angles in the gas phase and in a solvent environment of chloroform are depicted in **Figure 10** and the respective values are given in **Table 1**. Only the PMI-pPh-PMI could not be calculated in solvent environment. Predicted values are nearly identical in gas and solvent ($CHCl_3$) environment. The meta- and para-linked PMI as well as the trimer show similar dihedral angles of about 54°. The ortho-linked PMI has an increased angle, most likely due to the steric hindrance between the PMI residues.

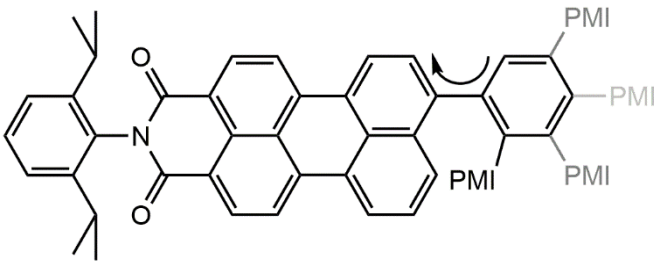

Figure 10: Graphical representation of the described angles for each acceptor.

Table 1: Results of the geometrical optimization; computations done on B3LYP level of theory using 6-31G* basis set.

Acceptor	**Angles (gas phase)**	**Angles (solvent)**
PMI-oPh-PMI	64°	64°
PMI-mPh-PMI	56°	55°
PMI-pPh-PMI	54°	-
$Ph(PMI)_3$	54°	53°

Second, the geometrically optimized structures were used for the calculations of the absorption maxima and the HOMO-LUMO levels. For this computations, a larger basis set was used (6-31+G*), comprising the diffuse functions of heavy atoms for more accurate results. This worked well for the acceptors which have only two PMI-residues but it reached the computational limits in case of the trimeric acceptor. Therefore, the calculations were repeated for all compounds with the smaller basis set 6-31G*. In addition, the same computation was done in a solvent environment of chloroform. The respective results for the larger basis set are shown in **Table 2** and for the smaller basis set in **Table 3**.

Table 2: Results of the DFT-based computations done on B3LYP level of theory using the basis set 6-31+G* in the gas phase.

Acceptor	**HOMO [eV]**	**LUMO [eV]**	**$E_G^{opt.}$ [eV]**	**$\lambda_{max}^{opt.}$ [nm]**
PMI-oPh-PMI	-5.80	-3.24	2.56	492
PMI-mPh-PMI	-5.84	-3.25	2.59	516
PMI-pPh-PMI	-5.81	-3.29	2.52	546

Table 3: Results of the DFT-based computations done on B3LYP level of theory using the basis set 6-31G* in the gas phase.

Acceptor	HOMO [eV]	LUMO [eV]	$E_G^{opt.}$ [eV]	$\lambda_{max}^{opt.}$ [nm]
PMI-oPh-PMI	-5.52	-2.90	2.62	477
PMI-mPh-PMI	-5.56	-2.91	2.65	502
PMI-pPh-PMI	-5.53	-2.96	2.57	532
$Ph(PMI)_3$	-5.66	-3.03	2.63	502

All acceptors have similar HOMO-LUMO levels (**Table 2**) and therefore similar band gaps. The absorption maxima are shifted to longer wavelengths from the ortho- to the meta- and the meta- to the para-linked PMI. In **Table 3**, similar results are shown for the HOMO-LUMO levels and the optical band gap with the difference that both HOMO and LUMO levels are slightly increased compared to the calculations with the larger basis set. The values of the optical band gaps deviate highest by 0.05 eV. As mentioned above, the maxima are red-shifted from the ortho- to the para-linked PMI in case of the computation with the basis set 6-31+G*; the same results are given for the smaller basis set 6-31G*.

With the smaller basis set 6-31G* it was possible to compute the trimeric acceptor as well. Compared to the other acceptors, the HOMO and LUMO levels of the trimer are reduced and the band gap shows a similar value. The absorption maximum is at 502 nm, which is the same as for the meta-linked PMI.

Table 4: Results of the DFT-based computations done on B3LYP level of theory using the basis set 6-31G* in a solvent environment of chloroform.

Acceptor	HOMO [eV]	LUMO [eV]	$E_G^{opt.}$ [eV]	$\lambda_{max}^{opt.}$ [nm]
PMI-oPh-PMI	-5.46	-2.89	2.57	502
PMI-mPh-PMI	-5.48	-2.88	2.60	517
PMI-pPh-PMI	-	-	-	-
$Ph(PMI)_3$	-5.54	-2.94	2.60	530

The results of the computations in a solvent environment of chloroform (see **Table 4**) are comparable to the values in the gas phase. The HOMO-LUMO levels are slightly shifted to higher values and the maximum absorption is increased. However, the results are in the same range. The computations in the solvent were not successful for the PMI-pPh-PMI.

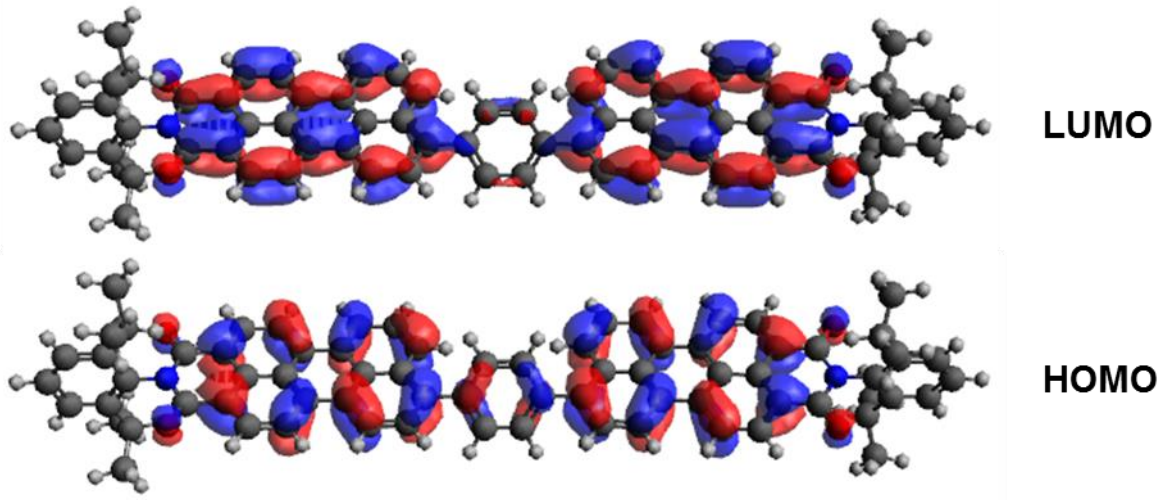

Figure 11: Graphical representation of the HOMO-LUMO levels of the para-linked PMI.

In **Figure 11** the HOMO and LUMO levels of the para-linked PMI are shown. The levels are representative for all acceptors, excluded the trimeric PMI. As expected, the molecule is fully conjugated in its HOMO level but the electronic density is mainly located on PMI upon excitation to the LUMO.

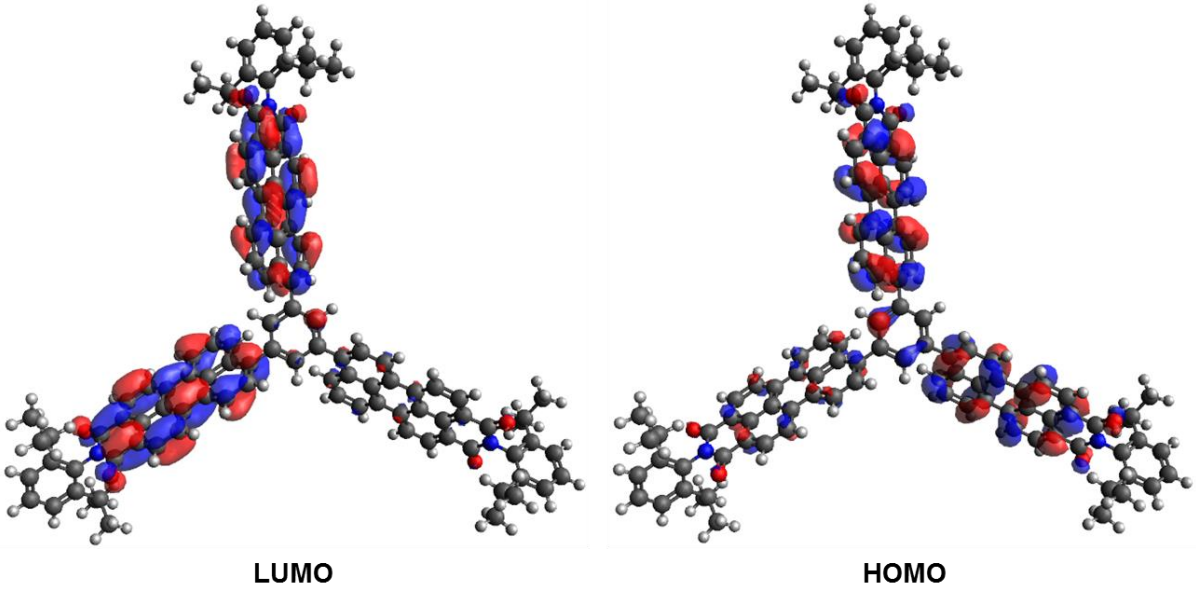

Figure 12: Representation of the HOMO-LUMO levels of the $Ph(PMI)_3$.

The graphical representation (see **Figure 12**) of the orbitals of the $Ph(PMI)_3$ indicate, that the molecule may be not fully conjugated in its non-excited state. In the visualization it is not clear if the third PMI contributes to the conjugated system or not. An electron density is

shown, but with very small coefficients. Nevertheless, the higher electron density shift in the direction of the third PMI unit in the excited state.

The trimeric compound could not be computed with the larger basis set (6-31+G*) due to the increased number of atoms compared to the other compounds. The complexity of the computation is also reflected in the CPU time used for each computation (see **Table 5**). Using the larger basis set, the calculation of the absorption properties needs 6 – 8 days, whereas the calculations with the smaller basis set could be achieved in less than one day for the smaller acceptors. Comparing the computations in gas phase with the values for the compound in a solvent environment, the calculations can be carried out in approximately the same time.

Table 5: Comparison of the CPU time needed for each computation of the absorption properties concerning the different basis sets and environments (solvent = $CHCl_3$).

Acceptor	**6-31+G* (gas phase)**	**6-31G* (gas phase)**	**6-31G* (solvent)**
PMI-oPh-PMI	8 d, 11 h, 45 min	19 h, 35 min	19 h, 56 min
PMI-mPh-PMI	6 d, 7 h, 7 min	18 h, 51 min	13 h, 53 min
PMI-pPh-PMI	6 d, 3 h,	17 h, 46 min	-
$Ph(PMI)_3$	-	2 d, 3 h, 8 min	2 d, 9 h, 39 min

The absorption properties of the PMI and PMI-Br were computed by Stefan Weber on B3LYP level of theory with the smaller basis set (6-31G*) in the gas phase, to compare those precursors with the different acceptors (see **Figure 13**). The PMI has the highest energy levels and the widest optical band gap of all material. When it is brominated, the levels and the optical band gap are decreasing slightly, which was as expected[69,70]. When the PMI is linked via a phenylene, the optical band gap decreases further and the HOMO-LUMO level are increasing for all acceptors except for the $Ph(PMI)_3$; the $Ph(PMI)_3$ shows lower HOMO-LUMO levels than all other compounds shown in this example. This could be due to the additional PMI unit on the linker.

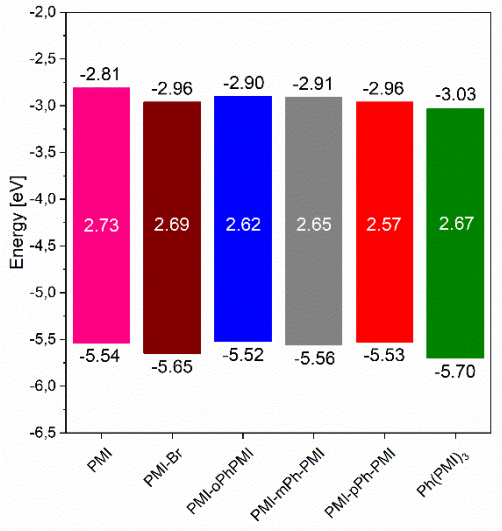

Figure 13: Graphic representation of the calculated (B3LYP, 6-31G*) HOMO-LUMO levels and the respective band gap of each material.

The absorption maximum of the PMI is at 485 nm and the brominated PMI has a red shift to 511 nm. Compared to the desired acceptors, the maximum of the PMI lies between the PMI-oPh-PMI and the PMI-mPh-PMI/$Ph(PMI)_3$ and has the exact calculated value as PMI-pPh-PMI.

4.2 Synthesis of Perylene Monoimide Acceptors

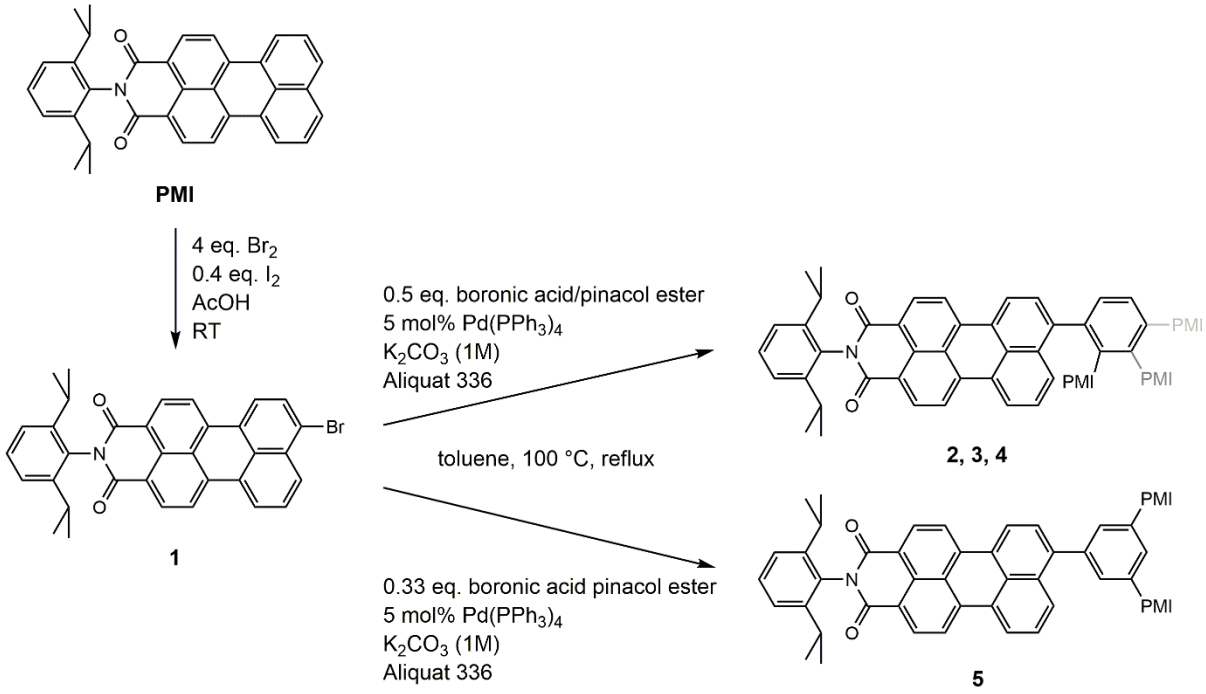

Scheme 3: Overview of the synthesis of the acceptors with the respective reaction conditions.

The synthesis of the desired acceptors was done as depicted in **Scheme 3**. The starting material was the perylene monoimide, which was brominated in the first step in acetic acid at room temperature (r.t.) using 4 eq. Br_2 and 0.4 eq. I_2. After 17 h, the TLC indicated full conversion and the product could be isolated at quantitative yield. To get to compounds **2 – 5**, a Suzuki-coupling was performed with compound **1** and the respective boronic acid/boronic acid pinacol ester as substrates. The catalyst was $Pd(PPh_3)_4$ and as base 1 M K_2CO_3 was used. The reaction was performed in toluene at 100 °C (reflux). The Aliquat 336 was applied to enable the phase-transfer of the base from the organic to the aqueous layers and vice versa. The synthesis of the PMI-pPh-PMI (compound **4**) was carried out by Matiss Reinfelds and is therefore not discussed further.

Compound **3** was the first synthesis performed; the bororganyl 1,3-benzenediboronic acid was used and the reaction performed 17.5 h. However, no full conversion was achieved and two side products were observed on the TLC. To isolate a pure product, separation was done via flash chromatography (toluene/acetone). Anyhow, the separation was not successful; due to this, several recrystallization steps were done with the different fractions collected from the column, finally yielding 117 mg (11%) of pure PMI-mPh-PMI.

The synthesis of PMI-oPh-PMI (compound **2**) was analogous to that of compound **3**, with the only exception that 1,2-benzenediboronic acid, bis(pinacol ester) was used as bororganyl. The

reaction was performed for 68 h, in order to achieve a full conversion. However, after 68 h the TLC indicated that still traces of the starting material were present in the reaction mixture. The purification was done via flash chromatography. The TLC indicated the presence of another side product and the chromatography was repeated. A ^{1}H-NMR spectrum (500 MHz) showed that the fraction isolated from the column was not purified completely; therefore, a recrystallization step was done, giving 139 mg pure compound **2** (30% yield).

The third reaction (synthesis of compound **5**) was done with 1,3,5-phenyltriboronic acid, tris(pinacol)ester under similar conditions as the other acceptors. The purification via column chromatography was carried out twice. However, 55 mg (8% yield) of the product with small impurities were isolated in the end (see **Figure 39** in the Appendix). All further experiments regarding the $Ph(PMI)_3$ were carried out using this fraction.

Overall, the Suzuki-coupling gave only very small yields (8 – 30%). However, due to temporal limitation, not all fractions of the products were purified. In addition, a variety of side products were formed in the reaction. According to literature, similar Suzuki reactions gave yields of about 65 – 82%[65,71,72], thus, the reaction needs optimization regarding the reaction conditions.

During the experiments it was observed that the solubility depends on the different positions of the PMI unit on the phenylene and increases in the following order: para < meta < ortho = trimer. This could be due to the differences in steric hindrance of the PMI units in vicinal positions. In the para-linked PMI, the PMI units do not interfere with each other enabling π-π stacking, which can decrease the solubility. In case of PMI units in meta-position to each other, there is no or low interaction between the PMI groups. The ortho-PMI product exhibits the highest solubility of all acceptors, as π-π stacking is not possible due to steric hindrance. $Ph(PMI)_3$ has good solubility in CH_2Cl_2 and $CHCl_3$; due to its bulkiness the stacking is not as efficient as in the PMI-mPh-PMI or PMI-pPh-PMI[65].

4.2.1 Structural Properties

The purity and nature of the synthesized acceptors were investigated by NMR experiments. The ^{1}H-NMR spectra of the brominated PMI, the PMI-mPh-PMI, PMI-pPh-PMI and $Ph(PMI)_3$ look alike, with differences concerning the hydrogens on the phenylene linker in the aromatic region (all spectra shown in the Appendix). In contrast, the aromatic signals of the PMI-oPh-PMI look different, as a lot more peaks occur (see **Figure 14**). This splitting of the aromatic peaks is most likely due to steric hindrance and the presence of isomers[71].

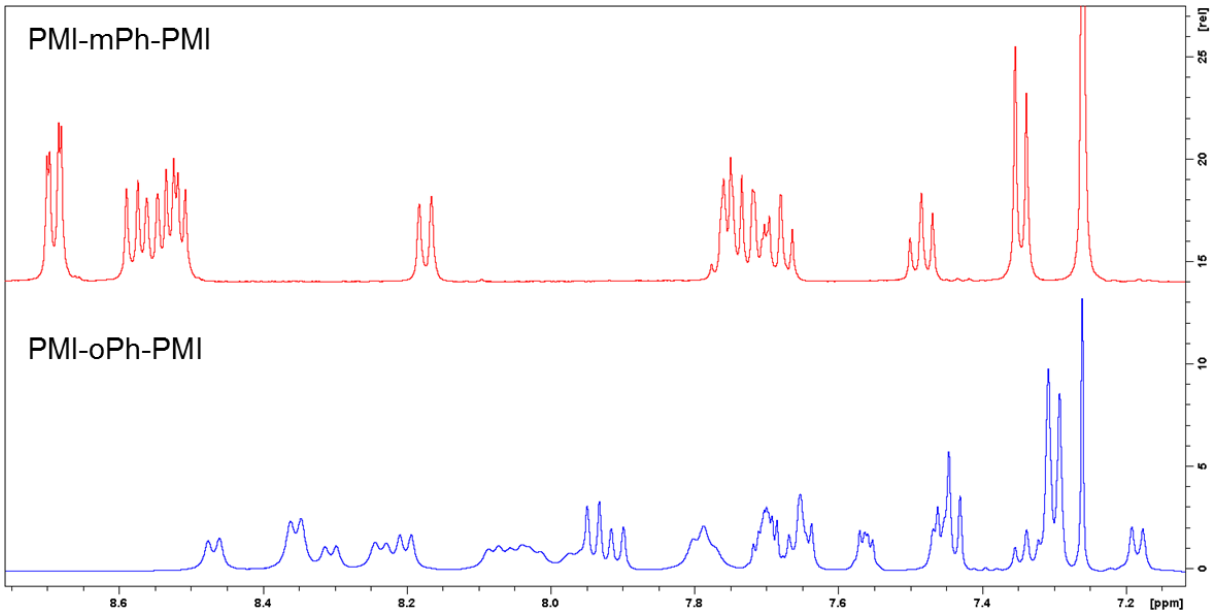

Figure 14: Comparison between the aromatic regions of the ^{1}H-NMR spectra of PMÍ-mPh-PMI (red) and PMI-oPh-PMI (blue), respectively.

4.2.2 Optical Properties

To characterize the materials, absorption spectra were recorded in chloroform ($CHCl_3$). Knowing the concentrations of the acceptors and the absorptions of each sample, the molar absorption coefficients could be determined. In **Figure 15**, the absorption spectra of all compounds are depicted. The PMI-mPh-PMI, PMI-pPh-PMI and $Ph(PMI)_3$ show a similar absorption behavior. They all have a broad absorption peak with two maxima. The highest maximum in the visible range for PMI-pPh-PMI is at 530 nm and for PMI-mPh-PMI and $Ph(PMI)_3$ at 527 nm. The lower maximum lies at 504 nm, 500 nm and 500 nm for the PMI-pPh-PMI, PMI-mPh-PMI and $Ph(PMI)_3$, respectively. The PMI-oPh-PMI gives a broad absorption peak as well, with the absorption maxima at 490 nm and 526 nm. The higher absorption is observed at the lower wavelength. Compared to PMI itself and the brominated PMI, which have their absorption maxima at 487 nm and 510 nm, the maxima of all acceptors are slightly red-shifted. PMI and PMI-Br both have a broad peak and at about 450 nm a shoulder can be seen. The spectra show more similarity to the absorption spectra of the ortho-linked PMI. In **Figure 15B**, the cyan line indicates the behavior of a PMI linked with a phenyl-ring (Ph(PMI)). Similar to the other linked PMIs, the spectrum is shifted to longer wavelengths and like for PMI and PMI-Br, a shoulder at approximately 450 nm is observable.

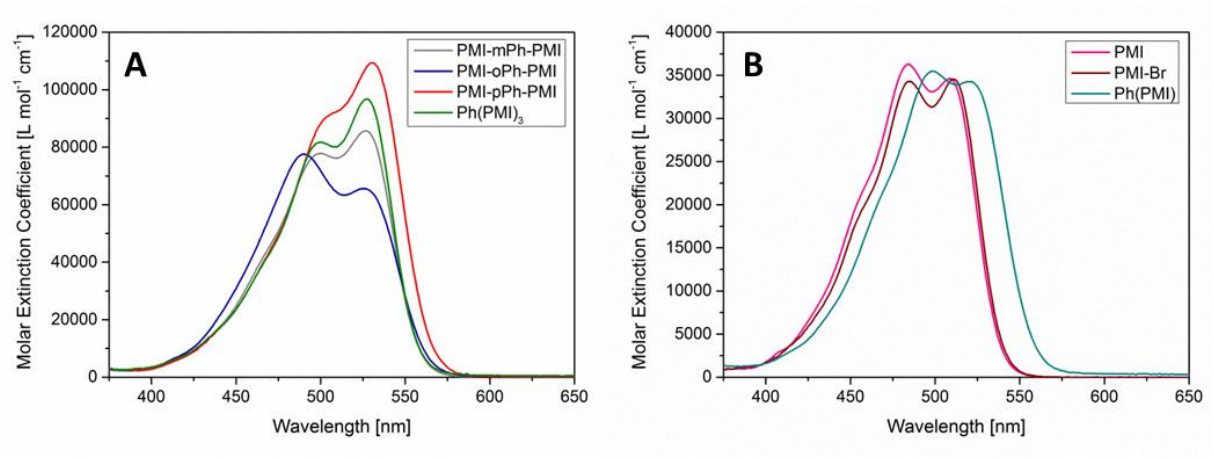

Figure 15: A: Absorption spectra of each acceptor dissolved in chloroform; blue: PMI-oPh-PMI, grey: PMI-mPh-PMI, red: PMI-pPh-PMI, green: $Ph(PMI)_3$; **B:** Absorption spectra of pink: PMI, brown: PMI-Br and cyan: Ph(PMI) dissolved in chloroform; PMI and PMI-Br measured by Matiss Reinfelds.

The molar absorption coefficient (ε) is the highest with about 109 300 L mol^{-1} cm^{-1} for the para-linked PMI, followed by 96 700 L mol^{-1} cm^{-1} of the $Ph(PMI)_3$, 85 700 L mol^{-1} cm^{-1} of the meta-linked PMI and 77 600 L mol^{-1} cm^{-1} of the ortho-linked PMI. This shows that ε increases with decreasing steric hindrance and increases with an additional PMI unit. This assumption correlates with the optical properties of the PMI, PMI-Br and Ph(PMI); all have a lower ε than the acceptors shown in **Figure 15A**. Of those three compounds, PMI-Br has the lowest ε with about 34 100 L mol^{-1} cm^{-1}. The PMI and Ph(PMI) have a similar ε values with about 35 900 and 35 500, respectively.

The optical band gap ($E_G^{opt.}$) was determined graphically for all acceptors, as well as for PMI, PMI-Br and Ph(PMI). Therefore, a tangent was applied where the peak flattens out. Where the tangent is intersecting the x-axis, the wavelength is taken and transformed into eV. In **Table 6** the results of this experiments are shown, as well as the computed data for all acceptors, PMI and PMI-Br in the gas phase (6-31+G*, 6-31G*) and the solvent $CHCl_3$ (6-31G*). The experimentally determined optical band gap is similar for all compounds, ranging from 2.20 to 2.30 eV. The PMI and PMI-Br results show the strongest deviation between all experimentally determined results. The computed band gaps are slightly higher than the experimental data. The computations with the larger basis set (6-31+G*) in the gas phase give similar values to the computation in the solvent (6-31G*) showing the same trend. However, the band gaps do not differ drastically from each other.

Table 6: Optical band gaps determined graphically from absorption spectra and by DFT based computations in the gas phase (6-31+G*, 6-31G*) and in $CHCl_3$ (6-31G*).

Acceptor	**$E_G^{opt.}$ [eV] (experimental data)**	**$E_G^{opt.}$ [eV] (DFT/gas phase/6-31+G*)**	**$E_G^{opt.}$ [eV] (DFT/gas phase/6-31G*)**	**$E_G^{opt.}$ [eV] (DFT/in CF/ 6-31G*)**
PMI-oPh-PMI	2.20	2.56	2.62	2.57
PMI-mPh-PMI	2.22	2.59	2.65	2.60
PMI-pPh-PMI	2.20	2.52	2.57	-
$Ph(PMI)_3$	2.23	-	2.63	2.60
Ph(PMI)	2.23	-	-	-
PMI	2.30	-	2.73	-
PMI-Br	2.30	-	2.69	-

The absorption maxima were computed in the gas phase with different basis sets (6-31+G*, 6-31G*) and in $CHCl_3$ (6-31G*) (**Table 7**). The computation in the gas phase using the larger basis set 6-31+G* gave similar results to the experimentally determined maximum for the absorption maximum of PMI-oPh-PMI. The PMI-mPh-PMI and PMI-pPh-PMI are under- and overestimated, respectively. However, the trend of increasing absorption maxima (ortho > meta > para) is given. With the smaller basis set 6-31G* in the gas phase, the calculated maxima deviate from the experimental data as well, giving smaller values for all acceptors. However, a similar shift for PMI-mPh-PMI and $Ph(PMI)_3$ is observable. This deviation was expected, as the used basis set comprises fewer functions. The computations in $CHCl_3$ correlate again to the experimentally determined maxima and the computation with 6-31+G* in the gas phase. This may be caused by the consideration of the interactions with the solvent, even though the smaller basis set was used. According to these results, the best computational data may be achieved using the 6-31+G* basis set in the solvent $CHCl_3$. However, this would increase the required CPU time for the calculations drastically.

In **Table 7**, the lower maxima in the visible range are listed in brackets. The computations showed for half of the acceptors one absorption maximum in the visible range. Only for the PMI-pPh-PMI a second maximum was observed for the computations in the gas phase. In the computations of PMI-oPh-PMI two shoulders were observed at higher wavelengths than the maximum. Those are at about 518 nm, 520 and 503 nm, as well as at 555 nm, and 555 nm and 541 nm for the larger basis set in the gas phase, the smaller basis set in the solvent and the smaller basis set in the gas phase, respectively. The computations of the absorption spectra of PMI-mPh-PMI and $Ph(PMI)_3$ showed only one maximum.

Table 7: Results of the absorption maxima determined experimentally in $CHCl_3$ and by DFT based computations in the gas phase (6-31+G*, 6-31G*) and in $CHCl_3$ (6-31G*); the highest maxima in the visible range are listed, the smaller absorption wavelengths in brackets.

Acceptor	$\lambda_{max}^{opt.}$ [nm] (experimental data)	$\lambda_{max}^{opt.}$ [nm] (DFT/gas phase/6-31+G*)	$\lambda_{max}^{opt.}$ [nm] (DFT/gas phase/6-31G*)	$\lambda_{max}^{opt.}$ [nm] (DFT/in CF/ 6-31G*)
PMI-oPh-PMI	490 (526)	492 (518, 555)	477 (503, 541)	502 (520, 555)
PMI-mPh-PMI	527 (500)	516	502	517
PMI-pPh-PMI	530 (504)	546 (498)	532 (485)	-
$Ph(PMI)_3$	527 (500)	-	502	530

Fluorescence spectra were recorded for each compound in $CHCl_3$; and the relative quantum yield (Φ) was calculated from the obtained data. In **Figure 16** the absorption and fluorescence spectra are shown; the dashed line represents the fluorescence; in blue: PMI-oPh-PMI, in grey: PMI-mPh-PMI, in red: PMI-pPh-PMI and in green: $Ph(PMI)_3$. The Stokes-shift of the PMI-oPh-PMI, PMI-mPh-PMI, PMI-pPh-PMI and $Ph(PMI)_3$ are 41 nm, 34 nm, 42 nm and 31 nm, respectively. The shift varies only a few nm for all acceptors.

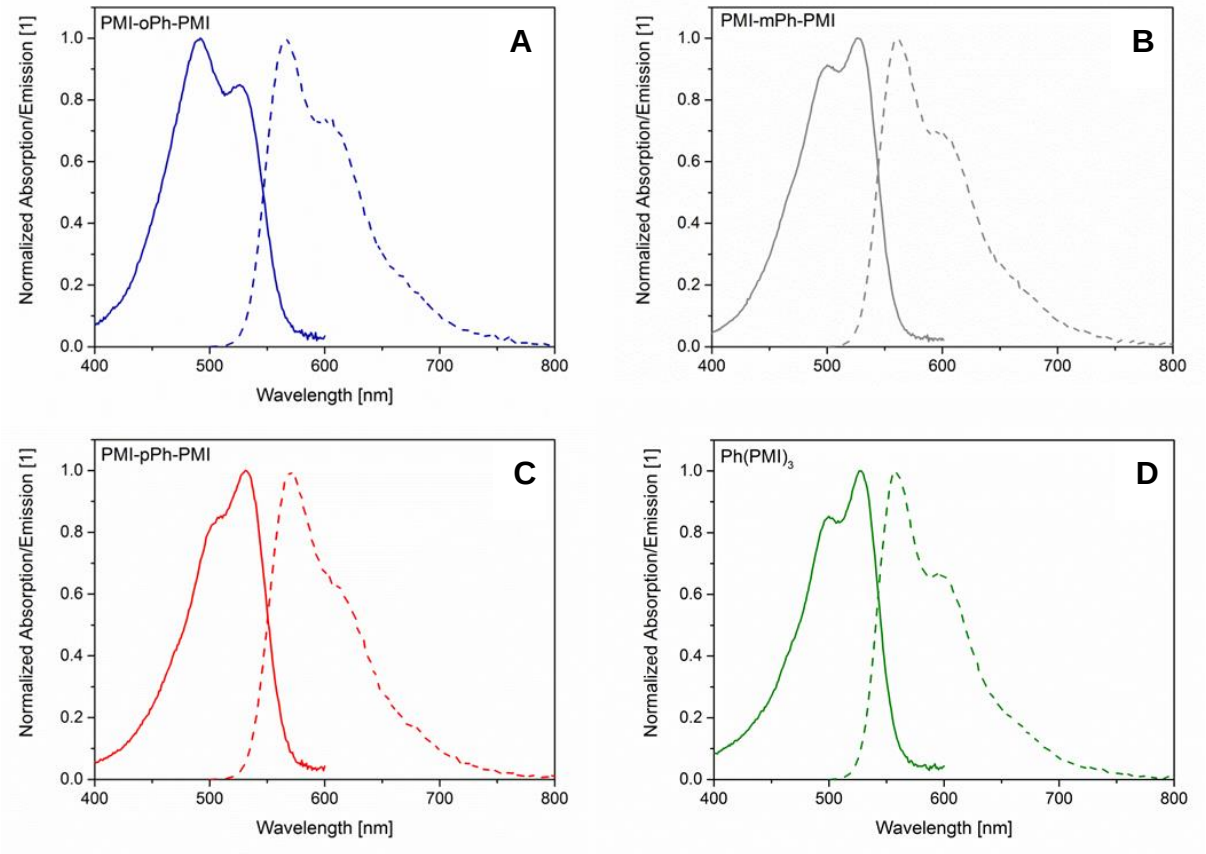

Figure 16: Absorption (filled line) and fluorescence spectra (dashed line) of each acceptor in solution ($CHCl_3$); **A:** PMI-oPh-PMI, **B:** PMI-mPh-PMI, **C:** PMI-pPh-PMI, **D:** $Ph(PMI)_3$.

Table 8: Quantum yield (Φ), calculated from the fluorescence spectra.

Acceptor	**Φ [%]**
PMI-oPh-PMI	77
PMI-mPh-PMI	80
PMI-pPh-PMI	78
$Ph(PMI)_3$	81

Like the absorption properties and the Stokes-shift, the relative quantum yield is similar for all acceptors, giving values between 77% and 81% (**Table 8**). The highest quantum yield is observed for the $Ph(PMI)_3$. The reference used for the measurements was 'Fluoreszenzorange', which is a PDI compound with a quantum yield of over 90%[73].

4.2.3 Thermal Properties

The synthesized compounds were characterized using thermogravimetric analysis (TGA) and differential scanning calorimetry (DSC). In **Figure 17** the results of the TGA measurement coupled with a DSC are shown for each acceptor. **Figure 17A** shows the TGA curve (blue) of the PMI-oPh-PMI and a high mass loss beginning at a 100 °C. This may be caused by solvents which remained in the sample. At 360 °C, about 10% of the total mass are lost before the compound starts melting at 515 °C and subsequently decomposes (32% mass loss in total). This is also shown in the corresponding DSC curve. In addition, a small deflection occurs at 200 °C, which could indicate a glass transition temperature (T_G).

In case of PMI-mPh-PMI (**Figure 17B**) there is no mass loss observed before 460 °C. In the corresponding DSC curve, an endothermic peak can be seen at 430 °C, where the compound starts to melt. Here, the decomposition occurs not subsequently but 30 °C higher with a total mass loss of 20%. In addition to the TGA coupled with DSC, a DSC measurement was carried out with more cycles, where a T_G was observed at 311.1 °C. In **Figure 17C**, the TGA and DSC of PMI-pPh-PMI can be seen. It shows similar behavior as the curves of PMI-oPh-PMI and PMI-mPh-PMI. The compound melts at 500 °C prior to the decomposition with a total mass loss of 19.5%. The DSC measurement with more than one cycle did not show a T_G.

In the fourth graph (**Figure 17D**) the TGA and DSC results of $Ph(PMI)_3$ can be seen. As for the TGA of PMI-oPh-PMI, a mass loss of about 20% is detected beginning below 100 °C. In the DSC curve, it can be seen that the sample contains still some impurities. However, a melting range can be determined from 310 – 390 °C. It is most likely that the compound starts to decompose at 460 °C and an additional mass loss of 10% is observed.

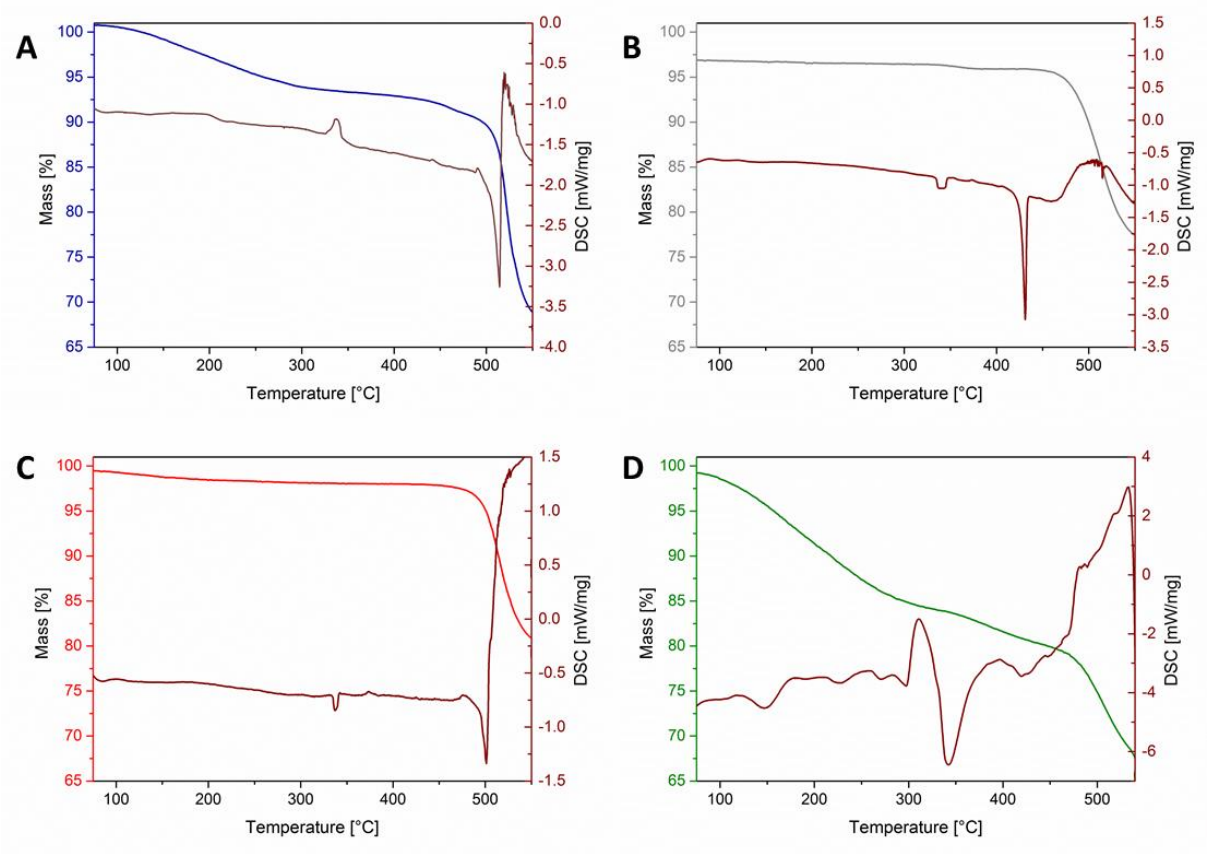

Figure 17: Graphical representation of the TGA coupled with a DSC; **A:** PMI-oPh-PMI, **B:** PMI-mPh-PMI, **C:** PMI-pPh-PMI, **D:** $Ph(PMI)_3$.

4.3 Organic Solar Cells

The assembly of the solar cell devices is described in *Chapter 5.4.1: General Procedure*. All devices were made in a bulk heterojunction inverted device design (see **Figure 18**). ITO-coated glass substrates were used, which were first coated with ZnO as an electron transport layer (ETL), then with the active layer followed by the hole transport layer (HTL) MoO_3 and the top electrode Ag.

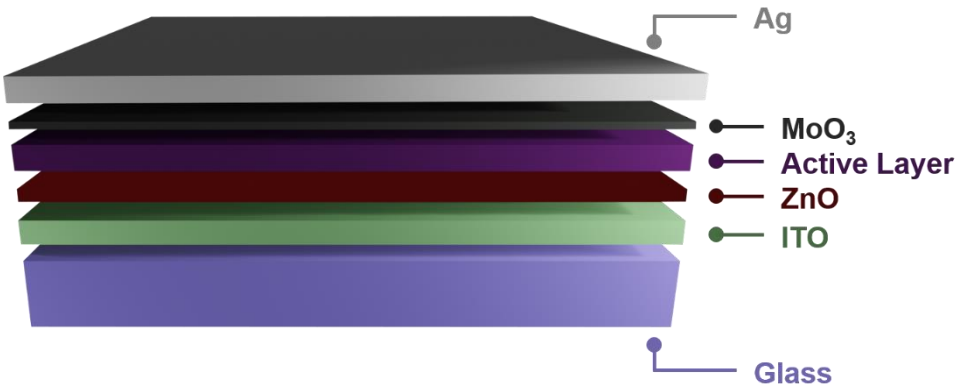

Figure 18: Schematic illustration of the device design of all assembled solar cells in this work.

4.3.1 PMI-oPh-PMI

For the first organic solar cells with the PMI-oPh-PMI (experiment 1), the acceptor was dissolved in chlorobenzene (CB) in a concentration of 12 mg/mL (results are shown in **Table 9**). Although the solubility should be better for this PMI derivative compared to PMI-mPh-PMI and PMI-pPh-PMI, the solid was not fully dissolved, even under heating (50 °C). Therefore, the mixture was filtered to obtain smooth films. For the next solar cells, the concentration was decreased to 10 mg/mL and the used solvent was chloroform. Using $CHCl_3$, the acceptor dissolved immediately without any further heating step. However, the application of the active layer with $CHCl_3$ was rather difficult, resulting in much higher active layer thicknesses (see **Table 9**).

Table 9: IV characteristics, annealing temperature and active layer thickness of the assembled solar cells with the active layer consisting of PMI-oPh-PMI and PCE-12 1:1 with an acceptor concentration of 10 and 12 mg/mL; the parameters of the cell with the highest PCE are shown in brackets; the values are averaged over 5 cells.

Experiment	V_{OC} [V]	I_{SC} [mA/cm^2]	FF [%]	PCE [%]	T [°C]	Thickness [nm]
1	1.01 (1.04) ± 0.02	2.38 (2.62) ± 0.16	41 (40) ± 1	0.98 (1.08) ± 0.06	150	142
2	0.87 (0.89) ± 0.05	1.73 (1.74) ± 0.06	32 (32) ± 1	0.47 (0.49) ± 0.02	150	252

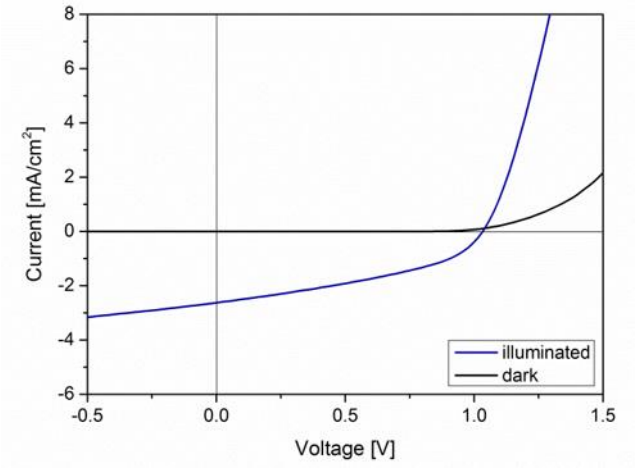

Figure 19: IV characteristics of the best solar cell with the PMI-oPh-PMI acceptor (experiment 2) of the dark measurement (black) and the illuminated measurement (blue), respectively.

The IV characteristics of the best assembled solar cells concerning the power conversion efficiency (PCE) are depicted in **Figure 19**. In the first try with CB as solvent a layer thickness between 100 and 150 nm was achieved. The substrate with the highest PCE had an active layer thickness of 142 nm, a PCE of 0.98%, a fill factor (FF) of 41% and a high open circuit voltage with 1.01%. These values are slightly higher than for the substrate with 100 nm layer thickness, reaching only 0.56% PCE, 36% FF and 0.93 V_{OC}.

When the acceptor was dissolved in $CHCl_3$ with a concentration of 10 mg/mL, the most promising substrate had a layer thickness of 252 nm. The assembling was more difficult, as $CHCl_3$ evaporates much faster, giving less smooth and worse distributed films. The best PCE achieved was 0.49%. The FF was rather low with 32% and the V_{OC} decreased to 0.87 V. The two experiments are not very suitable for comparison, as the concentration of the acceptor could not be determined for the first experiment.

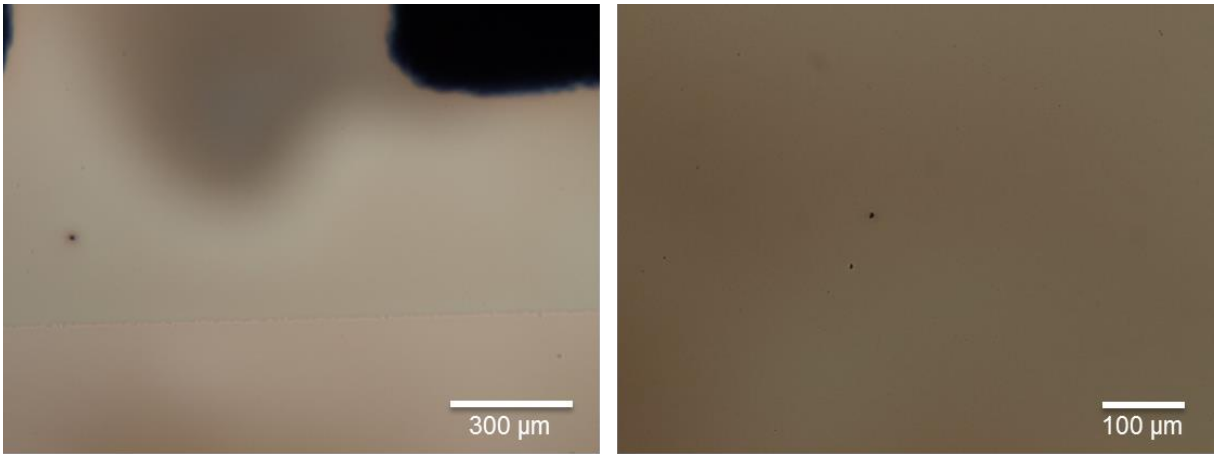

Figure 20: Light microscopy images of the active layer of a substrate from experiment 1 containing PMI-oPh-PMI and PCE-12 1:1 as active layer materials; left: magnification of 100x and right: magnification of 200x.

Images of the cells from experiment 1 were recorded using a light microscope with a magnification of 100x and 200x (see **Figure 20**). The pictures show that a smooth film was processed and that the material was well distributed over the substrate. Only one small crystal is seen in the pictures. In general, the results for this acceptor are quite good, as 1% efficiency was reached already in the first experiment, without further optimization of the assembling process.

4.3.2 PMI-mPh-PMI

Due to the limited solubility of the PMI-mPh-PMI acceptor in CB (12 mg/mL), dichlorobenzene (DCB) was used as solvent with lower mass contents (10 mg/mL) also leading to incomplete dissolution. Nevertheless, in experiment 1 and 2, the not fully dissolved mixture of donor and acceptor was used for assembling the solar cell devices. In experiment 3 the mixture was dissolved in CB (12 mg/mL) and filtrated before coating the active layer. In the 4th experiment, $CHCl_3$ was utilized as solvent, as the PMI-oPh-PMI exhibits a good solubility in this solvent. However, only 5 mg/mL could be dissolved, and the films still contained some crystals (donor/acceptor ratio = 1/0.5).

The IV characteristics of experiment 1, listed in **Table 10**, show that the best PCE (2.01%) was achieved with these substrates. These characteristics were measured before and after an annealing step of 150 °C for 10 min. After the annealing, the V_{OC} decreased drastically, but the FF has a high value with 47%. The PCE decreased by almost 0.30%. The substrate described in experiment 1 had an active layer thickness of 42 nm, which is very low compared to the experiments with the other acceptors.

Table 10: IV characteristics, annealing temperature and active layer thickness of the assembled solar cells with the active layer consisting of PMI-mPh-PMI and PCE-12 1:1 (experiments 1 – 3) or 1:0.5 (experiment 4) with an acceptor concentration of 5, 10 and 12 mg/mL; the parameters of best cell shown in brackets; the values are averaged over 5 cells.

Experiment	V_{OC} [V]	I_{SC} [mA/cm^2]	FF [%]	PCE [%]	T [°C]	Thickness [nm]
1	0.97 (0.99) ± 0.02	3.78 (3.82) ± 0.11	40 (41) ± 1	1.90 (2.01) ± 0.08	-	42
1.1	0.71 (0.73) ± 0.02	4.87 (4.97) ± 0.09	47 (47) ± 1	1.62 (1.71) ± 0.08	150	42
2	0.98 (0.99) ± 0.03	4.05 (4.17) ± 0.07	43 (43) ± 1	1.69 (1.78) ± 0.07	-	-
2.1	0.85 (0.89) ± 0.05	4.05 (4.14) ± 0.07	43 (45) ± 1	1.47 (1.67) ± 0.15	150	-
2.2	0.80 (0.85) ± 0.08	4.13 (4.28) ± 0.11	39 (39) ± 0	1.27 (1.42) ± 0.15	150	-
3	0.90 (0.89) ± 0.01	2.62 (2.88) ± 0.18	38 (37) ± 1	0.90 (0.96) ± 0.06	150	62
4	0.44 (0.83) ± 0.41	1.05 (2.37) ± 1.82	58 (31) ± 38	0.31 (0.61) ± 0.29	150	-

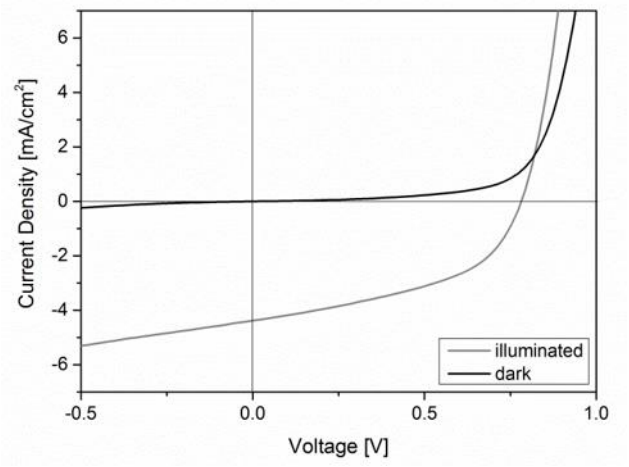

Figure 21: IV characteristics of the solar cell with the highest PCE using the PMI-mPh-PMI acceptor (experiment 1) of the dark measurement (black) and the illuminated measurement (grey), respectively.

In **Figure 21**, the IV curves of the best solar cell of the PMI-mPh-PMI acceptor are shown. The grey line represents the measurement under illumination and the black curve the measurement under dark conditions. In contrast to **Figure 19**, both curves have a similar slope, but it is seen that the black line drops below 0 in the region between -0.5 and -0.75 V.

In experiment 2 the devices were characterized before annealing at 150 °C, after annealing and afterwards after a light soaking of 5 min. Before the annealing, the best cell gave an efficiency of 1.78% and afterwards 1.69%. The V_{OC} decreased and the fill factor was slightly increased. These observations are the same as for experiment 1. After light soaking, the effi-

ciency and the V_{OC} decreased further from 1.67% to 1.42% and 0.85 V to 0.80 V, respectively. The FF decreased throughout the light soaking process. The annealing showed to have a negative effect on the solar cell parameters. This may be a result of the remaining crystals in the film.

The 3rd experiment was carried out with a donor acceptor blend dissolved in CB in a concentration of 12 mg/mL; the mixture was filtered before applying the active layer. The substrates were annealed before applying the HTL and the top electrode. Here, the V_{OC} still has a high value of 0.90 V and the PCE is rather good with 0.96%. The FF dropped below 40% and the I_{SC} is much lower compared to experiment 1 and 2. In **Figure 22**, images of the active layer of the cells in experiment 2 and 3 are shown, recorded using a light microscope in a magnification of 500x. The active layer in the left image shows that multiple, needle-like crystals are present in the device; whereas dissolving the donor and acceptor in CB with consequent filtration leads to a smooth and homogeneous surface without crystallites. As expected, the layer thickness of the substrate shown in the left image could not be determined, due to roughness. The active layer thickness of the right substrate was 62 nm thickness.

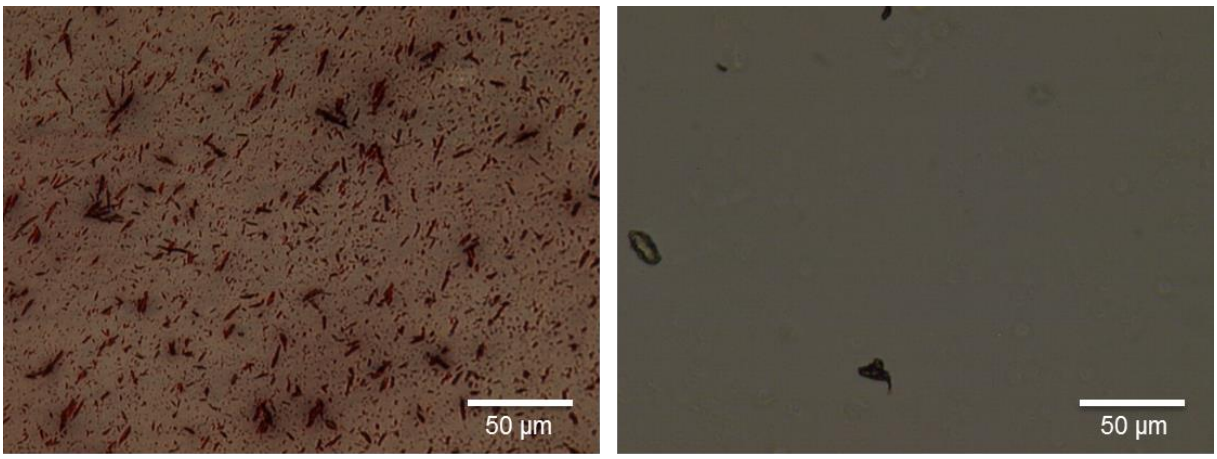

Figure 22: Images of the active layer of a substrate from experiment 2 (left) and 3 (right) containing PMI-mPh-PMI and PCE-12 1:1 as active layer materials; a magnification of 500x was used.

In the last experiment (4), the acceptor was dissolved in $CHCl_3$ with a concentration of 5 mg/mL. Even though the sample seemed to be fully dissolved, small crystals were present in the active layer. Overall, these substrates gave the lowest efficiency of all experiments with PMI-mPh-PMI. The averaged value for the V_{OC} was 0.44 V, the I_{SC} was 1.05 mA/cm^2 and the PCE reached barely 0.31%. Nevertheless, the FF has the highest value with 58%. The best cell in this experiment gave better results, but it was still not comparable to the other experiments. This drastic decrease of all parameters except the FF, could be a result of the low ac-

ceptor concentration in the active layer and the different donor acceptor ratio (1:0.5 instead of 1:1).

4.3.3 PMI-pPh-PMI

The PMI-pPh-PMI showed the lowest solubility of all acceptors in the chosen solvents; it was not possible to dissolve the compound in neither CB, DCB, nor $CHCl_3$. Thus, the donor acceptor blend contained undissolved parts throughout all three experiments.

The 1st experiment was carried out with CB as solvent and an acceptor concentration of 12 mg/mL. As stated above, the acceptor was not dissolved; still the cells were assembled. The substrates were measured before and after annealing at 120 °C. Here, the V_{OC} and FF did not change and the I_{SC} was increasing slightly. Upon annealing, the PCE increased for the best cell from 1.33% to 1.49%. All results are given in **Table 11**.

Table 11: IV characteristics, annealing temperature and active layer thickness of the assembled solar cells with the active layer consisting of PMI-pPh-PMI and PCE-12 1:1 (experiment 1, 2) or 1:0.5 (experiment 3) in an acceptor concentration of 5 and 12 mg/mL; the parameters of best cell shown in brackets; the values are averaged over 5 cells.

Experiment	V_{OC} [V]	I_{SC} [mA/cm^2]	FF [%]	PCE [%]	T [°C]	Thickness [nm]
1	0.85 (0.87) ± 0.02	3.43 (3.71) ± 0.42	41 (41) ± 2	1.18 (1.33) ± 0.14	-	-
1.1	0.85 (0.87) ± 0.01	3.79 (4.11) ± 0.48	41 (42) ± 1	1.31 (1.49) ± 0.17	120	-
2	0.89 (0.89) ± 0.00	3.88 (4.00) ± 0.07	43 (43) ± 0	1.49 (1.53) ± 0.03	-	193
3	0.90 (0.89) ± 0.01	3.11 (3.28) ± 0.16	41 (43) ± 1	1.17 (1.27) ± 0.08	150	-

In the light microscopy images (**Figure 23**), it can be seen that multiple crystals are present throughout the whole substrate. The left image was made in a magnification of 200x and the right with 500x. With the higher magnification one can see that beside the large crystals, small, needle-like structures appeared as well. Due to the heterogeneity, the layer thickness could not be determined for those substrates.

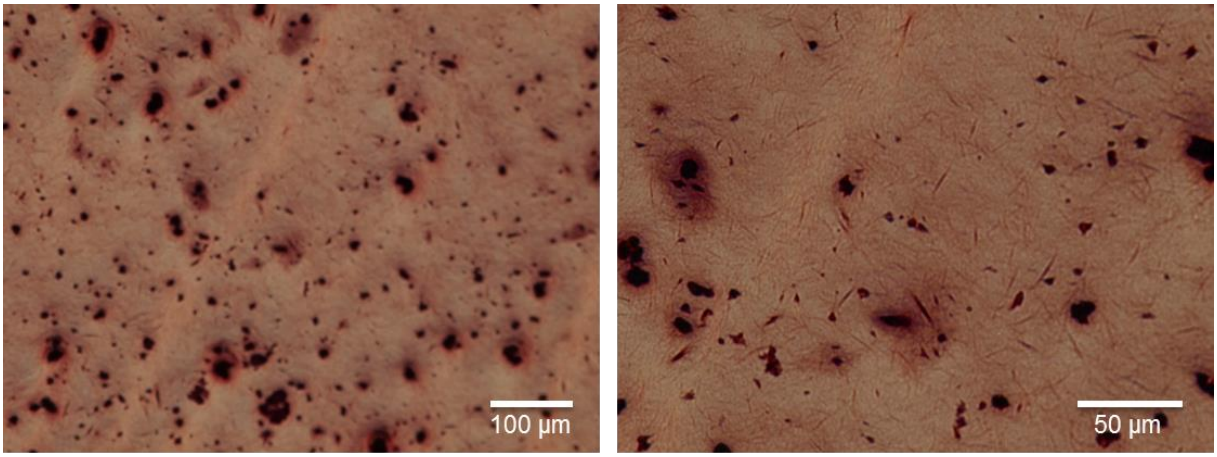

Figure 23: Images of the active layer of a substrate from experiment 1 containing PMI-pPh-PMI and PCE-12 1:1 as active layer materials; left: magnification of 200x and right: magnification of 500x.

In the 2nd experiment, the concentration was again 12 mg/mL and the substrates were not annealed. Comparing the results with experiment 1, the parameters are similar for the V_{OC}, I_{SC} and FF. The PCE was increasing slightly, giving up to 1.53%. This efficiency may be further increased with an annealing step. Only in experiment 2 the active layer thickness could be determined, which is high with 193 nm; in the other experiments the active layer was too rough to achieve a reliable measurement.

In **Figure 24**, the IV characteristics of the best cell from experiment 2 are shown. The red curve indicates the measurement under illumination and the black curve under dark conditions. The results are comparable to the IV curves from the PMI-oPh-PMI containing solar cells.

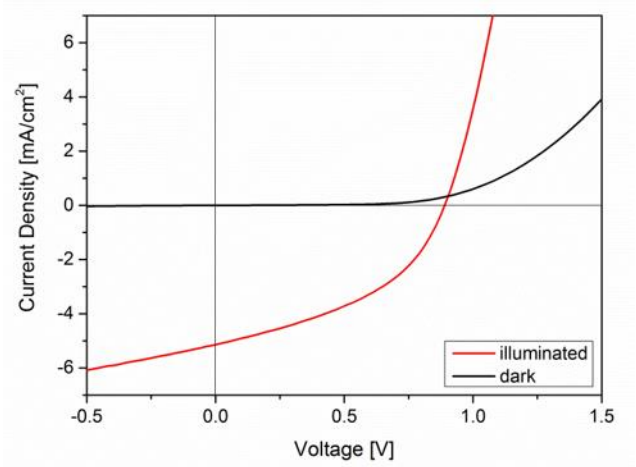

Figure 24: IV characteristics of the best solar cell with the PMI-pPh-PMI acceptor (experiment 2); red line giving the measurement under illumination and black line giving the measurement under dark conditions.

In the last experiment 5 mg/mL were dissolved in $CHCl_3$, which did not work out, even though the concentration of the acceptor was much lower than in the other experiments. The PCE is quite high with 1.17% and 1.27% for the best cell. The values for the I_{SC} and FF are similar to the other experiments; only the efficiency and the V_{OC} deviate slightly. Here, an annealing step at 150 °C was applied.

The results from experiment 3 indicate that the concentration of the acceptor has low impact on the solar cell parameters if the compound is not fully dissolved. For every experiment a saturated solution of the acceptor was used with remaining crystals in the resulting films.

4.3.4 Ph(PMI)$_3$

With $Ph(PMI)_3$ one experiment was carried out. The donor acceptor blend had a concentration of 10 mg/mL, both fully dissolved in $CHCl_3$. Due to the problems in the processing of the active layer with the solvent $CHCl_3$, the layer thickness was for all substrates approximately 150 nm. The best cell gave only a V_{OC} of 0.75 V and a very low I_{SC} of 0.65 mA/cm^2. The FF and PCE reached only 32% and 0.16%, respectively. Compared to all other acceptors, $Ph(PMI)_3$ gave the least satisfying results. This could also be a side effect of the annealing at 150 °C, as the cells were not measured prior to the annealing step.

Table 12: IV characteristics, annealing temperature and active layer thickness of the assembled solar cells with the active layer consisting of $Ph(PMI)_3$ and PCE-12 1:1 with an acceptor concentration of 10 mg/mL; the parameters of best cell shown in brackets; the values are averaged over 5 cells.

Experiment	V_{OC} [V]	I_{SC} [mA/cm^2]	FF [%]	PCE [%]	T [°C]	Thickness [nm]
1	0.72 (0.75) ± 0.02	0.53 (0.65) ± 0.09	32 (32) ± 2	0.12 (0.16) ± 0.02	150	148

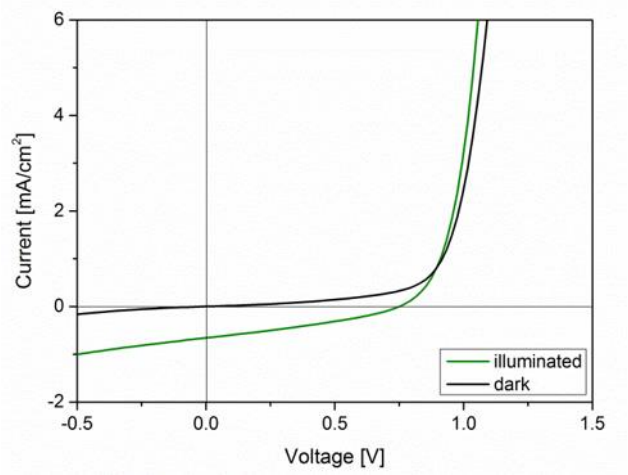

Figure 25: IV characteristics of the best solar cell with the $Ph(PMI)_3$ acceptor (experiment 1); green line giving the measurement under illumination and black line giving the measurement under dark conditions.

The IV curves of the best cell are depicted in **Figure 25**. The green line illustrates the measurement under illumination and the black line under dark conditions. The graph looks similar to **Figure 21**, which shows the IV characteristics of PMI-mPh-PMI; between -0.75 and -0.5 the black line decreases.

4.3.5 Comparison

The performance of the cells containing different acceptors highly depends on the solubility and temperature stability of the compounds. In **Table 13** the IV characteristics, annealing temperature and layer thickness of one solar cell device from each acceptor are listed. For good comparability, the data was chosen when all acceptors were annealed at the same temperature. In general, the best efficiencies were observed in solar cells where the active layer was not smooth but contained crystals. However, due to temporal limitations, the optimization was not possible, which means that the results shown are not representative for each acceptor. With further optimization of the procedure the parameters may be improved.

Nevertheless, solar cells containing PMI-mPh-PMI gave the highest PCE's so far, whereas the trimeric compound exhibited poor performance, giving the lowest PCE. In addition, the FF reached the highest values with PMI-mPh-PMI throughout all experiments. In contrast, the highest V_{OC} was achieved with the donor acceptor blend of PMI-oPh-PMI:PCE-12.

Table 13: IV characteristics, annealing temperature and active layer thickness of the assembled solar cells of all acceptors blended with PCE-12 1:1 (PMI-oPh-PMI, PMI-mPh-PMI and $Ph(PMI)_3$) or 1:0.5 (PMI-pPh-PMI) with an acceptor concentration of 5, 10 or 12 mg/mL; the parameters of best cell shown in brackets; the values are averaged over 5 cells.

Acceptor	V_{OC} [V]	I_{SC} [mA/cm²]	FF [%]	PCE [%]	T [°C]	Thickness [nm]
PMI-oPh-PMI	1.01 (1.04)	2.38 (2.62)	41 (40)	0.98 (1.08)	150	142
PMI-mPh-PMI	0.71 (0.73)	4.87 (4.97)	47 (47)	1.62 (1.71)	150	42
PMI-pPh-PMI	0.90 (0.89)	3.11 (3.28)	41 (43)	1.17 (1.27)	150	-
$Ph(PMI)_3$	0.72 (0.75)	0.53 (0.65)	32 (32)	0.12 (0.16)	150	148

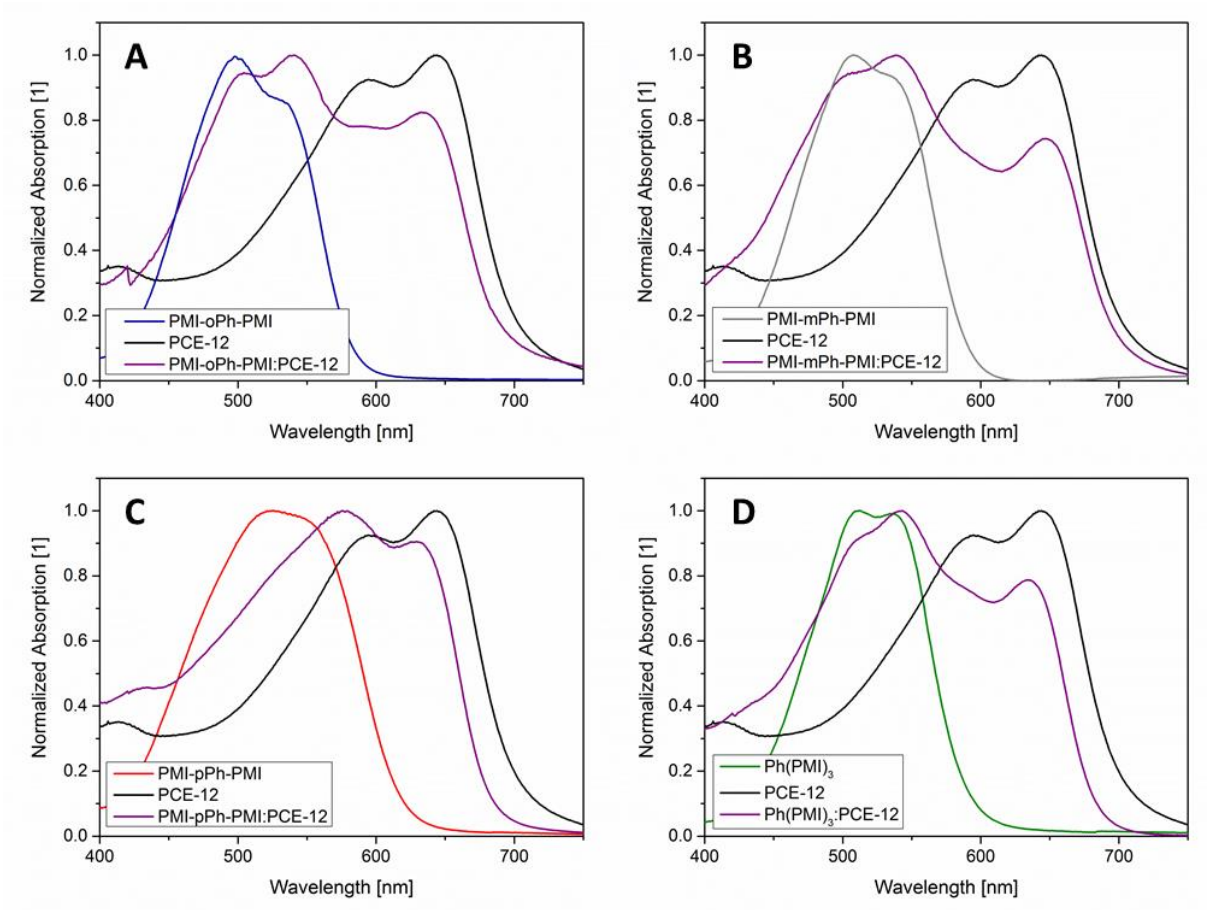

Figure 26: Absorption spectra of each acceptor, the respective blends with the polymer PCE-12 and the plain PCE-12; **A:** absorption spectra of PMI-oPh-PMI (blue), PMI-oPh-PMI:PCE-12 1:1 (violet), PCE-12 (black); **B:** absorption spectra of PMI-mPh-PMI (grey), PMI-mPh-PMI:PCE-12 1:1 (violet), PCE-12 (black); **C:** absorption spectra of PMI-pPh-PMI (red), PMI-pPh-PMI:PCE-12 1:0.5 (violet), PCE-12 (black); **D:** absorption spectra of $Ph(PMI)_3$ (green), $Ph(PMI)_3$:PCE-12 1:1 (violet), PCE-12 (black).

Absorption spectra were recorded for each acceptor, the blend of donor and acceptor, as well as for the donor in films (see **Figure 26**). PCE-12 has the absorption maximum between 500

and 700 nm, whereas all acceptors absorb best between 450 and 600 nm. It is seen that the acceptors in films have similar absorption properties as in solution, with the exception, that the first maximum is the higher, and the second the lower maximum. The only exception is the PMI-oPh-PMI, where the peak at lower wavelengths illustrated the higher maximum in solution as well. As expected, the blends of donor and acceptor gave an absorption between 450 and 700 nm, comprising nearly the whole visible range. In case of PMI-pPh-PMI the blend has a lower absorption between 450 and 600 nm than the other acceptors, as the donor acceptor ratio was only 1:0.5 instead of 1:1, respectively.

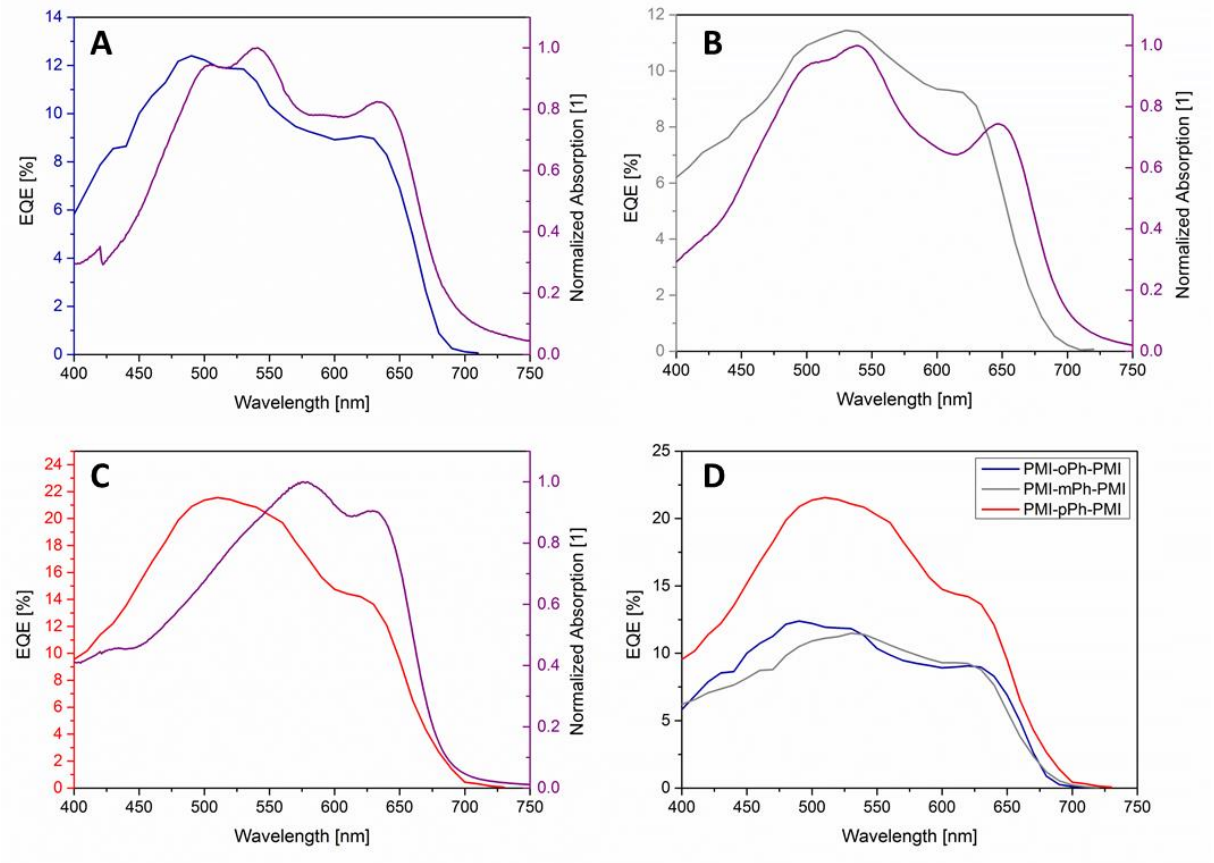

Figure 27: Absorption spectra of the donor:acceptor blends (violet) and EQE spectra of the solar cell devices; **A:** absorption and EQE spectra of PMI-oPh-PMI:PCE-12 1:1; **B:** absorption and EQE spectra of PMI-mPh-PMI:PCE-12 1:1 and 1:0.5, respectively; **C:** absorption and EQE spectra of PMI-pPh-PMI:PCE-12 1:0.5; **D:** EQE spectra of PMI-oPh-PMI (blue), PMI-mPh-PMI (grey) and PMI-pPh-PMI (red).

In **Figure 27**, the external quantum efficiency (EQE) and absorption spectra of the donor acceptor blends of PMI-oPh-PMI, PMI-mPh-PMI and PMI-pPh-PMI are shown. For all illustrations, the EQE spectra look similar to the recorded absorption spectra of the blended films. Comparing the EQE spectra, it is seen that the PMI-pPh-PMI:PCE-12 blend exhibits the highest quantum efficiency. The PMI-oPh-PMI and PMI-mPh-PMI:PCE-12 blends show a similar

behavior. Before and after recording the EQE spectra, the I_{SC} of the cells were measured to see if and how they changed throughout the experiment (see **Table 14**). For all acceptors, the I_{SC} was lower after the EQE measurement. The I_{SC} calculated from the EQE was comparable or lower as well. The results indicate that the solar cell device degraded throughout the experiments.

Table 14: I_{SC} values of solar cells containing the active layer materials PMI-oPh-PMI, PMI-mPh-PMI and PMI-pPh-PMI:PCE-12 blends 1:1 (PMI.oPh-PMI and PMI-mPh-PMI) or 1:0.5 (PMI-pPh-PMI), determined from the EQE spectra and measured before and after the EQE measurement.

Acceptor	**I_{SC} (before EQE)**	**I_{SC} (EQE)**	**I_{SC} (after EQE)**
PMI-oPh-PMI	1.59 mA/cm^2	1.63 mA/cm^2	1.29 mA/cm^2
PMI-mPh-PMI	1.76 mA/cm^2	1.54 mA/cm^2	1.60 mA/cm^2
PMI-pPh-PMI	3.17 mA/cm^2	2.76 mA/cm^2	2.54 mA/cm^2

5. Experimental

5.1 Chemicals and Materials

Reagents and solvents were purchased from Merck, Sigma Aldrich, TCI, abcr, VWR, Roth, Fisher Scientific, Macherey-Nagel and 1-Material. All materials were used without further purification if not otherwise mentioned. Dry solvents and materials used for solar cells were stored under N_2-atmosphere in a glove box.

Table 15: List of chemicals used for the synthesis of compounds **1 – 5** and the assembly of solar cells.

Chemicals	Purity Grade and Description	Supplier
Bromine, Br_2	> 99%, iodometric	Merck
Iodine, I_2	99.99% (trace metal basis), pellets	Sigma Aldrich
Bromo perlyenemonoimide	-	AG Trimmel
1,2-Benzenediboronic acid, bis(pinacol)ester	> 98%	TCI
1,3-Benzenediboronic acid	97%	abcr
1,4-Benzenediboronic acid	not specified	TCI
1,3,5-Phenyltriboronic acid, bis(pinacol)ester	> 98%	TCI
Tetrakis(triphenylphosphine)-Palladium, $Pd(PPh_3)_4$	99.9%	abcr
Aliquat 336	highly viscous liquid	Sigma Aldrich
Potassium carbonate, K_2CO_3	1 M solution	-
Zinc acetate dihydrate	≥ 99.5%	Fluka
2-Methoxyethanol	99.8%, anhydrous	Sigma Aldrich
Ethanolamine	≥ 99%	Sigma Aldrich
PBDB-T/PCE-12	OS0804	One Material
Chlorobenzene (CB)	99.8%, anhydrous	Sigma Aldrich
1,2-Dichlorobenzene (DCB)	99%	Sigma Aldrich
Chloroform (CF)	≥ 99.9%	Sigma Aldrich
Molybdenum(II)oxide	99.98% (trace metal basis)	Sigma Aldrich
Silver, Ag	99.99%, pellets	Kurt J. Lesker Company

5.2 DFT-based Calculations

All synthesized acceptors (compound **2 – 5**) were investigated using DFT-based calculations with the functional B3LYP and the basis set 6-31+G* and 6-31G* in the gas phase, as well as in a solvent environment of chloroform. The calculations in the solvent were performed using the default SCRF method, namely Polarizable Continuum Model (PCM).

5.2.1 Used Software

- Chem3D Version 15.1
  - For pre-optimization of the structures
- Gaussian 09
  - Input: gjf. file with all important information
  - For the geometrical optimization, calculation of energies, eigenvalues, frequencies, etc.
  - Gaussian 09, Revision D.01, M. J. Frisch, G. W. Trucks, H. B. Schlegel, G. E. Scuseria, M. A. Robb, J. R. Cheeseman, G. Scalmani, V. Barone, B. Mennucci, G. A. Petersson, H. Nakatsuji, M. Caricato, X. Li, H. P. Hratchian, A. F. Izmaylov, J. Bloino, G. Zheng, J. L. Sonnenberg, M. Hada, M. Ehara, K. Toyota, R. Fukuda, J. Hasegawa, M. Ishida, T. Nakajima, Y. Honda, O. Kitao, H. Nakai, T. Vreven, J. A. Montgomery, Jr., J. E. Peralta, F. Ogliaro, M. Bearpark, J. J. Heyd, E. Brothers, K. N. Kudin, V. N. Staroverov, T. Keith, R. Kobayashi, J. Normand, K. Raghavachari, A. Rendell, J. C. Burant, S. S. Iyengar, J. Tomasi, M. Cossi, N. Rega, J. M. Millam, M. Klene, J. E. Knox, J. B. Cross, V. Bakken, C. Adamo, J. Jaramillo, R. Gomperts, R. E. Stratmann, O. Yazyev, A. J. Austin, R. Cammi, C. Pomelli, J. W. Ochterski, R. L. Martin, K. Morokuma, V. G. Zakrzewski, G. A. Voth, P. Salvador, J. J. Dannenberg, S. Dapprich, A. D. Daniels, O. Farkas, J. B. Foresman, J. V. Ortiz, J. Cioslowski, and D. J. Fox, Gaussian, Inc., Wallingford CT, 2013.
- molden 5.7 (2017)
  - For the generation of the Z-matrix and the visualization of the vibrations
- Avogadro
  - For visualization of the HOMO-LUMO levels
- VESTA
  - For visualization of the structure

5.3 Synthesis

5.3.1 General Information

Some chemical reactions were performed under nitrogen atmosphere. Therefore, a balloon filled with nitrogen gas was used to degas the solvents and reaction mixtures. During the reaction, a constant stream of nitrogen was kept. If the reaction was performed under completely inert conditions, the glass apparatus was dried by heating with a heat gun under oil pump vacuum, then cooled to room temperature and flushed with nitrogen up to three times prior to the addition of solvent or reagents. The solvents and reaction mixture were all degassed using nitrogen.

5.3.2 Analytical Methods

5.3.2.1 Thin Layer Chromatography (TLC)

All reactions were monitored by thin layer chromatography on silica gel plates (HP-TLC, aluminum sheets, Silica gel 60 F_{254} purchased from Merck Millipore). As all products were visible on the TLC, no further staining was carried out. Elution solvents and R_f-values are stated for each compound.

5.3.2.2 Flash Chromatography

The flash chromatography was performed on silica gel 60 (particle size 0.06 – 0.2 mm and 0.04 – 0.063 mm) from Macherey-Nagel at elevated pressure. If not mentioned differently, the product was dissolved and adsorbed on silica gel before applying it onto the column.

5.3.2.3 Nuclear Magnetic Resonance Spectroscopy (NMR)

The nuclear magnetic resonance spectra were recorded on a Bruker Advance III spectrometer (300 MHz) with auto sampler and on an Inova 500 (500 MHz). The measurement on the 'Varian Inova 500' from Oxford Instruments were carried out by Petra Kaschnitz. Coupling constants (J) are reported as absolute values in Hertz (Hz) and chemical shifts are quoted in parts per million (ppm). To confirm and identify a structure additional NMR experiments (HH-COSY, HSQC, HMBC, APT) were recorded.

5.3.2.4 Mass Spectrometry (MS)

The mass spectra were recorded on the 'Micromass MALDI micro MX' mass spectrometer from Waters. The matrix was Dithranol or *trans*-2-[3-(4-*tert*-Butylphenyl)-2-methyl-2-propenylidene]malononitrile (DCTB) in a concentration of 10 mg/mL in THF; the sample had a concentration of 1 mg/mL in DCM in a mixing ratio matrix/sample = 7/2. The reference material used was polyethylene glycol (PEG). The MS measurements were performed by Karin Bartl and the data analysis was done with the MassLynx V4.1 software.

5.3.2.5 Fluorescence Spectroscopy

For the fluorescence spectroscopy, 3 samples in $CHCl_3$. were prepared with a maximum absorption smaller than or equal to 0.1. To make sure the absorbance is not exceeding 0.1, a UV/VIS spectrum was recorded of each sample immediately before the fluorescence measurement. The spectra were recorded on a UV-Visible Spectrophotometer 'Cary 50 Conc' from Varian with the following settings:

Table 16: Settings for the absorption measurement in $CHCl_3$ before the Fluorescence measurement.

Start Wavelength [nm]	800
End Wavelength [nm]	350
Slit Width [nm]	1.0
Scan Speed [nm/s]	70

Fluorescence spectra were recorded on the 'FluoroLog 3' spectrofluorometer from Horiba Scientific Jobin Yvon adjusted with the 'R2658' photomultiplier from Hamamatsu. A summary of the used settings are given in **Table 17**. The reference material used for these measurements was the 'Fluoreszenzorange' in CF purchased from Kremer Pigmente GmbH & Co.KG.

Table 17: Settings for the fluorescence measurement in $CHCl_3$.

Start Wavelength [nm]	500
End Wavelength [nm]	800
Slit Width [nm]	1.0
Excitation Wavelength [nm]	485

5.3.2.6 UV/VIS Spectroscopy and Optical Band Gap Determination in Solution

UV/VIS spectra in CF were recorded with the UV Spectrophotometer 'UV-1800' from Shimadzu. All products were measured 3x. In each vial, about 1 mg was weighed in and dissolved in 10 mL CF. From this solution, 1 mL was taken and diluted with 9 mL CF. Thereof, 2 mL were taken and diluted with 2 mL CF. According to this, 2 more solutions were made, resulting in a total of 5 solutions with concentrations between 150 and 1.25 mg/L. All samples were measured with the following settings:

Table 18: Settings for the absorption measurement in $CHCl_3$.

Start Wavelength [nm]	800
End Wavelength [nm]	350
Slit Width [nm]	1.0
Scan Speed	350 nm/min
Data Interval [nm]	1

With the accurate concentration and the absorbance maxima, the extinction coefficient was determined from each material. In addition, the band gap of each material was determined graphically from the absorption spectra.

5.3.2.7 Thermogravimetric Analysis (TGA)

The TGA was done on the 'STA 449 C' from NETSCH. The samples were measured in an aluminum pan with helium as protective gas. The flow rate was 50 mL/min and the heating rate 10 K/min. The samples were measured in a temperature range of 20 – 550 °C. The measurements were performed by Josefine Hobisch.

5.3.2.8 Differential Scanning Calorimetry (DSC)

The DSC was carried out using a 'DSC 8500' from Perkin Elmer. The start temperature was 30 °C and the samples were heated with a heating/cooling rate of 20 – 30 °C/min until 400 – 440 °C were reached. Overall, three cycles were measured. The measurements were performed by Josefine Hobisch.

5.3.3 Experimental Procedures and Analytical Data

Compound **1** was synthesized according to Nolde, F.; et al. (2006).[74] Compounds **2 – 5** were synthesized according to Hu, Y.; et al. (2017).[65] An overview of all reactions is shown in **Scheme 4** below.

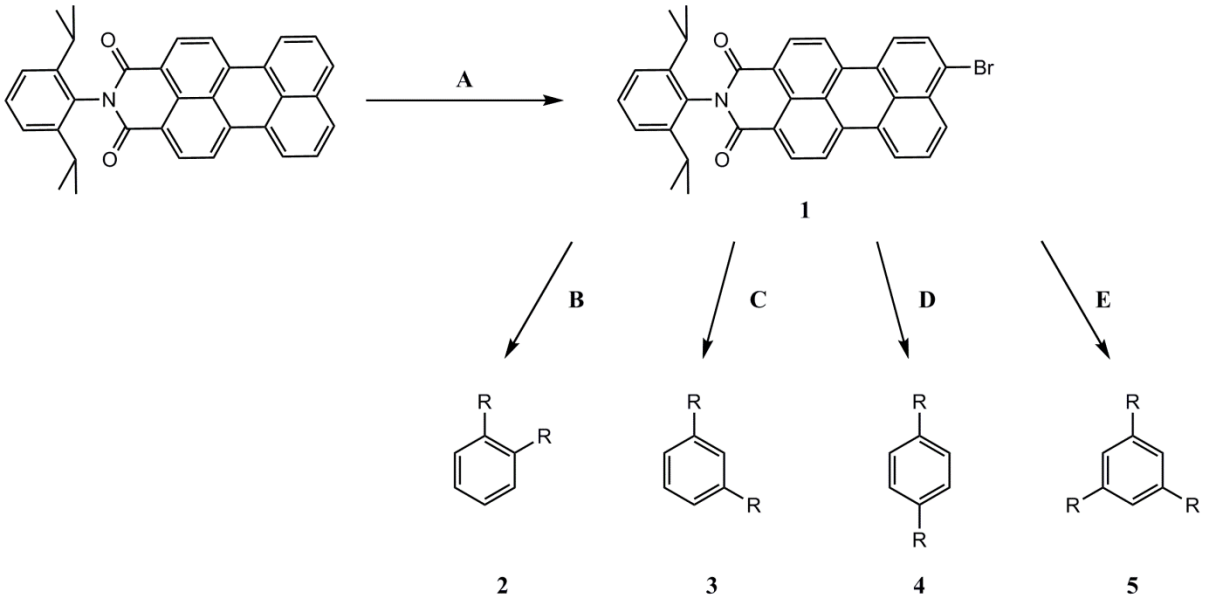

Scheme 4: Overview of all synthetic procedures presented in this work; R = PMI; **A**: 4 eq. Br_2, 0.4 eq. I_2, AcOH, RT; **B**: 0.5 eq. 1,2-Benzenediboronic acid, bis(pinacol)ester, 5 mol% $Pd(PPh_3)_4$, K_2CO_3 (1M), Aliquat 336, toluene, 100 °C, reflux; **C**: 0.5 eq. 1,3-Benzenediboronic acid, 5 mol% $Pd(PPh_3)_4$, K_2CO_3 (1M), Aliquat 336, toluene, 100 °C, reflux; **D**: 0.5 eq. 1,4-Benzenediboronic acid, 5 mol% $Pd(PPh_3)_4$, K_2CO_3 (1M), Aliquat 336, toluene, 100 °C, reflux; **E**: 0.33 eq. 1,3,5-Phenyltriboronic acid, bis(pinacol)ester, 5 mol% $Pd(PPh_3)_4$, K_2CO_3 (1M), Aliquat 336, toluene, 100 °C, reflux.

5.3.3.1 *8-bromo-2-(2,6-diisopropylphenyl)-1*H*-benzol[10,5]anthra[2,1,9*-def*]-isoquino-line-1,3(2*H*)-dione* (**1**)

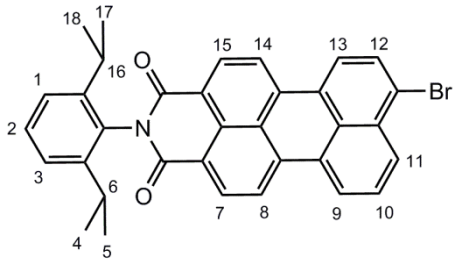

In a 100 mL one-necked round bottom flask ~950 mg (1.97 mmol, 1 eq.) PMI was suspended in 40 mL AcOH. After stirring for 30 min, about 405 µL (7.90 mmol, 4 eq.) bromine and 3 pellets of iodine were added. After 2 h, the mixture turned from bright red to dark red and

another ~300 µL bromine were added. ~17 h later the TLC indicated full conversion and N_2 was bubbled through the mixture for 10 min to remove the remaining bromine. Then, 40 mL MeOH were added and the mixture was stirred for 30 min – 1 h. The mixture was poured into deionized H_2O and the product was collected by filtration followed by drying.

Yield: 1.115 g (1.99 mmol, >99%), dark red powder, $C_{34}H_{26}BrNO_2$ [560.49 g/mol]
R_f = 0.23 (toluene/acetone = 99/1)

^{1}H-NMR (300 MHz; $CDCl_3$) δ = 8.63 – 8.69 (m, 2H, H-7, 15), 8.44 – 8.51 (m, 2H, H-8, 14), 8.42 (d, $^3J_{HH}$ = 8.1 Hz, 1H, H-12), 8.32 (d, $^3J_{HH}$ = 8.4 Hz, 1H, H-13), 8.25 (d, $^3J_{HH}$ = 8.2 Hz, 1H, H-9), 7.91 (d, $^3J_{HH}$ = 8.1 Hz, 1H, H-11), 7.73 (dd, $^3J_{HH}$ = 7.9 and 8.1 Hz, 1H, H-10), 7.49 (t, $^3J_{HH}$ = 7.8 Hz, 1H, H-2), 7.34 (d, $^3J_{HH}$ = 7.8 Hz, 2H, H-1, 3), 2.82 – 2.72 (m, 2H, H-6, 16), 1.19 (d, $^3J_{HH}$ = 6.9 Hz, 12H, H-4, 5, 17, 18)

5.3.3.2 *8,8'-(1,2-phenylene)bis(2-(2,6-diisopropylphenyl)-1*H*-benzo[10,5]anthra-[2,1,9-*def*]isoquinoline-1,3(2*H*)-dione)* (**2**)

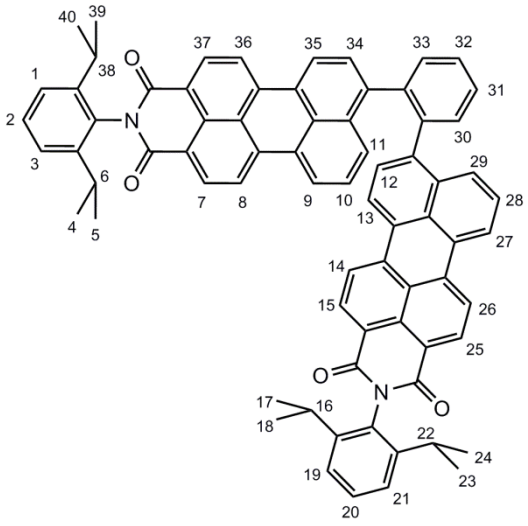

The reaction was performed under inert conditions. In a 250 mL two-necked round bottom flask 500 mg (0.89 mmol, 2 eq.) of compound **1** were suspended in 70 mL toluene which was degassed by a stream of nitrogen. Then, 148.5 mg (0.45 mmol, 1 eq.) 1,2-benzenediboronic acid, bis(pinacol)ester and 7 mL 1 M K_2CO_3 solution were added and, the mixture was de-gassed with nitrogen. One drop of Aliquat 336 and 5 spatula tips of $Pd(PPh_3)_4$ were added and the reaction mixture was heated to 100 °C. After 68 h the TLC indicated full conversion and

the reaction mixture was cooled down to room temperature. It was then washed with deionized water (3 × 30 mL). The combined aqueous layers were then extracted with toluene (1 × 30 mL). The combined organic layers were dried over Na_2SO_4. After filtration, the remaining Na_2SO_4 was washed with toluene and the solvent of the organic phases was removed under reduced pressure. The product was purified via flash chromatography (564 g silica gel, CH_2Cl_2/CH = 1/1 – 9/1, then DCM, fraction size: 65 mL and 95 mL). As the product was not fully separated from the side products in the column, further purification steps were necessary, concluding 2 small flash chromatography in a glass frit (DCM/CH = 4/1 and DCM). From these steps about 147 mg of the product, still with some impurities, was obtained. After recrystallization (DCM/MeOH) 139 mg pure product was obtained.

Yield: 139 mg (0.13 mmol, 30%), glimmering dark red powder, $C_{74}H_{56}N_2O_4$ [1037.27 g/mol]
R_f = 0.38 (DCM)

^{1}H-NMR (500 MHz; $CDCl_3$) δ = 8.46 (d, $^3J_{HH}$ = 7.8 Hz, 1H), 8.35 (d, $^3J_{HH}$ = 7.2 Hz, 2H), 8.30 (d, $^3J_{HH}$ = 7.8 Hz, 1H), 8.23 (d, $^3J_{HH}$ = 7.6 Hz, 1H), 8.20 (d, $^3J_{HH}$ = 7.9 Hz, 1H), 8.06 – 8.10 (m, 1H), 7.99 – 8.06 (m, 2H), 7.99 – 7.92 (m, 2H), 7.90 (d, $^3J_{HH}$ = 8.4 Hz, 1H), 7.84 – 7.74 (m, 2H), 7.74 – 7.67 (m, 2H), 7.67 – 7.61 (m, 2H), 7.59 – 7.53 (m, 1H), 7.49 – 7.41 (m, 3H), 7.37 – 7.32 (m, 1H), 7.30 (d, $^3J_{HH}$ = 7.8 Hz, 4H, H-1, 3, 19, 21), 7.18 (d, $^3J_{HH}$ = 7.7 Hz, 1H), 2.71 – 2.59 (m, 4H, H-6, 16, 22, 38), 1.19 – 1.06 (m, 24H, H-4, 5, 17, 18, 23, 24, 39, 40)

MS (MALDI-TOF) *m/z*: 1037.4475 (calculated for $C_{74}H_{56}N_2O_4$, $[MH]^+$ 1037.4391)

5.3.3.3 *8,8'-(1,3-phenylene)bis(2-(2,6-diisopropylphenyl)-1*H*-benzo[10,5]anthra-[2,1,9-*def*]isoquinoline-1,3(2*H*)-dione)* (**3**)

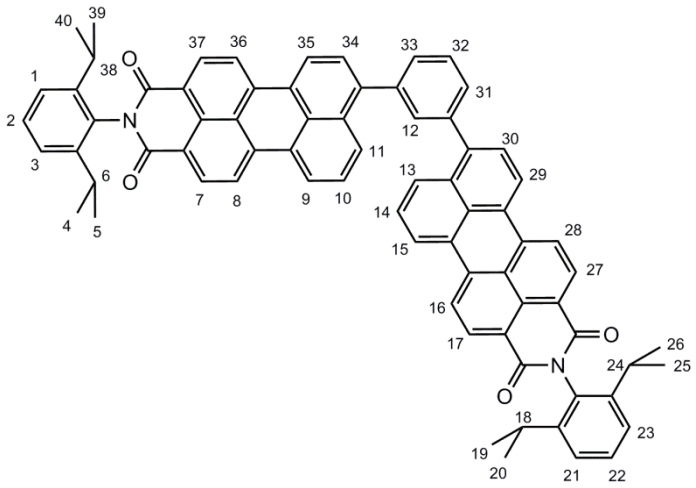

In a 250 mL two-necked round bottom flask 1.103 g (1,97 mmol, 2 eq.) of compound 1 were suspended in 100 mL toluene. To remove the oxygen from the solvent, the mixture was degassed with nitrogen. 166 mg (1.00 mmol, 1 eq.) 1,3-Benzenediboronic acid and 14 mL 1M K_2CO_3 solution were added and the mixture was degassed with nitrogen. 116.1 mg (0.1 mmol, 5 mol%) $Pd(PPh_3)_4$ and 2-3 drops Aliquat 336 were added and the mixture was heated up to 100 °C and stirred at this temperature for 45 h. Then the reaction mixture was cooled down and 29 mg (0.025 mmol, 1.3 mol%) $Pd(PPh_3)_4$ were added. The reaction mixture was then heated up again and after 4 h more, 42.1 mg (0.25 mmol, 0.13 eq) 1,3-Benzenediboronic acid were added. According to TLC, after another 17 h 30 min, there was no full conversion. Still the reaction mixture was cooled down to room temperature. The reaction mixture was washed with deionized H_2O (3 × 35 mL) and brine (2 × 45 mL). The combined aqueous layer were extracted with toluene (2 × 50 mL). The combined organic layers were dried over Na_2SO_4. After filtration, the remaining Na_2SO_4 was washed with toluene and dichloromethane. The solvent was removed under reduced pressure. The product was purified via flash chromatography (321 g silica gel, toluene/acetone = 99/1, fraction size: 65 mL). As the product was not fully separated from the side products in the column, recrystallization was used for further purification (DCM/toluene and MeOH). After 3 recrystallization steps, 117 mg pure product was obtained.

Yield: 117 mg (0.11 mmol, 11%), red powder, $C_{74}H_{56}N_2O_4$ [1037.27 g/mol]

R_f = 0.12 (DCM)

T_G: 311.10 °C

^{1}H-NMR (500 MHz; $CDCl_3$) δ = 8.72 – 8.66 (m, 4H, H-7, 17, 27, 37), 8.58 (d, $^{3}J_{HH}$ = 7.9 Hz, 2H, H-29, 35), 8.56 (d, $^{3}J_{HH}$ = 7.5 Hz, 2H, H-9, 15), 8.54 – 8.49 (m, 4H, H-8, 16, 28, 36), 8.18 (d, $^{3}J_{HH}$ = 8.4 Hz, 2H, H-11, 13), 7.77 – 7.65 (m, 8H, H-10, 12, 14, 30, 31, 32, 33, 34), 7.49 (t, $^{3}J_{HH}$ = 7.8 Hz, 2H, H-2, 22), 7.35 (d, $^{3}J_{HH}$ = 7.8 Hz, 4H, H-1, 3, 21, 23), 2.82 – 2.73 (m, 4H, H-6, 18, 24, 38), 1.19 (d, $^{3}J_{HH}$ = 6.8 Hz, 24H, H-4, 5, 19, 20, 25, 26, 39, 40)

MS (MALDI-TOF) *m/z*: 1037.4264 (calculated for $C_{74}H_{56}N_2O_4$, $[MH]^+$ 1037.4302)

*5.3.3.4 8,8'-(1,4-phenylene)bis(2-(2,6-diisopropylphenyl)-1*H*-benzo[10,5]anthra-[2,1,9-*def*]isoquinoline-1,3(2*H*)-dione)* (**4**)

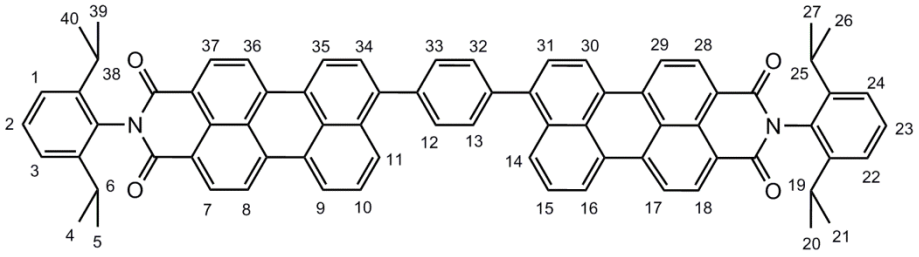

Compound 4 was synthesized by Matiss Reinfelds according to Hu, Y.; et al. (2017).[65], similar to compounds 2, 3 and 5.

MS (MALDI-TOF) *m/z*: 1037.4325 (calculated for $C_{74}H_{56}N_2O_4$, $[MH]^+$ 1037.4319)

5.3.3.5 *8,8',8''-(benzene-1,3,5-triyl)tris(2-(2,6-diisopropylphenyl)-1*H*-benzo[10,5]-anthra[2,1,9-*def*]isoquinoline-1,3(2*H*)-dione)* (**5**)

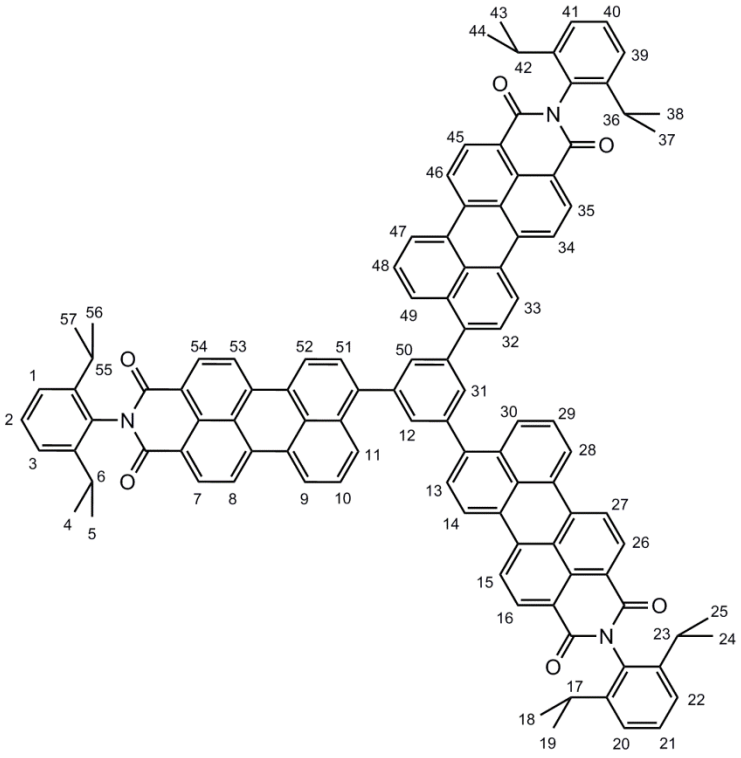

In a 250 mL round bottom flask 750 mg (1.34 mmol, 3 eq.) compound 1 was suspended in 70 mL toluene. To remove the oxygen from the solvent, the mixture was degassed with nitrogen for 35 min. Then 202 mg (0.44 mmol, 1 eq.) 1,3,5-phenyltriboronic acid, tris(pinacol)ester and 7 mL 1 M K_2CO_3 solution were added and again, the mixture was degassed with nitrogen for 45 min. One drop of Aliquat 336 and 5 spatula tips of $Pd(PPh_3)_4$ were added and the reaction mixture was heated up to 100 °C. After 23 h 35 min, the TLC indicated nearly full conversion and the reaction mixture was cooled down to room temperature, before it was washed with deionized water (3 × 30 mL). The combined aqueous layers were extracted with toluene (2 × 30 mL). The combined organic layers were then washed with brine (1 × 30 mL) and dried over Na_2SO_4. After filtration, the remaining Na_2SO_4 was washed with toluene and the solvent was removed under reduced pressure. A flash chromatography was made (DCM, fraction size: 95 – 500 mL) for purification. The product remained on the column and the silica gel was then extracted using first DCM and then $CHCl_3$. The flash chromatography was repeated with silica gel in a glass frit, with DCM as solvent. 55 mg of the product was obtained with some impurities.

Yield: 55 mg (0.04 mmol, 8%), glimmering dark red/violet powder, $C_{108}H_{81}N_3O_6$ [1516.85 g/mol]
R_f = 0.35 (DCM)

^{1}H-NMR (500 MHz; $CDCl_3$) δ = 8.67 (dd, $^3J_{HH}$ = 5.10 Hz, 6H, H-7, 16, 26, 35, 45, 54), 8.59 (d, $^3J_{HH}$ = 8.0 Hz, 3H, H-14, 33, 52), 8.53 (d, $^3J_{HH}$ = 7.7 Hz, 3H, H-9, 28, 47), 8.52 – 8.46 (m, 6H, H-8, 15, 27, 34, 46, 53), 8.32 (d, $^3J_{HH}$ = 8.5 Hz, 3H, H-11, 30, 49), 7.92 (s, 3H, H-12, 31, 50), 7.85 (d, $^3J_{HH}$ = 7.8 Hz, 3H, H-13, 32, 51), 7.72, (t, $^3J_{HH}$ = 8.0 Hz, 3H, H-10, 29, 48), 7.48 (t, $^3J_{HH}$ = 7.7 Hz, 3H, H-2, 21, 40), 7.34, (d, $^3J_{HH}$ = 7.8 Hz, 6H, H-1, 3, 20, 22, 39, 41), 2.82 – 2.74 (m, 6H, H-6, 17, 23, 36, 42, 55), 1.19 (d, $^3J_{HH}$ = 6.8 Hz, 39H, H-4, 5, 18, 19, 24, 25, 37, 38, 43, 44, 56, 57)

MS (MALDI-TOF) *m/z*: 1516.4862 (calculated for $C_{108}H_{81}N_3O_6$, $[MH]^+$ 1516.4858)

5.4 Organic Solar Cells

5.4.1 General Procedure

All solar cells were assembled in an inverted architecture with a bulk heterojunction device design. Each device consists of a top electrode, the active layer and the bottom electrode on a glass substrate with interlayers between both electrodes and the active layer. All devices were assembled according to the following procedure.

5.4.1.1 Cleaning and Activation of the Substrates

ITO-coated glass substrates (15 x 15 x 1.1 mm) with a sheet resistance of 15 Ω were used purchased from the Luminescence Technology Corporation. The substrates were cleaned with water and acetone before ultrasonic treatment in a bath of 2-propanol at 40 °C for 30 min. The ultrasonic bath used was the 'ultrasonic cleaner' from VWR. After the ultrasonic treatment, the substrates were dried with compressed air (N_2) followed by activation of the surface via plasma etching. The etching was carried out at a constant oxygen gas flow for 3 min in the 'Femto' etcher from Diener Electronics. The activated substrates were then transferred into the N_2-filled glove box 'LabMaster dp' from MBraun.

5.4.1.2 ZnO-Interlayer

The ZnO-interlayer was applied using a sol-gel procedure. A ZnO-precursor solution was prepared with a composition of 500 mg zinc acetate dihydrate, 5 mL 2-methoxyethanol and 150 µL ethanolamine. These were mixed and stirred outside the glove box for 18 h. The precursor solution was then again transferred into the N_2-filled glove box, where it continued stirring.

The deposition of the ZnO-interlayer was done via spin coating 35 µL of the precursor solution with 4000 rpm and 2000 rpm/s acceleration for 30 s, onto the ITO-coated glass substrates to obtain a layer thickness of 20 – 30 nm. A spin coater from Laurell Technologies was used ('Model WS-650MZ-23NPPB). After spin coating, the substrates were annealed at 150 °C for 10 min outside the glove box, before they were transferred in again.

5.4.1.3 Active Layer

The acceptor was diluted with CB, DCB or CF and dissolved for at least 1 h at 50 °C. The polymer PCE-12 was added and the mixture was left overnight to stir at 50 °C. The concentration was varied from 5 to 12 mg/mL (depending on the solubility of the acceptor). If not otherwise mentioned, the ratio between donor and acceptor was 1:1 and the resulting solution was deposited via spin coating with different parameters to obtain a layer thickness of 100 nm. For all substrates a drying step was included in the spin coating process with 4000 rpm, 4000 acc. for 5 s. The deposition of the active layer was, if not otherwise mentioned, concluded with an annealing step of 10 min at varying temperatures.

5.4.1.4 MoO_3-Interlayer and Ag Electrode

The MoO_3-interlayer (10 nm) and the Ag-electrode (100 nm) were deposited on the substrate via thermal evaporation. Therefore, a shadow mask was used giving an active electrode area of 0.09 cm^2. The evaporation was done under vacuum conditions with at least 1×10^{-5} mbar.

5.4.2 Characterization

5.4.2.1 UV/VIS-Spectroscopy in Films

To show the absorption behavior of the synthesized acceptors and the polymer PCE-12, absorption spectra were measured in thin films on glass substrates. Therefore, the acceptor and the polymer were coated on glass substrates via spin coating of the respective solutions (5 – 12 mg/mL) in CB, DCB or CF. Additionally, a 1:1 or 1:0.5 blend of each acceptor and the polymer were made and also deposited on glass substrates via spin coating of the respective solutions (12 mg/mL) in CB, DCB or CF. The preparation was done in a N_2-filled glove box. The spectra were recorded on the UV-VIS Spectrometer 'Lambda 35' from Perkin Elmer with the following settings:

Table 19: Settings for the absorption measurement of the acceptor, the polymer PCE-12 and the mixture of both PCE-12 with each acceptor in films.

Start Wavelength [nm]	800
End Wavelength [nm]	400
Slit Width [nm]	1.0
Scan Speed [nm/min]	240
Data Interval [nm]	1

5.4.2.2 I-V Characteristics

IV curves were monitored under illumination for each solar cell and under dark conditions for the best cell of each substrate, with the settings shown in **Table 20**. The measurement was made using a Keithley 2400 SourceMeter and a custom-made Lab-View software. The light source used was a Dedolight DEB400D lamp, which was set to an intensity of 100 mW/cm^2, providing a spectrum similar to AM 1.5 G. The solar cells have an active area of 0.09 cm^2. If not otherwise mentioned, a shadow mask was used for the measurements, which enclose the active area to 0.070225 cm^2. From the IV curves characteristic parameters such as the V_{OC}, I_{SC}, FF and PCE were determined and averaged over the best five solar cells.

Table 20: Settings for the IV-Measurement for all solar cell devices.

Start [mV]	1500
End [mV]	-500
Compliance [mA]	100
Number of Points	100
Overwrite Max Compliance [mA]	500
Delay [ms]	100
Step Widths [V]	-0.02

5.4.2.3 Layer Thickness and Roughness

In order to determine the thickness and roughness of the active layer, a small scratch was applied to the samples with a blade. Following this, the thickness and roughness was determined on 5 different positions using the contact profilometer 'DektakXT' from Bruker.

5.4.2.4 External Quantum Efficiency (EQE)

EQE measurements were carried out for one solar cell of each acceptor, prepared as described in Chapter 5.4.1. The IPCE (incident photon-to-current efficiency) measuring system consisted of a MuLTImode 4-AT monochromator (Amko) equipped with a xenon lamp (LPS 210-U, Amko) and a Keithley 2400 SourceMeter. For the measurement, the solar cell device was sealed under nitrogen in a custom made measuring box. After calibration with a photo diode (1.2 mm²), the EQE spectra of the solar cells (9 mm²) were monitored in the range of 380 – 900 nm.

5.4.2.5 Light Microscopy

Images of the active layer from the solar cell devices were made using the light microscope ‘BX60’ from Olymp with a camera (Olymp) attached. The images have a magnification of 50x, 100x, 200x, 500x and 1000x.

6. Summary and Conclusion

All desired acceptors were successfully synthesized and exhibit colors from light to dark red. The obtained yield was between 8% and 30%, which is much lower than those achieved in the literature. However, many side products occurred and not all fractions were purified yet. With further optimization of the reaction conditions the yield could be improved. This includes not only the used equivalents of the educts, but also the choice of catalyst, base and solvent. During the research it was found that the molecules have a limited solubility. This issue may be avoided by introducing alkyl-groups as side chains on the respective linker, which could hinder the π-stacking, thus increasing the solubility.

The synthesized molecules exhibit the highest absorption between wavelengths of 450 nm and 600 nm and two peaks can be observed in the visible region. Their maxima lie between 490 nm and 530 nm. The absorption maxima are slightly shifted to higher wavelengths in the following order: PMI-oPh-PMI < PMI-mPh-PMI = $Ph(PMI)_3$ < PMI-pPh-PMI. The molar absorption coefficient increases in the same order with PMI-oPh-PMI the lowest and PMI-pPh-PMI the highest. However, the $Ph(PMI)_3$ exhibits a higher absorption coefficient than PMI-mPh-PMI, most likely due to the additional PMI unit. Compared to the simpler structures of PMI, PMI-Br and Ph(PMI), the maxima of PMI and PMI-Br occur at lower wavelengths (λ_{max} = 487 nm) and for Ph(PMI) it is in the same range as the synthesized acceptors. They all show a lower absorption coefficient than the synthesized compounds. All phenylene-linked perylene monoimides reach a molar absorption coefficient of at least 77 000 L mol^{-1} cm^{-1}, whereas the PMI, PMI-Br and the Ph(PMI) achieve only 34 000 – 35 000 L mol^{-1} cm^{-1} (see **Figure 28**).

The optical band gaps of all investigated compounds are comparable. This was confirmed by DFT computations. However, all calculated band gaps were higher than those determined from the experimental data. According to the computations, the HOMO-LUMO levels decrease in the order PMI > PMI-oPh-PMI > PMI-mPh-PMI > PMI-pPh-PMI > PMI-Br > $Ph(PMI)_3$. In general, the computations with the smaller basis set are less accurate than with the larger basis set in the gas phase. When the computations were carried out in a solvent environment, the smaller basis set achieved similar values as the larger one in the gas phase.

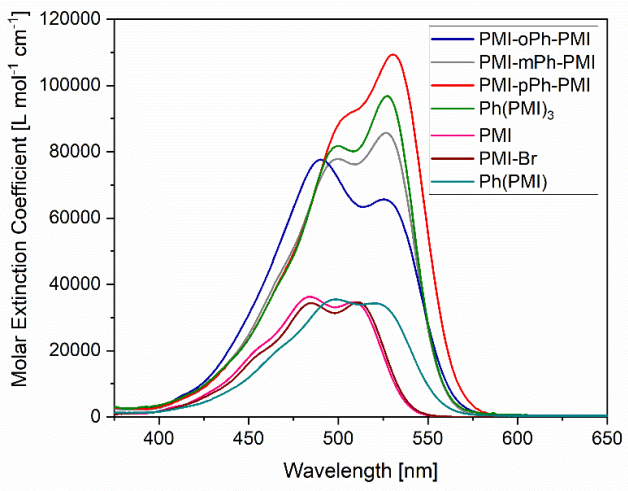

Figure 28: Absorption spectra of all investigated compounds dissolved in chloroform; blue: PMI-oPh-PMI, grey: PMI-mPh-PMI, red: PMI-pPh-PMI, green: $Ph(PMI)_3$, pink: PMI, brown: PMI-Br, cyan: Ph(PMI).

The fluorescence spectra show similar behavior for each compound, giving a Stokes-shift of about 30 – 40 nm for all compounds. The calculated quantum yield was comparable for all acceptors, giving the highest value of 81% for $Ph(PMI)_3$ and the lowest for PMI-oPh-PMI (77%). Thermal analysis showed that the acceptors have a high melting point and they decompose above 400 °C.

The acceptor which exhibits the best efficiency in the active layer blended with PCE-12 was PMI-mPh-PMI, followed by PMI-oPh-PMI, PMI-pPh-PMI and $Ph(PMI)_3$. Due to the limited solubility, multiple solar cell devices comprised crystallites in their active layer. Upon filtration of the donor acceptor blend, smooth and well distributed films were obtained using CB or DCB as solvents. The application of the active layer blend dissolved in $CHCl_3$ was rather difficult, resulting in poorly distributed layers with a high active layer thickness.

The solar cell parameters of all acceptors are promising and may be improved upon further optimization of the process steps including the annealing temperature and used solvents. In addition, the solar cell devices could be assembled in a normal device structure instead of the inverted with varying electrodes and interfacial layers. Besides, the suitable ratio of the donor-acceptor blend needs to be determined and the influence of additives could be investigated. To learn more about the morphology of the materials, electron microscopy like atomic force microscopy or scanning electron microscopy need to be carried out. Furthermore, the films could be investigated using grazing-incident x-ray scattering methods.

According to the obtained results of this study, phenylene-linked perylene monoimides and their derivatives seem to be a promising material class for the use in photovoltaic devices.

7. References

(1) Masson, G.; Izumi, K. Trends 2017 in Photovoltaic Applications. http://www.iea-pvps.org/fileadmin/dam/intranet/task1/IEA_PVPS_Trends_2018_in_Photovoltaic_Applications.pdf (accessed Oct 24, 2019).

(2) Erneuerbare Energien in Österreich. https://de.statista.com/statistik/studie/id/45553/dokument/erneuerbare-energien-in-oesterreich/ (accessed Oct 24, 2019).

(3) Yamamoto, K.; Yoshikawa, K.; Uzu, H.; Adachi, D. High-Efficiency Heterojunction Crystalline Si Solar Cells. *Jpn. J. Appl. Phys.* **2018**, *57* (8). https://doi.org/10.7567/JJAP.57.08RB20.

(4) Photovoltaics Report. https://www.ise.fraunhofer.de/content/dam/ise/de/documents/publications/studies/Photovoltaics-Report.pdf (accessed Oct 24, 2019).

(5) Fechner, H.; Rosner, M.; Mayr, C.; Rennhofer, M.; Schneider, A.; PeharzGerhard. Photovoltaik, Technologie-Roadmap Teil 2. https://nachhaltigwirtschaften.at/resources/iea_pdf/schriftenreihe_2018-27_pv-roadmap.pdf (accessed Oct 24, 2019).

(6) Green, M. A.; Hishikawa, Y.; Dunlop, E. D.; Levi, D. H.; Hohl-Ebinger, J.; Yoshita, M.; Ho-Baillie, A. W. Y. Solar Cell Efficiency Tables (Version 53). *Prog. Photovolt. Res. Appl.* **2019**, *27*, 3–12. https://doi.org/10.1002/pip.3102.

(7) First Solar Achieves Yet Another Cell Conversion Efficiency World Record. https://investor.firstsolar.com/news/press-release-details/2016/First-Solar-Achieves-Yet-Another-Cell-Conversion-Efficiency-World-Record/default.aspx (accessed Nov 7, 2019).

(8) Solar Frontier Achieves World Record Thin-Film Solar Cell Efficiency of 23.35%. http://www.solar-frontier.com/eng/news/2019/0117_press.html (accessed Nov 7, 2019).

(9) Shah, A. V.; Platz, R.; Keppner, H. Thin-Film Silicon Solar Cells: A Review and Selected Trends. *Sol. Energy Mater. Sol. Cells* **1995**, *38* (1–4), 501–520. https://doi.org/10.1016/0927-0248(94)00241-X.

(10) O'Regan, B.; Grätzel, M. A Low-Cost, High-Efficiency Solar Cell Based on Dye-Sensitized Colloidal TiO2 Films. *Nat. Publ. Gr.* **1991**, *353*, 737–740. https://doi.org/10.1016/0146-5724(84)90144-4.

(11) Grätzel, M. Dye-Sensitized Solar Cells. **2003**, *4*, 145–153. https://doi.org/10.1016/S1389-5567(03)00026-1.

(12) Fleischer, M. *Recent Estimates of the Abundances of the Elements in the Earth's Crust*; 1963.

(13) Fthenakis, V.; Kim, H.; Frischknecht, R. *Life Cycle Inventories and Life Cycle Assessment of Photovoltaic Systems*; 2011; Vol. 12. https://doi.org/10.1111/j.1365-2117.2010.00499.x.

(14) Dickschicht oder Dünnschicht. https://photovoltaiksolarstrom.com/aufbau-photovoltaik/photovoltaikmodule/vergleich/#preise (accessed Nov 8, 2019).

(15) Andersson, B. A. Materials Availability for Large-Scale Thin-Film Photovoltaics. *Prog. Photovolt. Res. Appl.* **2000**, *8*, 61–76.

(16) Burschka, J.; Pellet, N.; Moon, S. J.; Humphry-Baker, R.; Gao, P.; Nazeeruddin, M. K.; Grätzel, M. Sequential Deposition as a Route to High-Performance Perovskite-Sensitized Solar Cells. *Nature* **2013**, *499* (7458), 316–319. https://doi.org/10.1038/nature12340.

(17) NREL. Best Research-Cell Efficiencies. *National Renewable Enery Laboratory*.

(18) Wang, R.; Mujahid, M.; Duan, Y.; Wang, Z. K.; Xue, J.; Yang, Y. A Review of Perovskites Solar Cell Stability. *Adv. Funct. Mater.* **2019**, *1808843*, 1–25. https://doi.org/10.1002/adfm.201808843.

(19) Yan, J.; Saunders, B. R. Third-Generation Solar Cells: A Review and Comparison of Polymer:Fullerene, Hybrid Polymer and Perovskite Solar Cells. *RSC Adv.* **2014**, *4* (82), 43286–43314. https://doi.org/10.1039/c4ra07064j.

(20) Ju, M. G.; Dai, J.; Ma, L.; Zeng, X. C. Lead-Free Mixed Tin and Germanium Perovskites for Photovoltaic Application. *J. Am. Chem. Soc.* **2017**, *139* (23), 8038–8043. https://doi.org/10.1021/jacs.7b04219.

(21) Nagane, S.; Ghosh, D.; Hoye, R. L. Z.; Zhao, B.; Ahmad, S.; Walker, A. B.; Saiful Islam, M.; Ogale, S.; Sadhanala, A. Lead-Free Perovskite Semiconductors Based on Germanium-Tin Solid Solutions: Structural and Optoelectronic Properties. *J. Phys. Chem. C* **2018**, *122* (11), 5940–5947. https://doi.org/10.1021/acs.jpcc.8b00480.

(22) Kopacic, I.; Friesenbichler, B.; Hoefler, S. F.; Kunert, B.; Plank, H.; Rath, T.; Trimmel, G. Enhanced Performance of Germanium Halide Perovskite Solar Cells through Compositional Engineering. *ACS Appl. Energy Mater.* **2018**, *1* (2), 343–347. https://doi.org/10.1021/acsaem.8b00007.

(23) Yeh, N.; Yeh, P. Organic Solar Cells: Their Developments and Potentials. *Renew. Sustain. Energy Rev.* **2013**, *21*, 421–431. https://doi.org/10.1016/j.rser.2012.12.046.

(24) Shaheen, S. E.; Brabec, C. J.; Sariciftci, N. S.; Padinger, F.; Fromherz, T.; Hummelen, J. C. 2.5% Efficient Organic Plastic Solar Cells. *Appl. Phys. Lett.* **2001**, *78* (6), 841–843. https://doi.org/10.1063/1.1345834.

(25) Cui, Y.; Yao, H.; Zhang, J.; Zhang, T.; Wang, Y.; Hong, L.; Xian, K.; Xu, B.; Zhang, S.; Peng, J.; et al. Over 16% Efficiency Organic Photovoltaic Cells Enabled by a Chlorinated Acceptor with Increased Open-Circuit Voltages. *Nat. Commun.* **2019**, *10* (1), 1–8. https://doi.org/10.1038/s41467-019-10351-5.

(26) Duan, L.; Elumalai, N. K.; Zhang, Y.; Uddin, A. Progress in Non-Fullerene Acceptor Based Organic Solar Cells. *Sol. Energy Mater. Sol. Cells* **2019**, *193* (April 2018), 22–65. https://doi.org/10.1016/j.solmat.2018.12.033.

(27) Nagao, Y. Synthesis and Properties of Perylene Pigments. *Prog. Org. Coatings* **1997**, *31* (1–2), 43–49. https://doi.org/10.1016/S0300-9440(97)00017-9.

(28) Capelle, K. A Bird's-Eye View of Density-Functional Theory. *Brazilian J. Phys.* **2006**, *36* (4 A), 1318–1341.

(29) Yehuda B. Band; Avishai, Y. *Quantum Mechanics with Applications to Nanotechnology and Information Science*; Yehuda B. Band, Y. A., Ed.; Academic Press: Cambridge (Massachusetts), 2013. https://doi.org/10.1016/B978-0-444-53786-7.00015-0.

(30) Born, M.; Oppenheimer, R. Zur Quantentheorie Der Molekeln. *Ann. Phys.* **1927**, *84* (20), 457–484. https://doi.org/10.1038/168970b0.

(31) Bartolotti, L. J.; Flurchick, K. An Introduction to Density Functional Theory. *Rev. Comput. Chem.* **2007**, *7*, 187–216. https://doi.org/10.1002/9780470125847.ch4.

(32) Koch, W.; Holthausen, M. C. *A Chemist's Guide to Density Functional Theory*; 2001; Vol. 3. https://doi.org/10.1002/3527600043.

(33) Hohenberg, P.; Kohn, W. Inhomogeneous Electron Gas. *Phys. Rev. B* **1964**, *136*, 864–871. https://doi.org/10.1103/PhysRev.136.B864.

(34) Brückner, R. *Reaktionsmechanismen*, 3rd ed.; Springer Spektrum: Heidelberg, 2015.

(35) Suzuki, A. Organoborane Coupling Reactions (Suzuki Coupling). *Synlett* **2004**, *80* (8), 359–371. https://doi.org/10.2183/pjab.80.359.

(36) Suzuki, A. Synthesis of Functionalized Organotin Compounds via Palladium-Catalyzed Cross-Coupling Reaction of Aryl or 1-Alkenyl Halides with 9-(w-Stannylalkyl)-9-Borybicyclo[3.1.1]Nonanes. *Synlett* **1991**, *10*, 687–688.

(37) Chemler, S. R.; Trauner, D.; Danishefsky, S. J. The B-Alkyl Suzuki-Miyaura Cross-Coupling Reaction: Development, Mechanistic Study, and Applications in Natural Product Synthesis. *Angew. Chemie - Int. Ed.* **2001**, *40* (24), 4544–4568. https://doi.org/10.1002/1521-3773(20011217)40:24<4544::AID-ANIE4544>3.0.CO;2-N.

(38) Paul, S.; Islam, M. M.; Islam, S. M. Suzuki-Miyaura Reaction by Heterogeneously Supported Pd in Water: Recent Studies. *RSC Adv.* **2015**, *5* (53), 42193–42221. https://doi.org/10.1039/c4ra17308b.

(39) M. R. Netherton, C. Dai, K. Neuschütz, G. C. F. Room-Temperature Alkyl-Alkyl Suzuki Cross-Coupling of Alkyl Bromides That Possess â Hydrogens. *J. Am. Chem. Soc.* **123AD**, 10099–10100. https://doi.org/10.1017/S0003055400077534.

(40) Lennox, A. J. J.; Lloyd-Jones, G. C. Selection of Boron Reagents for Suzuki-Miyaura Coupling. *Chem. Soc. Rev.* **2014**, *43* (1), 412–443. https://doi.org/10.1039/c3cs60197h.

(41) Miyaura, N.; Suzuki, A. Palladium-Catalyzed Cross-Coupling Reactions of Organoboron Compounds. *Chem. Rev.* **1995**, *95* (7), 2457–2483. https://doi.org/10.1021/cr00039a007.

(42) Littke, A. F.; Dai, C.; Fu, G. C. Versatile Catalysts for the Suzuki Cross-Coupling of Arylboronic Acids with Aryl and Vinyl Halides and Triflates under Mild Conditions. *J. Am. Chem. Soc.* **2000**, *122* (17), 4020–4028. https://doi.org/10.1021/ja0002058.

(43) Dong, C. G.; Hu, Q. S. Preferential Oxidative Addition in Palladium(0)-Catalyzed Suzuki Cross-Coupling Reactions of Dihaloarenes with Arylboronic Acids. *J. Am. Chem. Soc.* **2005**, *127* (28), 10006–10007. https://doi.org/10.1021/ja052547p.

(44) Zapf, A.; Ehrentraut, A.; Beller, M. A New Highly Efficient Catalyst System for the Coupling of Nonactivated and Deactivated Aryl Chlorides with Arylboronic Acids. *Angew. Chemie - Int. Ed.* **2000**, *39* (22), 4153–4155. https://doi.org/10.1002/1521-3773(20001117)39:22<4153::AID-ANIE4153>3.0.CO;2-T.

(45) Bedford, R. B.; Welch, S. L. Erratum: Palladacyclic Phosphinite Complexes as Extremely High Activity Catalysts in the Suzuki Reaction. *Chem. Commun.* **2001**, *2* (15), 1418. https://doi.org/10.1039/b008470k.

(46) Deibel, C. *Photocurrent Generation in Organic Solar Cells*; Elsevier Inc., 2011; Vol. 85. https://doi.org/10.1016/B978-0-12-391060-8.00009-5.

(47) Benanti, T. L.; Venkataraman, D. Organic Solar Cells: An Overview Focusing on Active Layer Morphology. *Photosynth. Res.* **2006**, *87* (1), 73–81. https://doi.org/10.1007/s11120-005-6397-9.

(48) Liao, K. S.; Yambem, S. D.; Haldar, A.; Alley, N. J.; Curran, S. A. Designs and Architectures for the next Generation of Organic Solar Cells. *Energies* **2010**, *3* (6), 1212–1250. https://doi.org/10.3390/en3061212.

(49) Steim, R.; Kogler, F. R.; Brabec, C. J. Interface Materials for Organic Solar Cells. *J. Mater. Chem.* **2010**, *20* (13), 2499–2512. https://doi.org/10.1039/b921624c.

(50) Meiss, J.; Uhrich, C. L.; Fehse, K.; Pfuetzner, S.; Riede, M. K.; Leo, K. Transparent Electrode Materials for Solar Cells. *Photonics Sol. Energy Syst. II* **2008**, *7002* (0), 700210. https://doi.org/10.1117/12.781275.

(51) Tore, N.; Parlak, E. A.; Usluer, O.; Egbe, D. A. M.; San, S. E.; Aydogan, P. Effect of Blend Ratio on Poly(p-Phenylene-Ethynylene)-Alt-Poly(p-Phenylene- Vinylene) Polymer Solar Cell. *Sol. Energy Mater. Sol. Cells* **2012**, *104*, 39–44. https://doi.org/10.1016/j.solmat.2012.04.040.

(52) Yumusak, C.; M. Egbe, D. A. Organic Bulk Heterojunction Solar Cells Based on Poly(p-Phenylene-Vinylene) Derivatives. *Sol. Cells - New Asp. Solut.* **2011**, No. July. https://doi.org/10.5772/22306.

(53) Howard, I. A.; Mauer, R.; Meister, M.; Laquai, F. Effect of Morphology on Ultrafast Free Carrier Generation in Polythiophene:Fullerene Organic Solar Cells. *J. Am. Chem. Soc.* **2010**, *132* (42), 14866–14876. https://doi.org/10.1021/ja105260d.

(54) Gadisa, A.; Svensson, M.; Andersson, M. R.; Inganas, O. Correlation between Oxidation Potential and Open-Circuit Voltage of Composite Solar Cells Based on Blends of Polythiophenes/Fullerene Derivative. *Appl. Phys. Lett.* **2004**, *84* (9), 1609–1611. https://doi.org/10.1063/1.1650878.

(55) Jamieson, F. C.; Agostinelli, T.; Azimi, H.; Nelson, J.; Durrant, J. R. Field-Independent Charge Photogeneration in PCPDTBT/PC70BM Solar Cells. *J. Phys. Chem. Lett.* **2010**, *1* (23), 3306–3310. https://doi.org/10.1021/jz1013517.

(56) Alem, S.; Chu, T. Y.; Tse, S. C.; Wakim, S.; Lu, J.; Movileanu, R.; Tao, Y.; Bélanger, F.; Désilets, D.; Beaupré, S.; et al. Effect of Mixed Solvents on PCDTBT:PC70BM Based Solar Cells. *Org. Electron. physics, Mater. Appl.* **2011**, *12* (11), 1788–1793. https://doi.org/10.1016/j.orgel.2011.07.011.

(57) Wang, G.; Jiu, T.; Tang, G.; Li, J.; Li, P.; Song, X.; Lu, F.; Fang, J. Interface Modification of ZnO-Based Inverted PTB7:PC71BM Organic Solar Cells by Cesium Stearate and Simultaneous Enhancement of Device Parameters. *ACS Sustain. Chem. Eng.* **2014**, *2* (5), 1331–1337. https://doi.org/10.1021/sc5001447.

(58) Liao, S. H.; Jhuo, H. J.; Yeh, P. N.; Cheng, Y. S.; Li, Y. L.; Lee, Y. H.; Sharma, S.; Chen, S. A. Single Junction Inverted Polymer Solar Cell Reaching Power Conversion Efficiency 10.31% by Employing Dual-Doped Zinc Oxide Nano-Film as Cathode Interlayer. *Sci. Rep.* **2014**, *4*, 4–10. https://doi.org/10.1038/srep06813.

(59) Chang, H.; Chen, Z.; Yang, X.; Yin, Q.; Zhang, J.; Ying, L.; Jiang, X. F.; Xu, B.; Huang, F.; Cao, Y. Novel Perylene Diimide Based Polymeric Electron-Acceptors Containing Ethynyl as the π-Bridge for All-Polymer Solar Cells. *Org. Electron. physics, Mater. Appl.* **2017**, *45*, 227–233. https://doi.org/10.1016/j.orgel.2017.03.022.

(60) Upama, M. B.; Elumalai, N. K.; Mahmud, M. A.; Xu, C.; Wang, D.; Wright, M.; Uddin, A. Enhanced Electron Transport Enables over 12% Efficiency by Interface Engineering of Non-Fullerene Organic Solar Cells. *Sol. Energy Mater. Sol. Cells* **2018**, *187* (April), 273–282. https://doi.org/10.1016/j.solmat.2018.08.010.

(61) Hou, W.; Xiao, Y.; Han, G.; Lin, J. Y. The Applications of Polymers in Solar Cells: A Review. *Polymers (Basel).* **2019**, *11* (1), 1–46. https://doi.org/10.3390/polym11010143.

(62) Patil, Y.; Misra, R. Small Molecule Based Non-Fullerene Acceptors: A Comparative Study. *Chem. Rec.* **2018**, *18* (9), 1350–1364. https://doi.org/10.1002/tcr.201800037.

(63) Yan, C.; Barlow, S.; Jen, A. K.-Y.; Marder, S. Non-Fullerene Acceptors for Organic Solar Cells High Energy Density Nanocomposites Based on Surface-Modified BaTiO3 and a Ferroelectric Polymer View Project Organic Solar Cells View Project. *Nat. Publ. Gr.* **2018**, *3*, 1–19. https://doi.org/10.1038/natrevmats.2018.3.

(64) Fraga Domínguez, I.; Distler, A.; Lüer, L. Stability of Organic Solar Cells: The Influence of Nanostructured Carbon Materials. *Adv. Energy Mater.* **2017**, *7* (10). https://doi.org/10.1002/aenm.201601320.

(65) Hu, Y.; Chen, S.; Zhang, L.; Zhang, Y.; Yuan, Z.; Zhao, X.; Chen, Y. Facile Approach to Perylenemonoimide with Short Side Chains for Nonfullerene Solar Cells. *J. Org. Chem.* **2017**, *82* (11), 5926–5931. https://doi.org/10.1021/acs.joc.7b00272.

(66) Huang, C.; Barlow, S.; Marder, S. R. Perylene-3,4,9,10-Tetracarboxylic Acid Diimides: Synthesis, Physical Properties, and Use in Organic Electronics. *J. Org. Chem.* **2011**, *76* (8), 2386–2407. https://doi.org/10.1021/jo2001963.

(67) Zhang, Y.; Guo, X.; Guo, B.; Su, W.; Zhang, M.; Li, Y. Nonfullerene Polymer Solar Cells Based on a Perylene Monoimide Acceptor with a High Open-Circuit Voltage of 1.3 V. *Adv. Funct. Mater.* **2017**, *27* (10), 1–8. https://doi.org/10.1002/adfm.201603892.

(68) Zhang, Y.; Xiao, Y.; Xie, Y.; Zhu, L.; Shi, D.; Cheng, C. Fluorene-Centered Perylene Monoimides as Potential Non-Fullerene Acceptor in Organic Solar Cells. *Org. Electron. physics, Mater. Appl.* **2015**, *21*, 184–191. https://doi.org/10.1016/j.orgel.2015.03.017.

(69) Wang, Y.; Zhang, Y.; Qiu, N.; Feng, H.; Gao, H.; Kan, B.; Ma, Y.; Li, C.; Wan, X.; Chen, Y. A Halogenation Strategy for over 12% Efficiency Nonfullerene Organic Solar Cells. *Adv. Energy Mater.* **2018**, *8* (15), 1–7. https://doi.org/10.1002/aenm.201702870.

(70) Wan, S.; Chang, C.; Wang, J.; Yuan, G.; Wu, Q.; Zhang, M.; Li, Y. Effects of the Number of Bromine Substitution on Photovoltaic Efficiency and Energy Loss of Benzo[1,2-b:4,5-b′]Diselenophene-based Narrow-Bandgap Multibrominated Nonfullerene Acceptors. *Solar RRL*. **2018**, *3*. https://doi.org/10.1002/solr.201800250.

(71) Grilli, S.; Lunazzi, L.; Mazzanti, A.; Pinamonti, M. Conformational Studies by Dynamic NMR Spectroscopy. Part 96: Stereomutations of Highly Hindered Naphthylphenyl Atropisomers in Solution and in the Solids. *Tetrahedron* **2004**, *60* (20), 4451–4458. https://doi.org/10.1016/j.tet.2004.01.094.

(72) Yoshida, H.; Okada, K.; Kawashima, S.; Tanino, K.; Ohshita, J. Platinum-Catalysed Diborylation of Arynes: Synthesis and Reaction of 1,2-Diborylarenes. *Chem. Commun.* **2010**, *46* (10), 1763–1765. https://doi.org/10.1039/b919407j.

(73) Fluoreszenzorange. https://www.kremer-pigmente.com/media/pdf/94738.pdf (accessed Nov 4, 2019).

(74) Nolde, F.; Pisula, W.; Müller, S.; Kohl, C.; Müllen, K. Synthesis and Self-Organization of Core-Extended Perylene Tetracarboxdiimides with Branched Alkyl Substituents. *Chem. Mater.* **2006**, *18* (16), 3715–3725. https://doi.org/10.1021/cm060742c.

Appendix

List of Figures

List of Tables

List of Abbreviations

AcOH	Acetic acid
CB	Chlorobenzene
CH	Cyclohexane
DCB	Dichlorobenzene
DCM	Dichloromethane
DCTB	*trans*-2-[3-(4-*tert*-Butylphenyl)-2-methyl-2-propenylidene]malononitrile
DFT	Density Functional Theory
DSC	Differential Scanning Calorimetry
EQE	External Quantum Efficiency
EtOH	Ethanol
MeOH	Methanol
MS	Mass Spectrometry
NMR	Nuclear Magnetic Resonance
PBDB-T/PCE-12	Poly[(2,6-(4,8-bis(5-(2-ethylhexyl)thiophen-2-yl)-benzo[1,2-b:4,5-b']dithiophene))-alt-(5,5-(1',3'-di-2-thienyl-5',7'-*bis*(2-ethylhexyl)benzo[1',2'-c:4',5'-c']dithiophene-4,8-dione)]
PEG	Polyethylene Glycol
PMI	Perylene Monoimide
PMI-Ph(meta)-PMI	8,8'-(1,3-phenylene)bis(2-(2,6-diisopropylphenyl)-1*H*-benzo[10,5]anthra[2,1,9-*def*]isoquinoline-1,3(2*H*)-dione)
PMI-Ph(ortho)-PMI	8,8'-(1,2-phenylene)bis(2-(2,6-diisopropylphenyl)-1*H*-benzo[10,5]anthra[2,1,9-*def*]isoquinoline-1,3(2*H*)-dione)
PMI-Ph(para)-PMI	8,8'-(1,4-phenylene)bis(2-(2,6-diisopropylphenyl)-1*H*-benzo[10,5]anthra[2,1,9-*def*]isoquinoline-1,3(2*H*)-dione)
PMI-Ph(trimer)-PMI	8,8',8''-(benzene-1,3,5-triyl)tris(2-(2,6-diisopropylphenyl)-1*H*-benzo[10,5]-anthra[2,1,9-*def*]isoquinoline-1,3(2*H*)-dione)
RT	Room Temperature
TGA	Thermogravimetric Analysis
THF	Tetrahydrofuran
TLC	Thin Layer Chromatography

Analytical Data

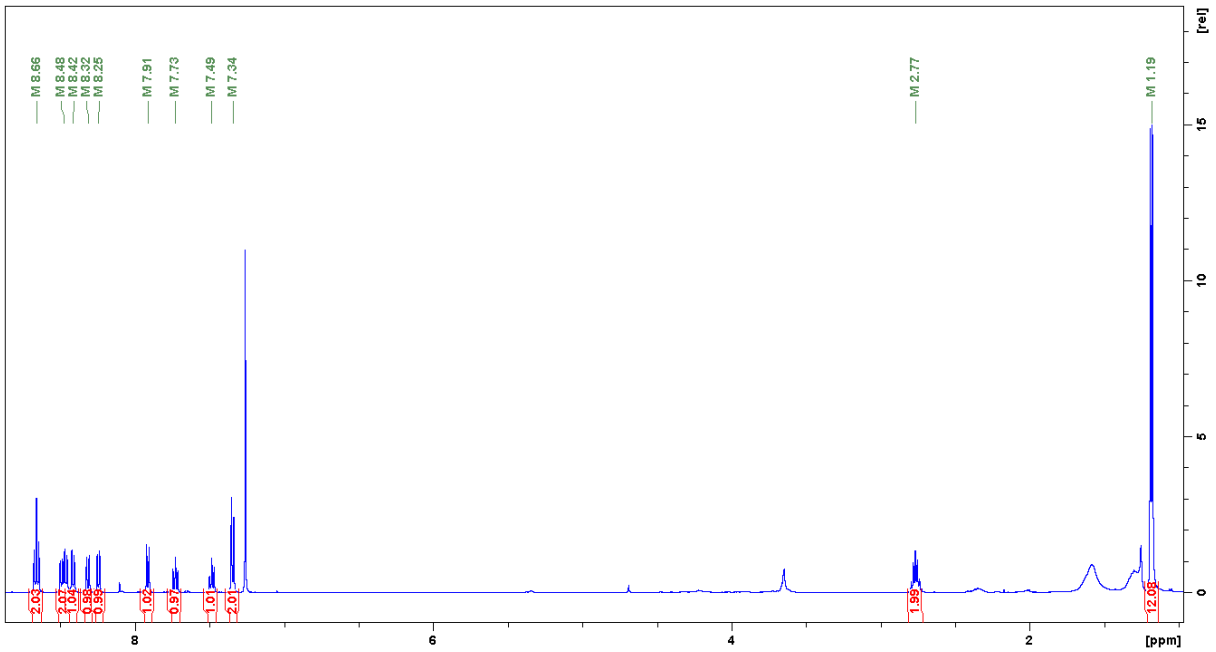

Figure 29: ^{1}H-NMR spectrum of the purified PMI-Br.

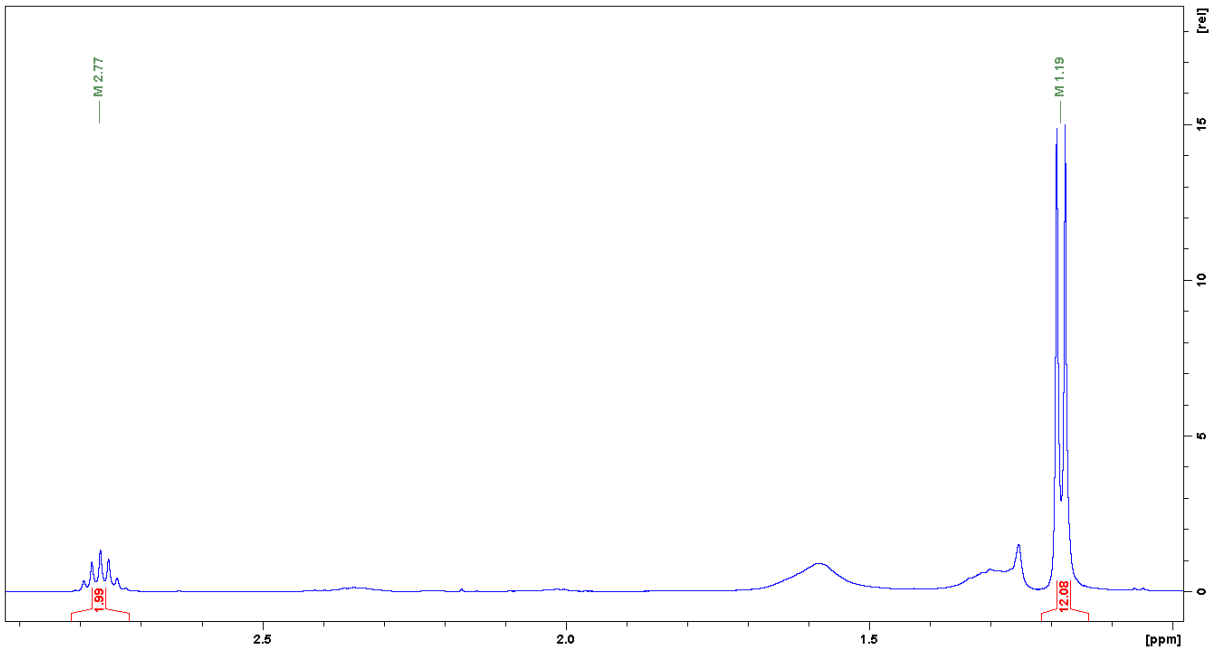

Figure 30: ^{1}H-NMR spectrum of the aliphatic region of the purified PMI-Br.

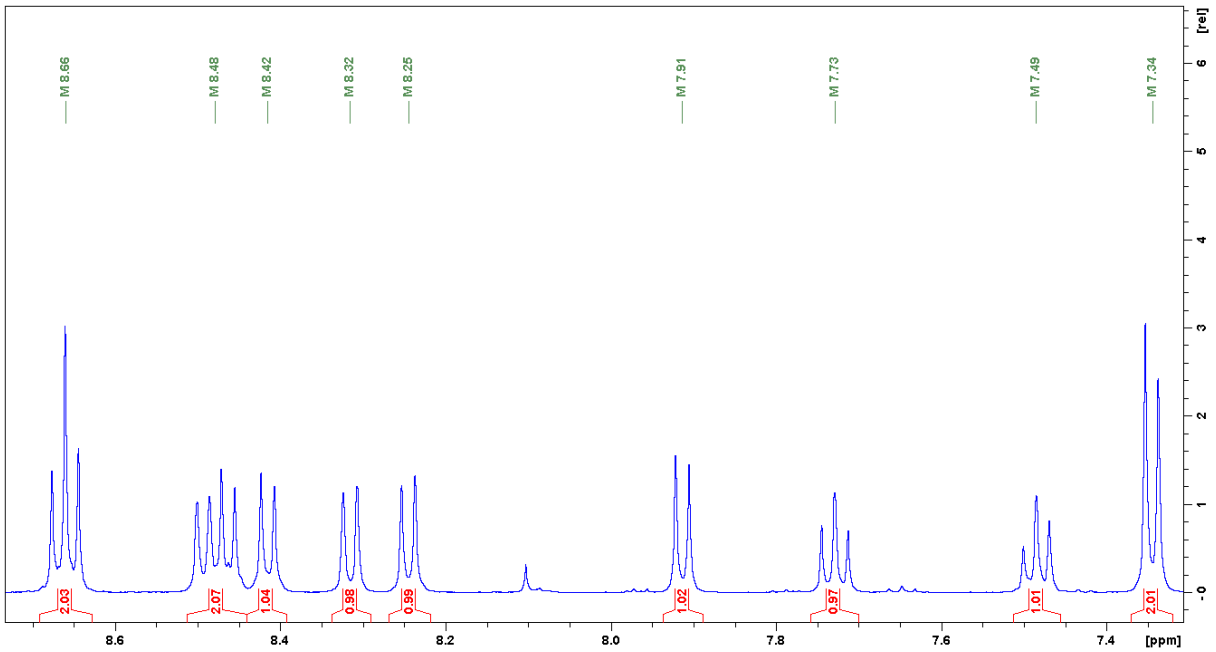

Figure 31: [1]H-NMR spectrum of the aromatic region of the purified PMI-Br.

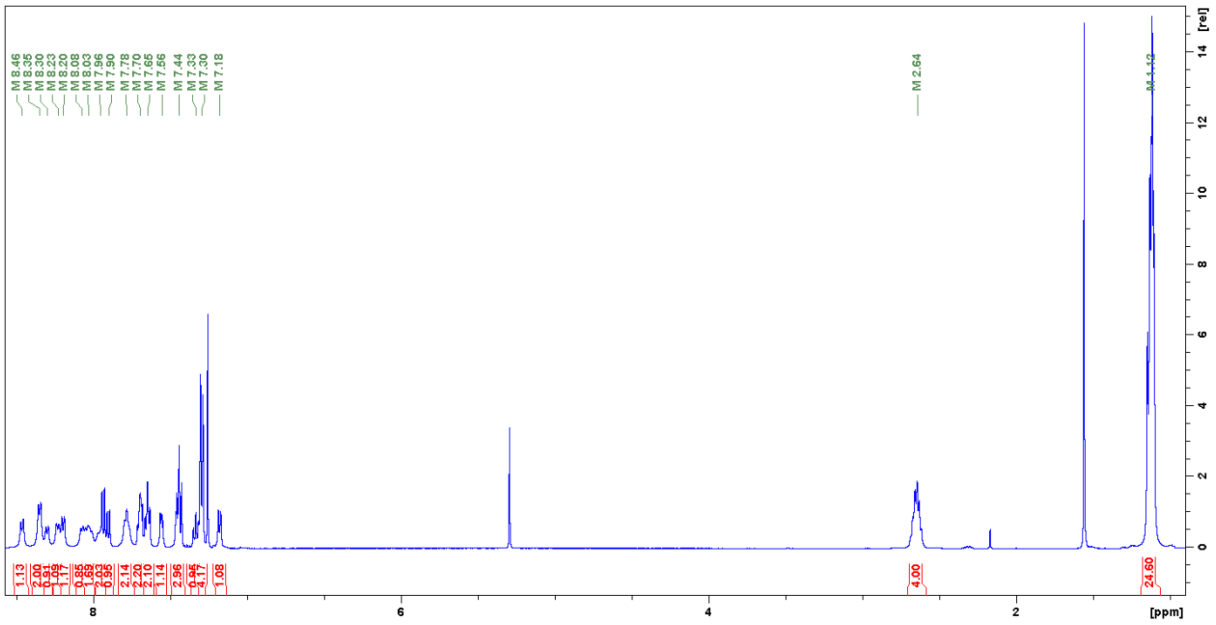

Figure 32: [1]H-NMR spectrum of the purified PMI-oPh-PMI.

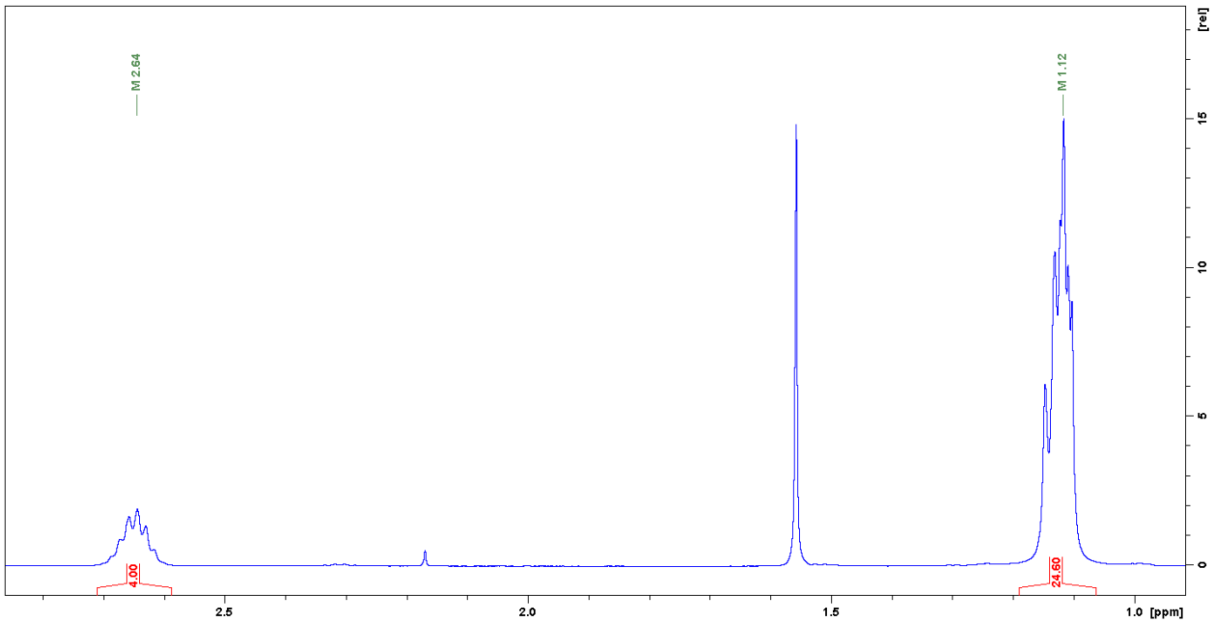

Figure 33: ^{1}H-NMR spectrum of the aliphatic region of the purified PMI-oPh-PMI.

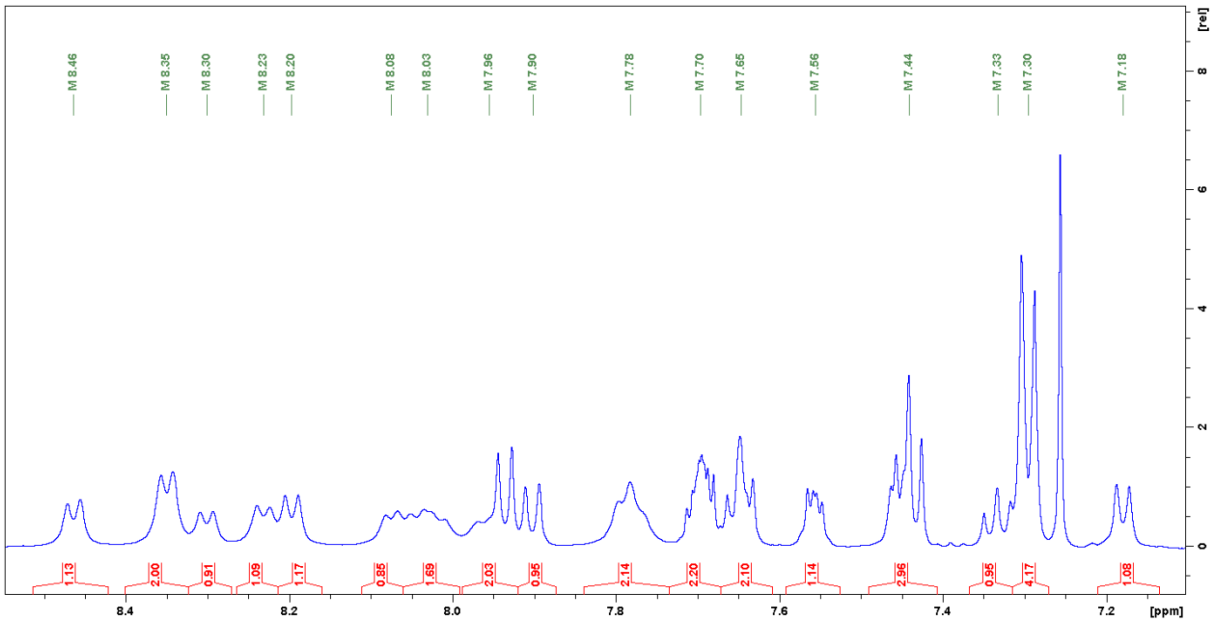

Figure 34: ^{1}H-NMR spectrum of the aromatic region of the purified PMI-oPh-PMI.

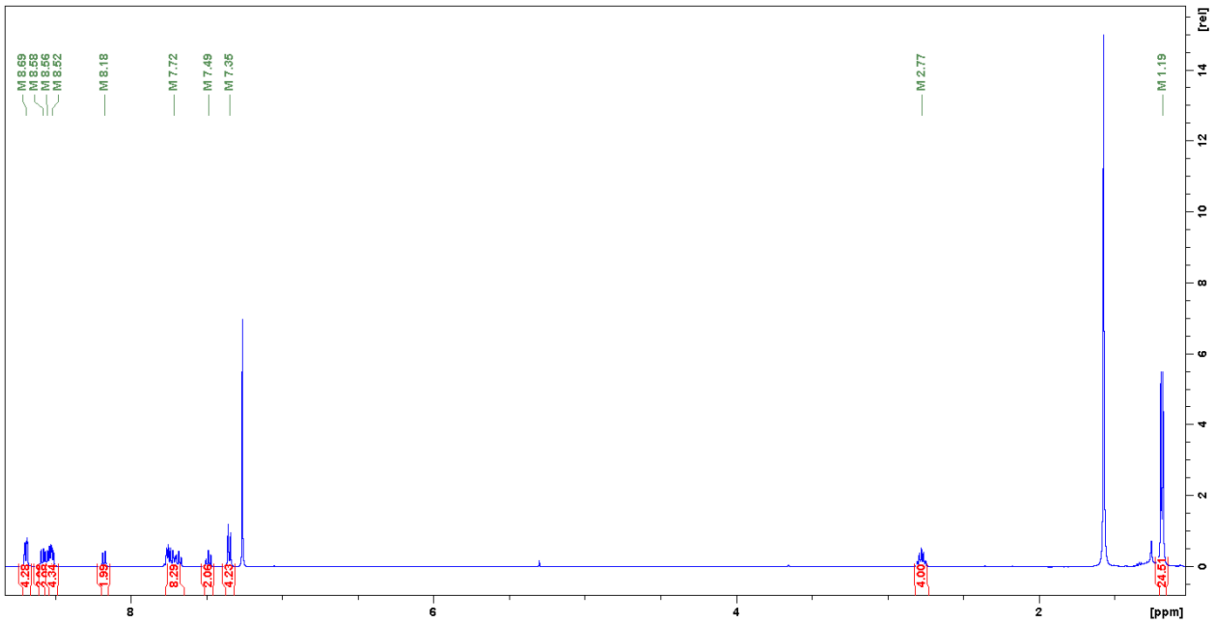

Figure 35: ^{1}H-NMR spectrum of the purified PMI-mPh-PMI.

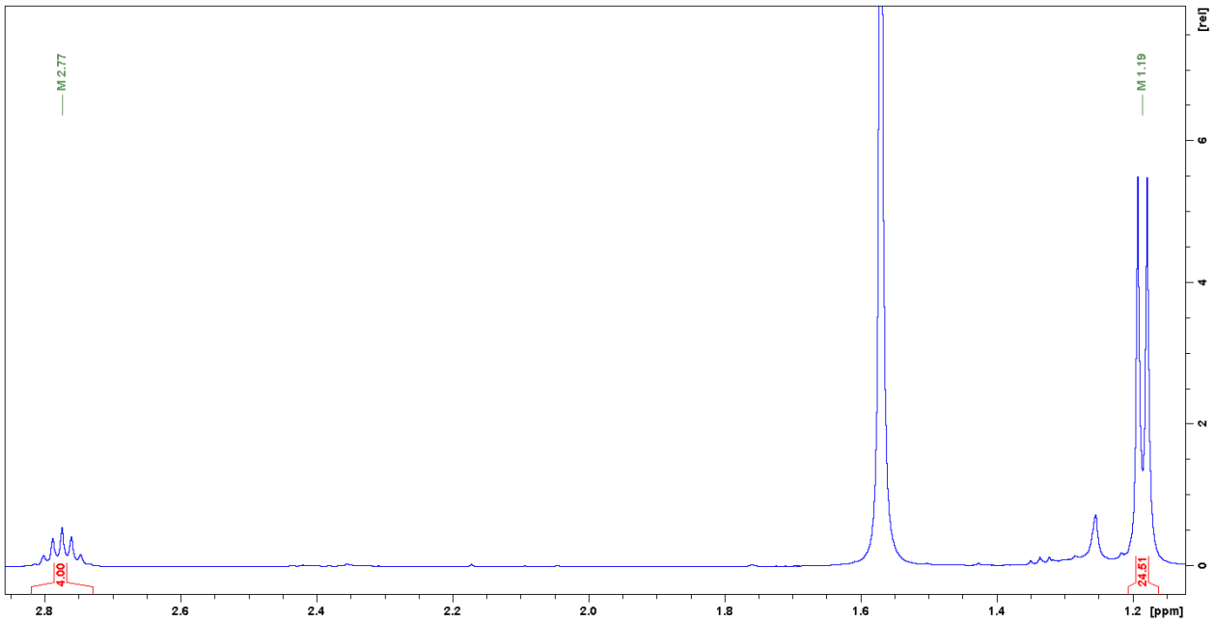

Figure 36: ^{1}H-NMR spectrum of the aliphatic region of the purified PMI-mPh-PMI.

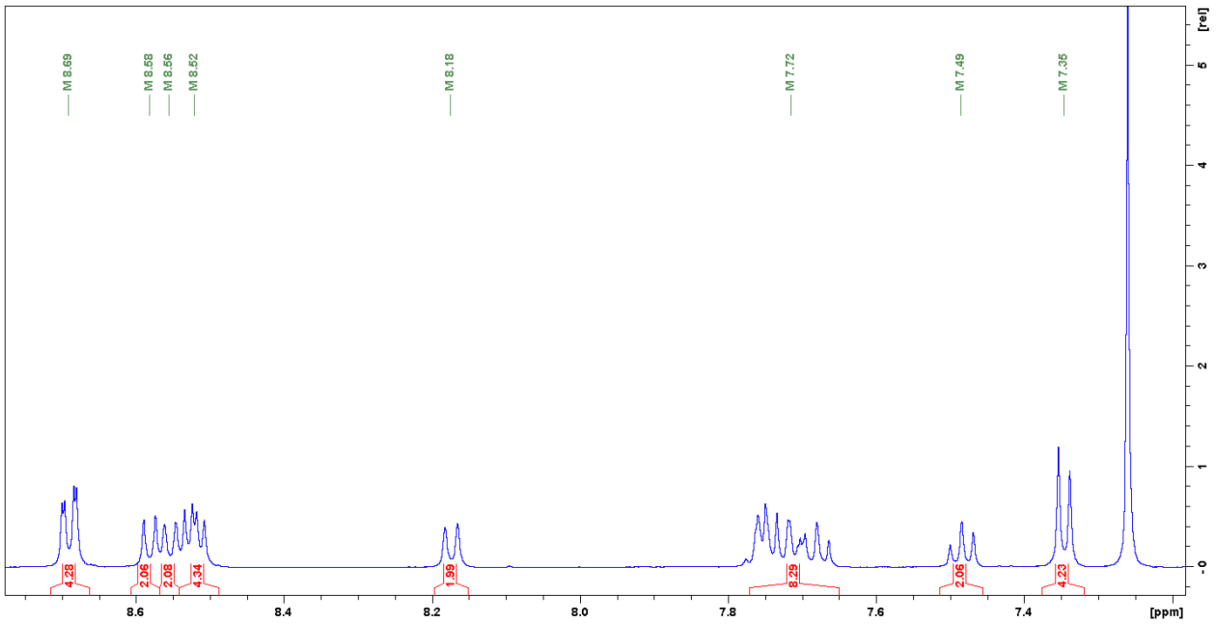

Figure 37: ^{1}H-NMR spectrum of the aromatic region of the purified PMI-mPh-PMI.

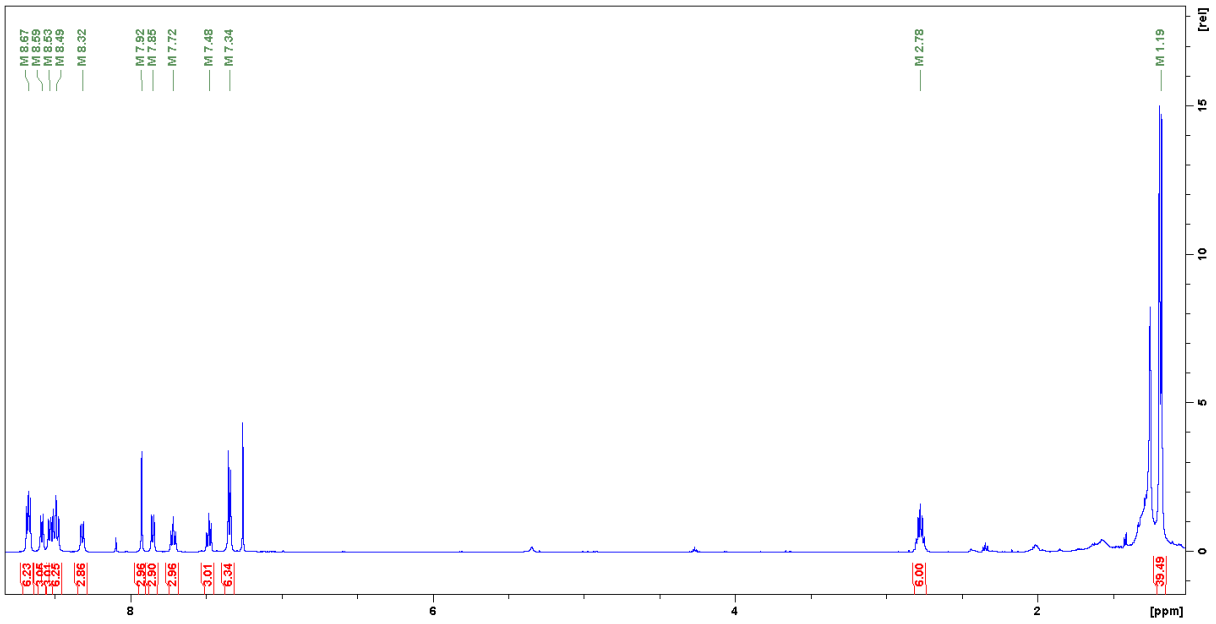

Figure 38: ^{1}H-NMR spectrum of the purified Ph(PMI)$_3$.

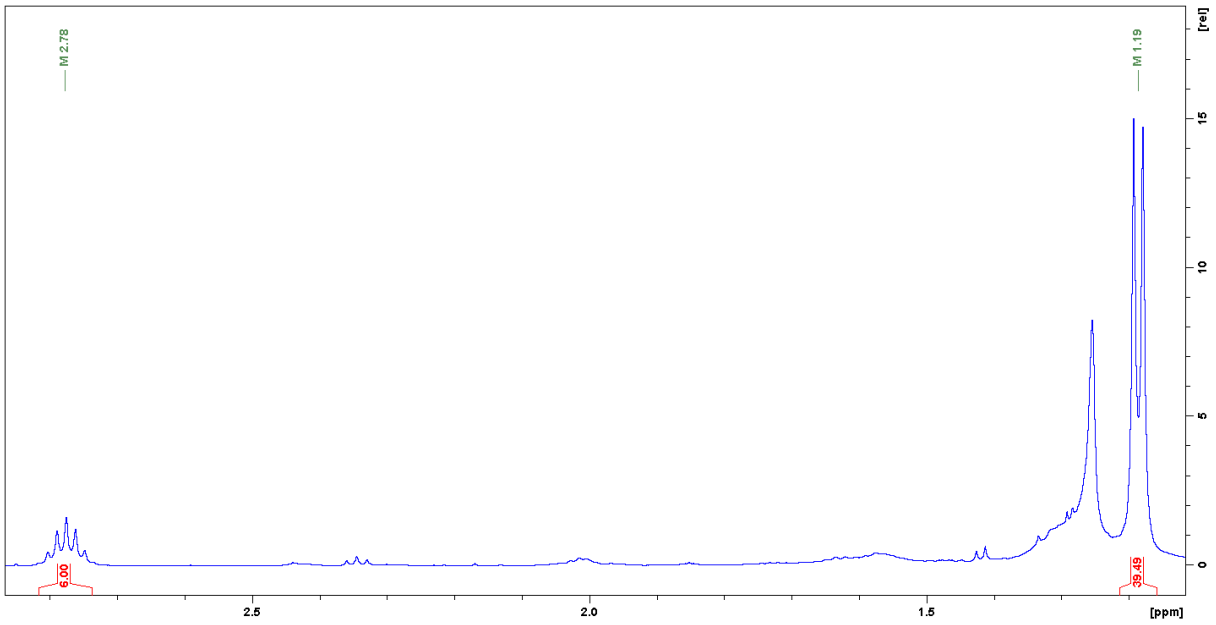

Figure 39: ^{1}H-NMR spectrum of the aliphatic region of the purified Ph(PMI)$_3$.

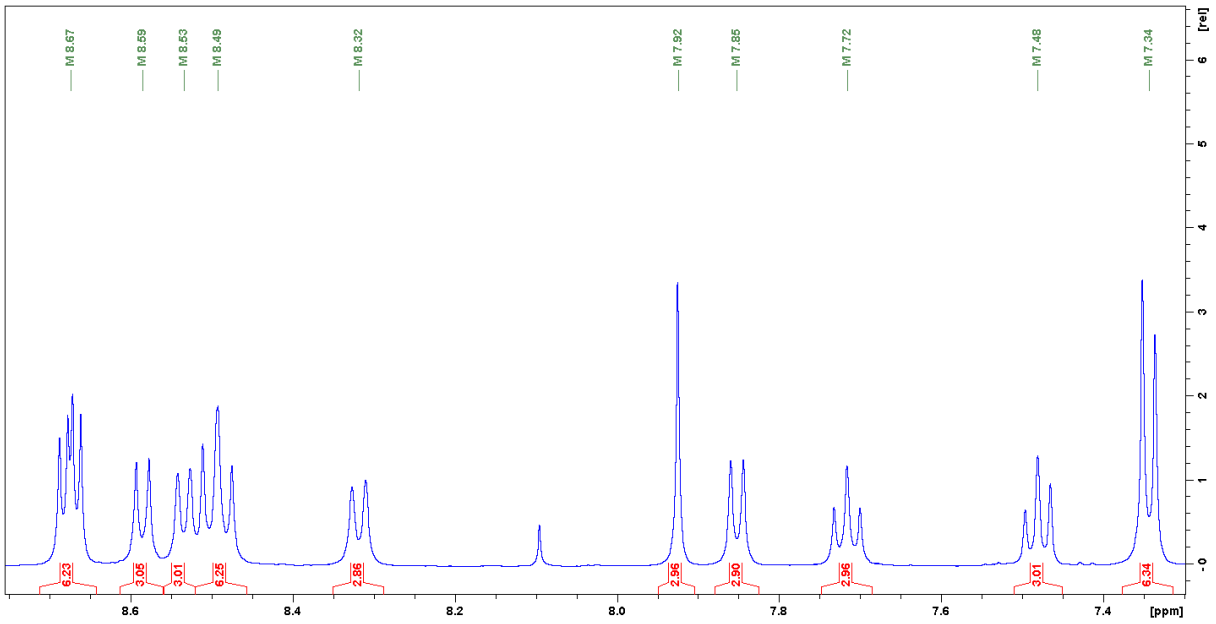

Figure 40: ^{1}H-NMR spectrum of the aromatic region of the purified Ph(PMI)$_3$.

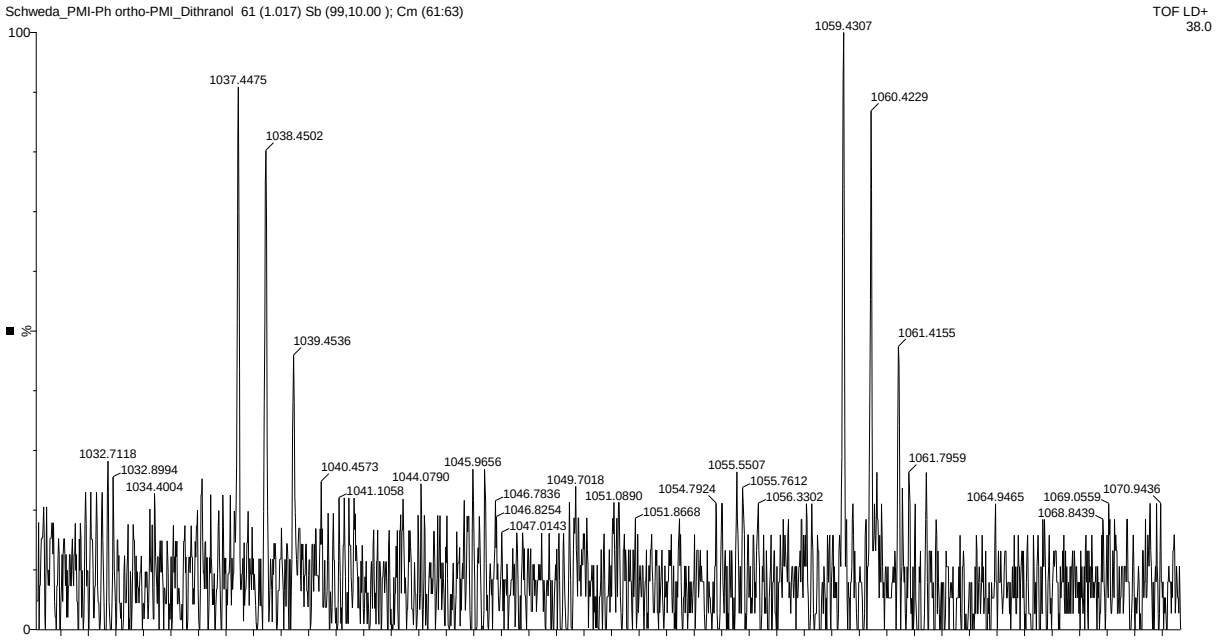

Figure 41: Mass spectrum of PMI-oPh-PMI; *m/z*: 1037.4475.

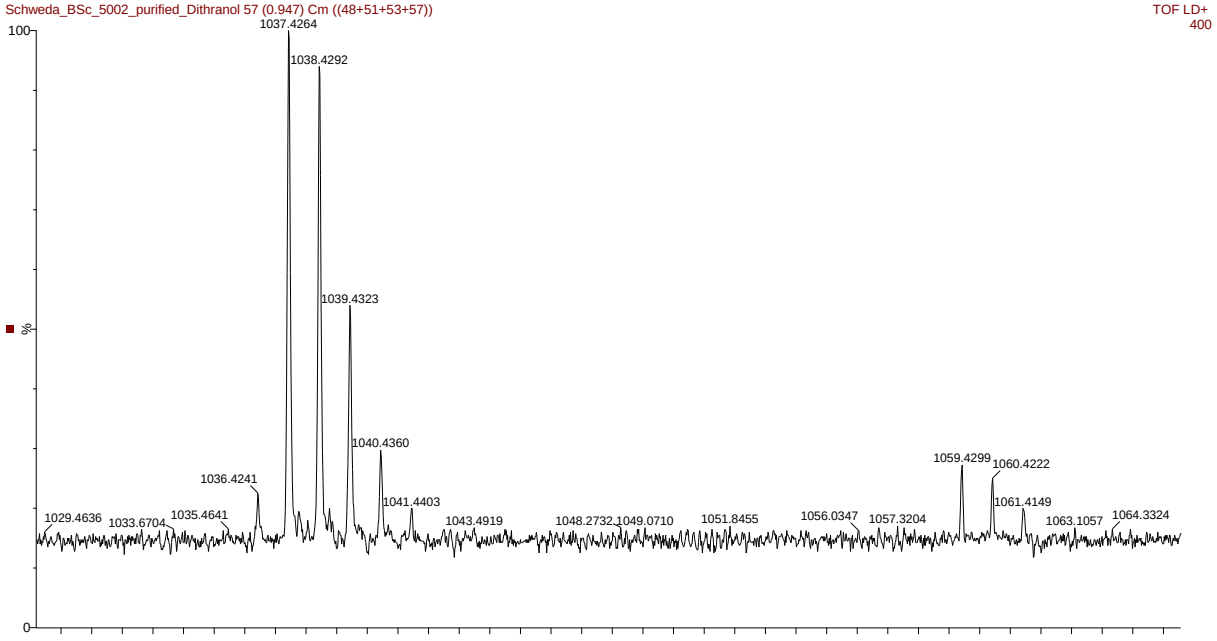

Figure 42: Mass spectrum of PMI-mPh-PMI; *m/z*: 1037.4264.

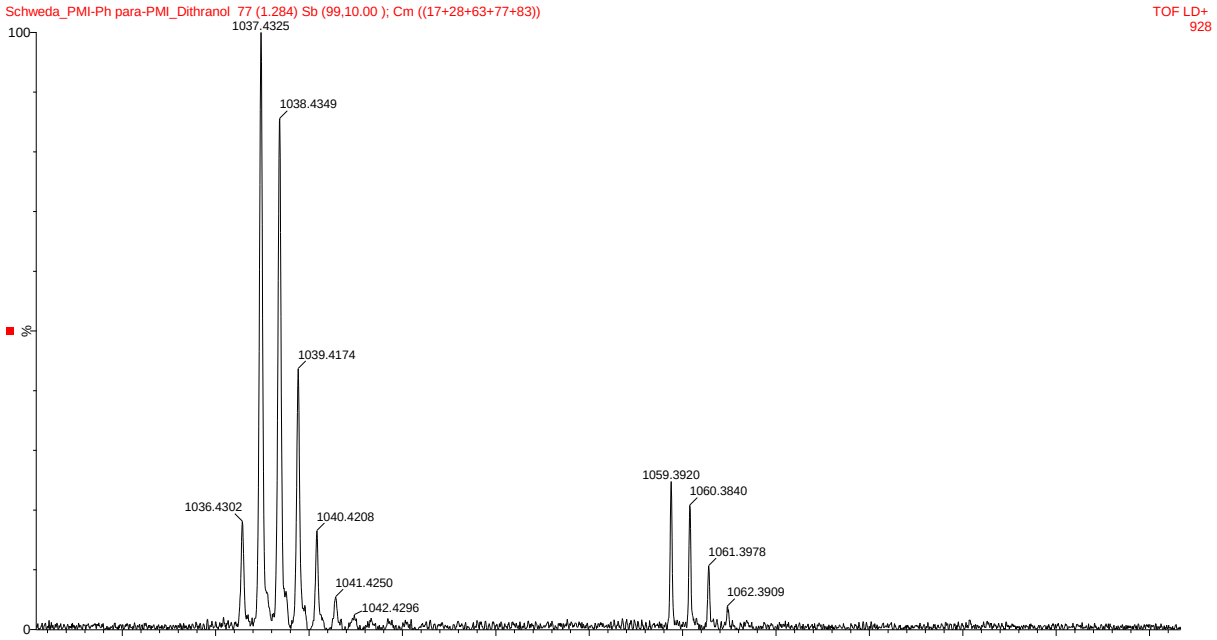

Figure 43: Mass spectrum of PMI-pPh-PMI; *m/z*: 1037.4325.

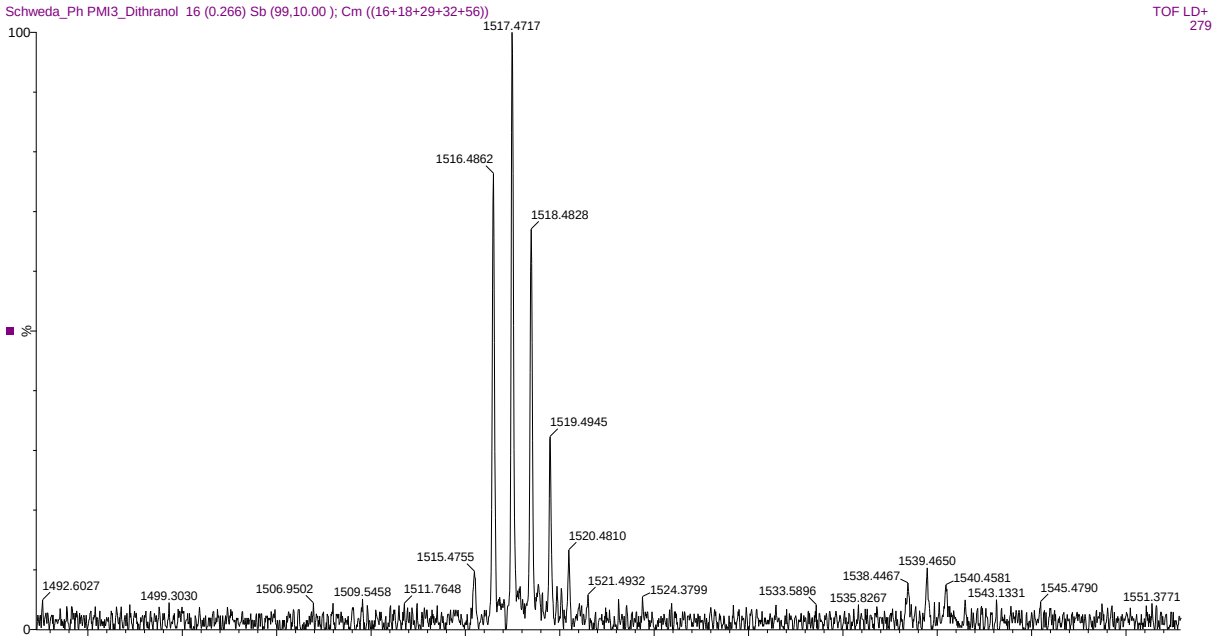

Figure 44: Mass spectrum of $Ph(PMI)_3$; *m/z*: 1516.4862.